Title
Experimental investigation on liquid behaviors in nanopores

Permalink
https://escholarship.org/uc/item/9vx9799d

Author
Lu, Weiyi

Publication Date
2011

Peer reviewed|Thesis/dissertation

UNIVERSITY OF CALIFORNIA, SAN DIEGO

Experimental Investigation on Liquid Behaviors in Nanopores

A dissertation submitted in partial satisfaction of the
requirements for the degree Doctor of Philosophy

in

Structural Engineering

by

Weiyi Lu

Committee in charge:

      Professor Yu Qiao, Chair
      Professor Yuri Bazilevs
      Professor Vlado Lubarda
      Professor Vitali Nesterenko
      Professor Qiang Zhu

2011

The Dissertation of Weiyi Lu is approved, and it is acceptable in quality and form for publication on microfilm and electronically:

_____

_____

_____

_____

_____

Chair

University of California, San Diego

2011

iii

DEDICATION

To my fiancée and my parents

TABLE OF CONTENTS

LIST OF FIGURES

LIST OF TABLES

ACKNOWLEDGEMENT

Han, Aijie; Lu, Weiyi; Punyamurtula, Venkata; Chen, Xi; Surani, Falgun; Kim, Taewan; Qiao, Yu. Effective viscosity of glycerin in a nanoporous silica gel. 104, 124908. 1-4 (2008). The dissertation author was the primary investigator/author of this paper.

Chapter 4, in part, is a reprint of the material as it appears in Smart Materials and Structures. Han, Aijie; Lu, Weiyi; Kim, Taewan; Punyamurtula, Venkata K.; Qiao, Yu. The dependence of infiltration pressure and volume in zeolite Y on potassium chloride concentration. 18, 024005.1-5 (2009). The dissertation author was the primary investigator/author of this paper.

Chapter 5, in full, is a reprint of the material as it appears in Physics Review E. Han, Aijie; Lu, Weiyi; Kim, Taewan; Chen, Xi; Qiao, Yu. Influence of anions on liquid infiltration and defiltration in a zeolite Y. 78, 031408.1-4 (2008). The dissertation author was the primary investigator/author of this paper.

Chapter 6, in full, is a reprint of the material as it appears in Applied Physics Letter. Lu, Weiyi; Han, Aijie; Kim, Taewan; Punyamurtula, Venkata K.; Chen, Xi; Qiao, Yu. Field-responsive ion transport in nanopores. 94, 023106.1-3 (2009). The dissertation author was the primary investigator/author of this paper.

Chapter 7, in full, is a reprint of the material as it appears in Langmuir. Lu, Weiyi; Kim, Taewan; Han, Aijie; Chen, Xi; Qiao, Yu. Electrowetting effect in a nanoporous silica. 25, 9463-9466 (2009). The dissertation author was the primary investigator/author of this paper.

Chapter 8, in full, is a reprint of the material as it appears in Journal of Materials Research. Lu, Weiyi; Punyamurtula, Venkata K.; Han, Aijie; Kim, Taewan; Qiao, Yu. A thermally sensitive

energy-absorbing composite functionalized by nanoporous carbon. 24, 3308-3312 (2009). The

dissertation author was the primary investigator/author of this paper.

VITA

2004   Bachelor of Science, University of Shanghai Jiao Tong University

2007   Master of Science, University of Shanghai Jiao Tong University

2007-2011   Research Assistant, University of California, San Diego

2010-2011   Teaching Assistant, University of California, San Diego

2011   Doctor of Philosophy, University of California, San Diego

PUBLICATIONS

Lu, W; Kim, T; Han, A; Chen, X; Qiao, Y. Effects of electric field on confined electrolyte in a hexagonal mesoporous silica. Journal of Chemical Physics. 2011. 134, 204706.

Lu, W; Punyamurtula, V; Qiao, Y. An energy absorption system based on carbon nanotubes and non-aqueous liquid. International Journal of Materials Research. 102, 587-590.

Lu, W; Kim, T; Punyamurtula, V; Han, A; Qiao, Y. Effects of addition of potassium chloride and ethylene glycol on nanofluidic behaviors. Journal of Materials Science. 2011. 46, 4053-4057.

Lu, W; Chow, B; Kim, T; Han, A; Qiao, Y. Effects of graphite particles on ion transport in a zeolite Y. Applied Physics Letter. 2011. 98, 013102.

Kim, T; Lu, W; Lim, H; Han, A; Qiao, Y. Electrically controlled hydrophobicity in a surface modified nanoporous carbon. Applied Physics Letter. 2011. 98, 053106.

Lu, W; Chen, J; Chakravarthula, S; Qiao, Y. Resistance to cleavage cracking and subsequent shearing of high angle grain boundary. Engineering Fracture Mechanics. 2010. 77, 768-775.

Lu, W; Punyamurtula, V; Han, A; Kim, T; Qiao, Y. A thermally sensitive energy-absorbing composite functionalized by nanoporous carbon. Journal of Materials Research. 2009. 24, 3308-3312.

Liu, L; Chen, X; Lu, W; Han, A; Qiao, Y. Infiltration of electrolytes in molecular-sized

nanopores. Physical Review Letters. 2009. 102, 184501.

Lu, W; Kim, T; Han, A; Chen, X; Qiao, Y. Electrowetting effect in a nanoporous silica. Langmuir. 2009. 25, 9463-9466.

Kim, T; Lu, W; Han, A; Punyamurtula, V; Chen, X; Qiao, Y. Effects of anion concentration on ion-transport pressure in nanopores. Applied Physics Letter. 2009. 94, 013105.

Lu, W; Han, A; Kim, T; Punyamurtula, V; Chen, X; Qiao, Y. Field-responsive ion transport in nanopores. Applied Physics Letter. 2009. 94, 023106.

Lu, W; Han, A; Kim, T; Qiao, Y. Effect of 16-mercaptohexadecanoic acid modification on liquid transport in a nanoporous carbon. Applied Physics Letter. 2009. 94, 223120.

Han, A; Lu, W; Punyamurtula, V; Kim, T; Qiao, Y. Temperature variation in liquid infiltration and defiltration in a MCM41. Journal of Applied Physics. 2009. 105, 024309.

Lu, W; Han, A; Kim, T; Lim, H; Qiao, Y. Effects of surface charging treatment on outer and inner surfaces of a nanoporous carbon. Journal of Materials Research. 2009. 24, 2471-2475.

Han, A; Lu, W; Kim, T; Punyamurtula, V; Qiao, Y. The dependence of infiltration pressure and volume in zeolite Y on potassium chloride concentration. Smart Materials & Structures. 2009. 18, 024005.

Chen, J. Lu, W. Qiao, Y. Resistance of grain boundary array to cleavage cracking in free-standing thin film. Mechanics of Materials. 2009. 41, 131-138.

Han, A; Lu, W; Punyamurtula, V; Chen, X; Surani, F; Kim, T; Qiao, Y. Effective viscosity of glycerin in a nanoporous silica gel. Journal of Applied Physics. 2008.104, 124908.

Han, A; Lu, W; Kim, T; Chen, X; Qiao, Y. Influence of anions on liquid infiltration and defiltration in a zeolite Y. Physical Review E. 2008. 78, 031408.

Han, A; Punyamurtula, V; Lu, W; Qiao, Y. Deformation of a nanoporous silica under compressive loading. Journal of Applied Physics. 2008. 103, 084318.

Chen, J; Lu, W; Qiao, Y. Cleavage cracking across twin boundaries in free-standing silicon thin films. Applied Physics A-Materials Science & Processing. 2008. 91, 663-666.

ABSTRACT OF THE DISSERTATION

Experimental Investigation on Liquid Behaviors in Nanopores

by

Weiyi Lu

Doctor of Philosophy in Structural Engineering

University of California, San Diego, 2011

Professor Yu Qiao, Chair

Nanoporous materials are involved in many industrial processes such as catalysis, filtration, chromatography, etc. Recently, they are applied to absorb or capture the energy associated with blast, collision, and impact attacks. In such applications, the nanoporous materials are immersed in liquids or gels. The inner surfaces of nanopores are usually modified to increase the degree of hydrophobicity. When an external pressure is applied on the system, the liquid phase can be compressed into the nanoporous space. The liquid infiltration behavior in the

nanopores becomes significantly different from that of untreated material.

The effective interfacial tension and viscosity of the confined liquid are investigated. While the simple superposition principle can be employed for the analysis of interfacial tension, in a nanopore the effective liquid viscosity is no longer a material constant. It is highly dependent on the pore size and the loading rate, much smaller than its bulk counterpart. In addition, the influence of electrolyte concentration as well as its dependence on temperature are analyzed in detail. As the electrolyte concentration varies, the effective interfacial tension changes rapidly. The testing data show that, the pressure-induced infiltration behavior is not only determined by the cations, but also highly dependent on the anion species.

The transport behaviors of solvated ions in nanopores can be field responsive, providing a novel method to develop interactive protection systems. As an external electric field is applied, the observed change in effective solid-liquid interfacial tension is contradictory to the prediction of classic electrochemistry theory.

To simplify the materials handling, a polypropylene-matrix composite material is produced. When the temperature is relatively low, the matrix dominates the system behavior. When the temperature is relatively high, with a sufficiently large external pressure the polymer phase can be intruded into the nanopores, providing an energy absorption mechanism.

Chapter 1 Background

Protecting key infrastructures and personnel from blast, collision, and impact attacks is of great importance to may military, homeland security, and commercial applications. For example, a considerable portion of the soldiers deployed in the battlefields in Iraq and Afghanistan suffer Traumatic brain injury (TBI) and/or blast lung injury (BLI), which significantly affected their quality of life, their families, and the healthcare providing system. To reduce and eventually prevent such damages and injuries, high performance energy absorption materials and structures must be developed.

1.1 Conventional Energy Dissipation Materials and Mechanisms

1.1.1 Solid Materials and Structures
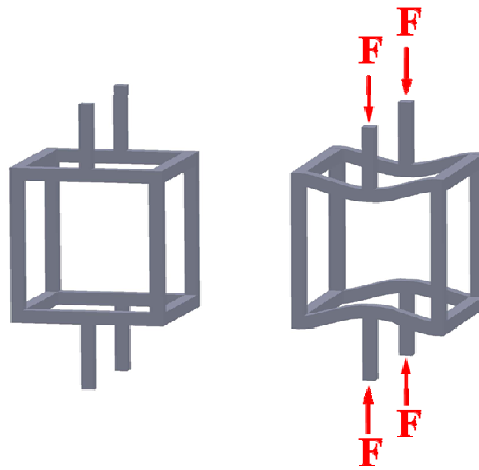
Figure 1-1 Schematic of the buckling of a foam cell

Typical energy absorption materials, such as foams, foam-based sandwichs, shape-memory alloys, etc have been widely used [1-5]. The energy dissipation mechanism of these systems is related to the internal damaging. As shown in Figure 1-1, when a sufficiently high external loading is applied on a foam, the cellular structure would buckle and dissipate the impact energy to thermal energy [3].
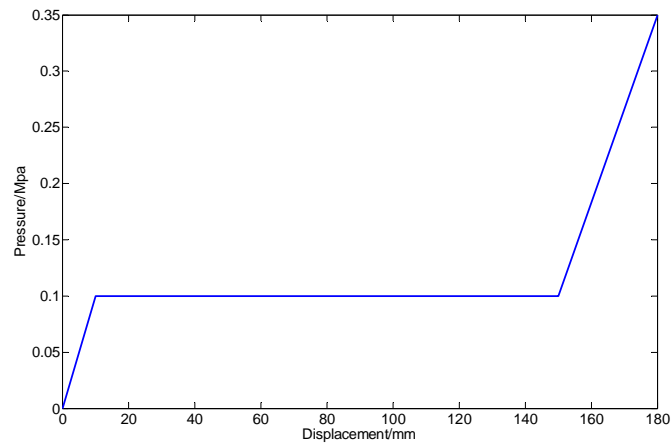
Figure 1-2 Compressive force vs deformation for polyurethane foam block

Figure 1-2 is a typical compression isotherm of a polyurethane foam. When the external force reaches a critical value, a stress plateau is observed at 0.1 MPa [3], which is associated with the crushing of the foam cells. The critical force and pressure are referred to as the crushing force and the crushing pressure, respectively. Theoretically, the transmitted pressure should be equal or smaller than the crushing pressure, if the energy absorption capacity of the foam is not exceeded. According to the static compression testing result (Figure 1-2) the energy absorption capacity of this material is about 3 J/g.

A foam-based sandwich composite is composed of strong, stiff skins with a soft core [4].

The two hard skin layers are employed to distribute the impact loading more uniformly so that more cells of the foam can be involved in the energy dissipation process.

Table 1-1 Summary of energy dissipation mechanisms

Mechanism	Commonly studied EAM	Unsolved problems
Buckling of cells and columns	Foams, honeycombs, CNT forests	Prevent shear localization Reduce response time
Debonding, fracture, voiding	Composites, ductile metals/alloys	Promote bulk distributed damage
Internal friction	CNT forests, STL, granular composites	Maintain ultra-steep velocity gradients

Table 1-1 summarizes the major energy absorption mechanisms that are currently being utilized. Usually, a conventional energy dissipation system only contains solid components. For mitigation of blast attacks, there are several major issues: 1) Bio-tissues may fail at only 0.01 MPa [6], much smaller than the crushing pressures of the foams of high energy-absorption capacities. Therefore, very often the protection devices have to be massive and bulky. 2) Since crushing is the major energy dissipation mechanism, permanent deformation occurs during the process of energy dissipation; thus, the reusability of the system is poor. For instance, the Mullins' effect [5] can be observed at repeated loading-unloading cycles; that is, the energy absorption capacity of the system keeps decreasing as the crushing pressure is reduced. 3) Although the hard skins can be used, the system response may still be quite localized. Even in a low-velocity impact test, a foam-based sandwich structure typically fails in a shear mode. 4) As loading rate increases, the rate embrittlement effect, i.e. the cell buckling time is longer than the loading time, can be pronounced. For example, at a blast front, the pressure rises to the peak value in a few

microseconds, while the energy absorption mechanisms of a conventional protection material (e.g. cell buckling) take a few fraction of milliseconds. Thus, although the overpressure plateau following the blast front can be reduced, the front itself can directly pass through the protection layer as if the foam were "transparent".

1.1.2 Shear Thickening Fluids

In the past a few decades, new materials with low densities, high strengths, and high energy absorption capacities have been developed, such as Kevlar [7]. However, 20-50 layers of these fabrics are required for typical ballistic and stab threats [7, 8]. As a result, the protection armor is bulky and inflexible.

To make the protection layer more conformable, an advanced sandwich structure was analyzed by Y. Lee et al. [8]. In this energy absorption system, the Kevlar fabric was impregnated by a special fluid, shear thickening fluid (STF). STFs demonstrated non-Newtonian behaviors, which was first discovered in 1970s [9]. The non-Newtonian behavior depends on the shear rate and the normal pressure. In general, at low shear rates, shear thinning (liquid-like behavior) occurs; while at high shear rates, shear thickening (solid-like behavior) takes place [10]. Although the mechanism of shear thickening is still under investigation, two possible processes are identified: the order-to-disorder transition or the formation of hydroclusters [11].

According to the results of ballistic tests and conventional drop tower tests [7, 8], the impregnation of fabrics in STFs increases both the energy absorption capacity and the efficiency

of the system. In addition, the liquid-solid transition is reversible; that is, the system is reusable. The STF can be utilized to efficiently mitigate ballistic impacts, punctures and cuts, etc. However, it can only be used in shear, not under compressive loads. Moreover, if the shear rate is relatively low, only shear thinning occurs.

1.2 Nanoporous Materials Functionalized Liquids

1.2.1 Energy Dissipation Mechanism of Nanoporous Materials Functionalized Liquids

Figure 1-3 A liquid suspension of nanoporous particles

In order to develop advanced protection materials working under compressive loads, the most critical loading mode for TBI/BLI mitigation, we investigated nanoporous-materials-functionalized (NMF) liquids. A NMF liquid is a liquid suspension of nanoporous particles (Figure 1-3). Typical materials of the nanoporous particles are silicas, carbons, zeolytes, celytes, metals, polymers, and ceramics. Most of these materials have hydrophilic surfaces, i.e. when the particles are mixed with water or aqueous solutions of

electrolytes, the nanopores would be spontaneously wetted and occupied by the liquid phase and no energy can be dissipated.

Thus, the inner surfaces of nanopores have to be specially treated to make them hydrophobic. The treated particles are non-wettable and can keep the liquid phase separated from the solid phase. When an external pressure is applied and reaches a critical value, the capillary effect is overcome. Consequently, the liquid phase can be intruded into the nanopores. As the ultra-large pore surface (100 m^2/g ~1200 m^2/g) is exposed to the confined liquid, tremendous amount of energy is dissipated [12]. The liquid motions studied in this dissertaion were only focused on solid-liquid interactions. There is another indispensable factor - the gas phase in the confined nanopore environment. The confined gas molecules behaviors vary with the nanopore sizes, which significantly affect the defiltration of the liquid phase [13]. However, it is not directly to the infiltration pressure of the liquid phase and the amount of captured energy.
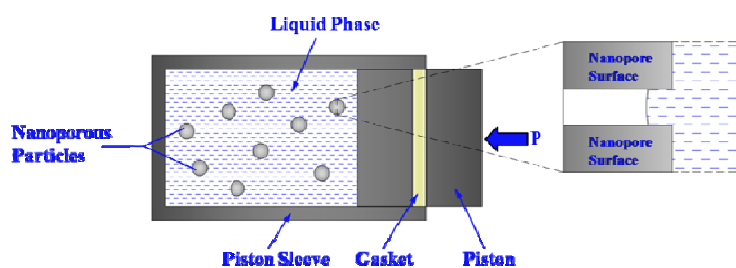
Figure 1-4 Schematic of the mechanism of NMF liquids

The mechanism mentioned above is only focused on a single nanopore. At the macrosopic level, consider a particle consisting of a large number of nanopores and/or a cluster of many nanoporous particles. The system can be regarded as a special "sandwich" structure of millions-billions of hard-soft layers. The nanopore walls with very high strength and stiffness are

the "hard layers", while the nanopores and the confined soft matter are the "soft layer". It is well

known that such a layer-stack structure helps with "capturing" stress waves [14]. Due to the

impedance mismatch of the hard and soft layers, a major portion of the energy would be "locked"

in the nanopores, together with the energy-carrying medium. Moreover, if the ligament length is

small, the nanopore walls become nearly incompressible, and, therefore, little compressive wave

can transmit across them.

1.2.2 Advantages of Nanoporous Materials Functionalized Liquids

The NMF liquids have a number of advantages. 1) They have high energy absorption

efficiency, associated with the large specific surface area of the nanopores, as well as the

energy-capture mechanism discussed above. 2) The materials are light weight and small size. The

density of typical nanoporous particles is 0.4 g/cm^3 and the size of particles is in the range of

1-100 μm. Due to the high energy absorption efficiency, the volume of the system can be

minimized. 3) NMF liquids can be used to filter out only the harmful peaks of external loading,

instead of absorbing all the energy carried by the impact [15]. 4) The energy dissipation is

ultra-fast, which can be completed in a few microseconds, ideal for mitigating blast fronts.

1.2.3 Control of Working Pressures

The absorbed energy of a NMF liquid can be expressed as

$$U=P_{in}V_{in} \tag{1.1}$$

where P_{in} is the external pressure required to overcome the capillary effect, which will be referred to as the infiltration pressure in this dissertation; and V_{in} is the specific pore volume of the materials. Note that the infiltration pressure determines the working pressure. It varies with the pore size and the surface properties. When the impact pressure is lower than P_{in}, energy absorption cannot be activated.

Therefore, one way to control the energy absorption properties of the system is to select nanoporous particles with appropriate pore size. The criteria of selection include: 1) The infiltration pressure, P_{in}, must be lower than the safety threshold; and 2) The energy capacity must be as large as possible. According to Equation (1.1), as a first-order assessment, the energy absorption capacity is proportional to P_{in}, described as (see Figure 1-5)

$$P_{in} = 2\Delta\gamma/r \tag{1.2}$$

where $\Delta\gamma$ is the effective surface tension, r is the effective pore radius.
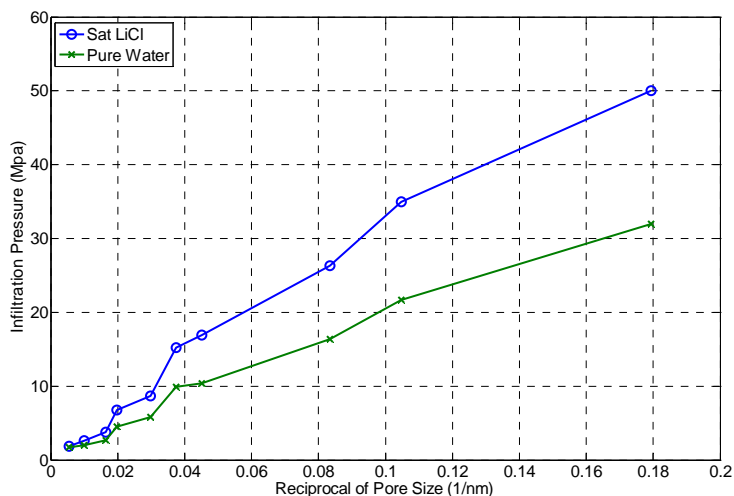
Figure 1-5 Relationship between the infiltration pressure
and the reciprocal of nanopore size

The materials shown in Figure 1-5 were nanoporous silica. The liquid phases were saturated LiCl solution (blue) and distilled water (green), respectively. The effective surface tension was controlled through certain surface treatment which will be discussed in detail in Chapter 2. Note that Equation (1.2) can be rewritten as

$$P_{in} = C/r \qquad\qquad (1\text{-}3)$$

where C is a constant determined by the surface treatment conditions and the liquid properties. The nanopore sizes and the corresponding infiltration pressures are listed in Table 1-2.

Table 1-2 Nanopore sizes and corresponding infiltration pressure

Nanopore Radius (nm)	5.6	9.6	12.0	22.2	26.7.	33.6	50.6	61.0	102	184.8
P_{in} with Sat. LiCl (MPa)	50	34.95	26.3	16.9	15.2	8.7	6.8	3.8	2.655	1.9
P_{in} with Water (MPa)	32	21.7	16.4	10.4	9.9	5.8	4.5	2.7	2	1.75

1.3 Liquid Behavior in Nanopores

In Figure 1-5, for the same nanoporous materials, when distilled water is used as the liquid phase, P_{in} decreases as compared to the system based on. It can be seen clearly that the liquid phase has significant effects on the performance of the system. In order to control the energy dissipation properties, it is imperative to understand the liquid behavior in nanopores, which is a new scientific area. As the liquids are confined in nano-environment, there may be only a few liquid molecules that can enter the nanopores simultaneously. Thus, the continuous theories cannot be directly implemented to explain the phenomena. To understand the liquid behaviors in

the nano-environment, we investigated a variety of internal and external factors, including the surface treatment, the viscosity, the cations, the anions, temperature, and the external electrical fields.
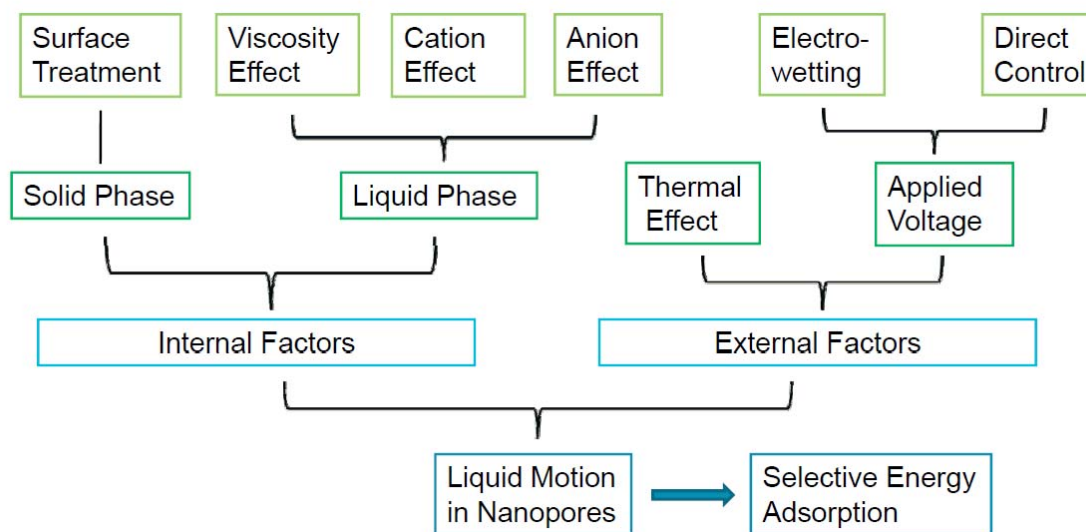
Figure 1-6 Factors of liquid behavior in nanopores

Figure 1-6 shows the structure of this dissertation. First, surface treatment is discussed. It is critial to control the degree of hydrophobicity of the inner surfaces of nanopores. The surface reagents and treatment conditions determine the hydrophobicity, the morphology, the modified nanopore size, etc. Second, the properties of the liquid phase are investigated, such as viscosity, the types of ions, and the concentration of ions. Finally, the effects of external fields are studied.

References

[1]   Kong, X; Qiao, Y. Thermal effects on pressure-induced infiltration of a nanoporous system. Philosophical Magazine Letters. 2005. 85, 331-337.

[2]   Song, B; Chen, W. SHPB techniques for characterizing soft materials. Latin American Journal of Solids and Structures. 2005. 2, 113-152.

[3]   Shim, V; Yap, K. Static and impact crushing of layered foam-plate systems. Journal of Mechanical Sciences. 1997. 39, 69-86.

[4]   Hazizan, M; Cantwell, W. The low velocity impact response of foam-based sandwich structures. Composites Part B: Engineering. 2002. 33, 193-204.

[5]   Shen, Y; Golnaraghi, F; Plumtree, A. Modelling compressive cyclic stress–strain behaviour of structural foam. Journal of Fatigure. 2001. 23, 491-407.

[6]   Daniel, J; Ng, T; Garner, S; Arias, A; Coleman, J; Liu, J; Jackson, R. Pressure sensors for printed blast dosimeters. Ninth IEEE Sensors Conference. 2010. 2259-2263.

[7]   Decker, M; Halbach, C; Nam C; Wagner, N; Wetzel, E. Stab resistance of shear thickening fluid (STF)-treated fabrics. Composites Science and Technology. 2007. 67, 565-578.

[8]   Lee, Y; Wetzel, E; Wagner, N. The ballistic impact characteristics of Kevlar woven fabrics impregnated with a colloidal shear thickening fluid. Journal of Materials Sciences. 2003. 38, 2825-2833.

[9]   Hoffman, R, Discontinuous and dilatant viscosity behavior in concentrated suspensions.II. Theory and experimental tests. Journal of Colloid and Interface Science. 1974. 46, 491-506.

[10] Wetzel, E; Lee, Y; Egres, R; Kirkwood, K; Kirkwood, J; Wagner, N. The effect of rheological parameters on the ballistic properties of shear thickening fluid (STF)-Kevlar composites. NUMIFORM. 2004. 288-293.

[11] Lin, H; Hwu, W; Ger, M. The mechanism of shear thickening fluid with nanoparticles applied to liquid armor. Microprocesses and Nanotechnology. 2007. 5, 212-213.

[12] Kong, X; Qiao, Y. Improvement of recoverability of a nanoporous energy absorption system by using chemical admixture. Applied Physics Letters. 2005. 86, 151919.

[13] Qiao, Y; Cao, G; Chen, X. Effects of gas molecules on nanofluidic behaviors. Journal of the American Chemical Society. 2007. 129, 2355-2359.

[14] Lu, G; Yu, T. Energy absorption of structures and materials. Woodhead Publishing. 2003.

[15] Surani, F; Kong, X; Qiao, Y. Two-staged sorption isotherm of a nanoporous energy absorption system. Applied Physics Letters. 2005. 87, 251906.

Chapter 2 Surface Treatment

2.1 Introduction

As discussed in Chapter 1, an NMF liquid, also referred to as nanoporous-energy-absorption system (NEAS) in this dissertation, contains two phases: a nanoporous phase, which is often in the form of micrometer (μm) sized particles, and a liquid phase in which the nanoporous particles are immersed. The properties of the inner surfaces of nanopores must be appropriately controlled so that the effective solid-liquid interfacial tension, γ_{sl}, is larger than $\gamma_s+\gamma_l$, where γ_s and γ_l are the effective surface tensions of the nanopore wall and the liquid, respectively; that is, work needs to be done to expose the nanopore surface to the liquid. Thus, at rest the repelling effect of the nanopore surfaces would keep the liquid phase out of the nanopores. Otherwise, the nanopores may be soaked up spontaneously and the bulk modulus of the system would be close to those of the liquid phase, shown in Figure 2-1.
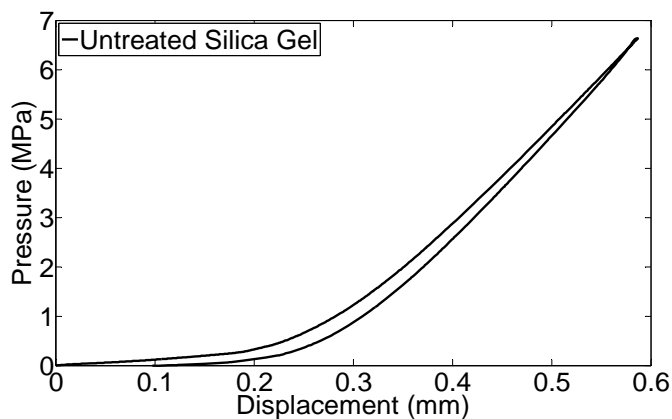
Figure 2-1 Typical compression isotherm curve of an untreated nanoporous silica gel

Modifying surface properties has long been an active research area, which is of both

prime scientific interest and important technological relevance [1]. In general, one of the efficient

surface treatment methods is to graft a hydrocarbon layer on the substrate surface [2], shown in

Figure 2-2. If the surface group density is sufficiently high, the surface properties are dominated

by the grafted surface groups. The thickness of the layer, t, which affects the effective nanopore

radius r' and the pore volume, is varied with the surface reagents and the surface treatment

conditions. Through appropriate surface treatment, the nanopore surfaces become hydrophobic

and as an external pressure is applied, the liquid can be compressed into the nanopores,

accompanied by a large increase in system free energy, the amount of which is correlated to the

total surface area. Thus, the NEAS can be regarded as an effectively compressible liquid, relevant

to advanced damping and protection applications [3, 4], show in Figure 2-3. Typically, the

nanoporous structure collapses at over 750 MPa [5], which is much higher than the infiltration

pressure of the NMF liquid system.
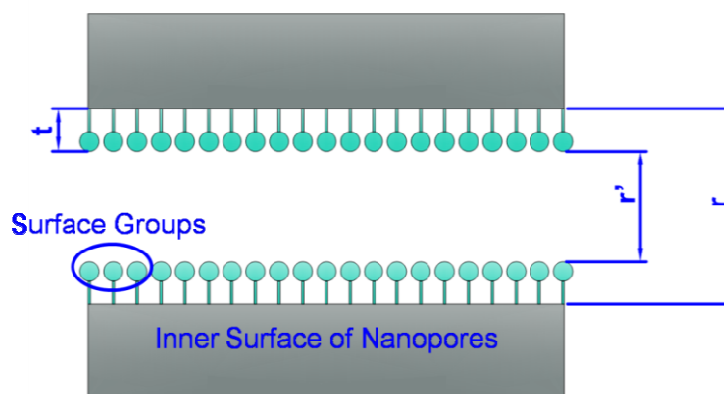
Figure 2-2 Modified nanopores
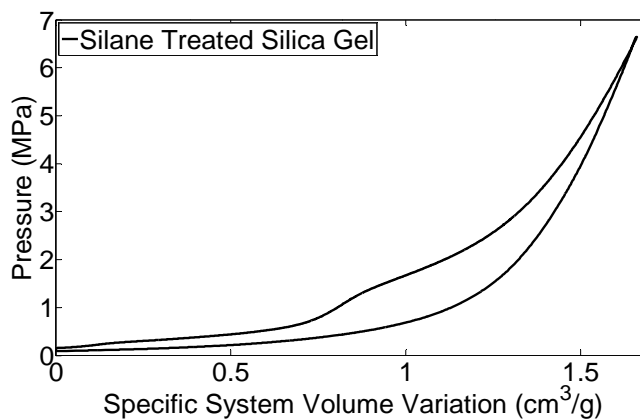
Figure 2-3 Typical compression isotherm curve of a surface treated nanoporous silica gel

2.2 Surface Treatment Procedure

Widely used surface agents include organosilicon compounds with the chemical formula

$R_{4-n}SiX_n$, where R is the alkyl group, C_mH_{2m+1}, and X can be Cl, OCH_3, OC_2H_5, $N(CH_3)_2$, etc [2].

Some commonly used surface groups and their effective layer thicknesses are listed in Table 2-1.

Table 2-1 Surface groups and the bonded layer thickness

Surface group	Chemical formula	Effective layer thickness[*] (nm) [6, 7]
Chloro-trimethyl-silane	$(CH_3)_3SiCl$	0.3
Chloro-dimethyl-octyl-silane	$C_8H_{17}Si(CH_3)_2Cl$	0.8
Chloro-dimethyl-octadecyl-silane	$C_{18}H_{37}Si(CH_3)_2Cl$	1.4

* The effective layer thickness, t, varies with the nanopore size and the treatment time.

The interaction between the hydroxyl groups and these organic compounds is:

$$SiO_2\!\!-\!OH + R\text{-}Si\text{-}Cl \longrightarrow SiO_2\!\!-\!O\text{-}Si\text{-}R + HCl \tag{2.1}$$
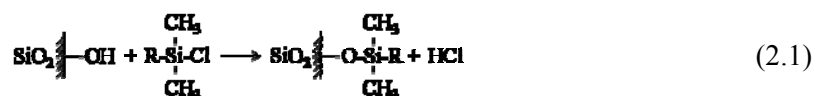
where R is the alkyl groups. Sometimes trichloro modifiers, typically trichloro-dodecyl-silane, are

also used. At the initial stage, the Si-Cl groups react with a portion of the hydroxyl groups on the

substrate surface, and the others remain unreacted. When a well-controlled amount of water is

added, polymer-like chains are generated, which increases both the surface coverage and the

thickness of the surface layer.

$$SiO_2 \!\!-\!\! OH + R\text{-}\underset{Cl}{\overset{Cl}{\underset{|}{\overset{|}{Si}}}}\text{-}Cl \longrightarrow SiO_2 \!\!-\!\! O\text{-}\underset{Cl}{\overset{Cl}{\underset{|}{\overset{|}{Si}}}}\text{-}R + HCl \xrightarrow{H_2O} SiO_2 \!\!-\!\! O\text{-}\underset{OH}{\overset{OH}{\underset{|}{\overset{|}{Si}}}}\text{-}R + 2HCl \qquad (2.2)$$
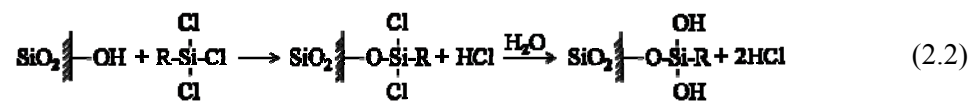
Figure 2-4 shows the procedure of surface treatment. Usually, end capping is optional,

which is equivalent to a second round of surface treatment by using surface groups of smaller

molecular sizes, such as chloro-trimethyl-silane. It is used when surface groups of relative long

alkyl chains are employed in the surface treatment. The details of surface treatment procedure are

described in Appendix A and B.
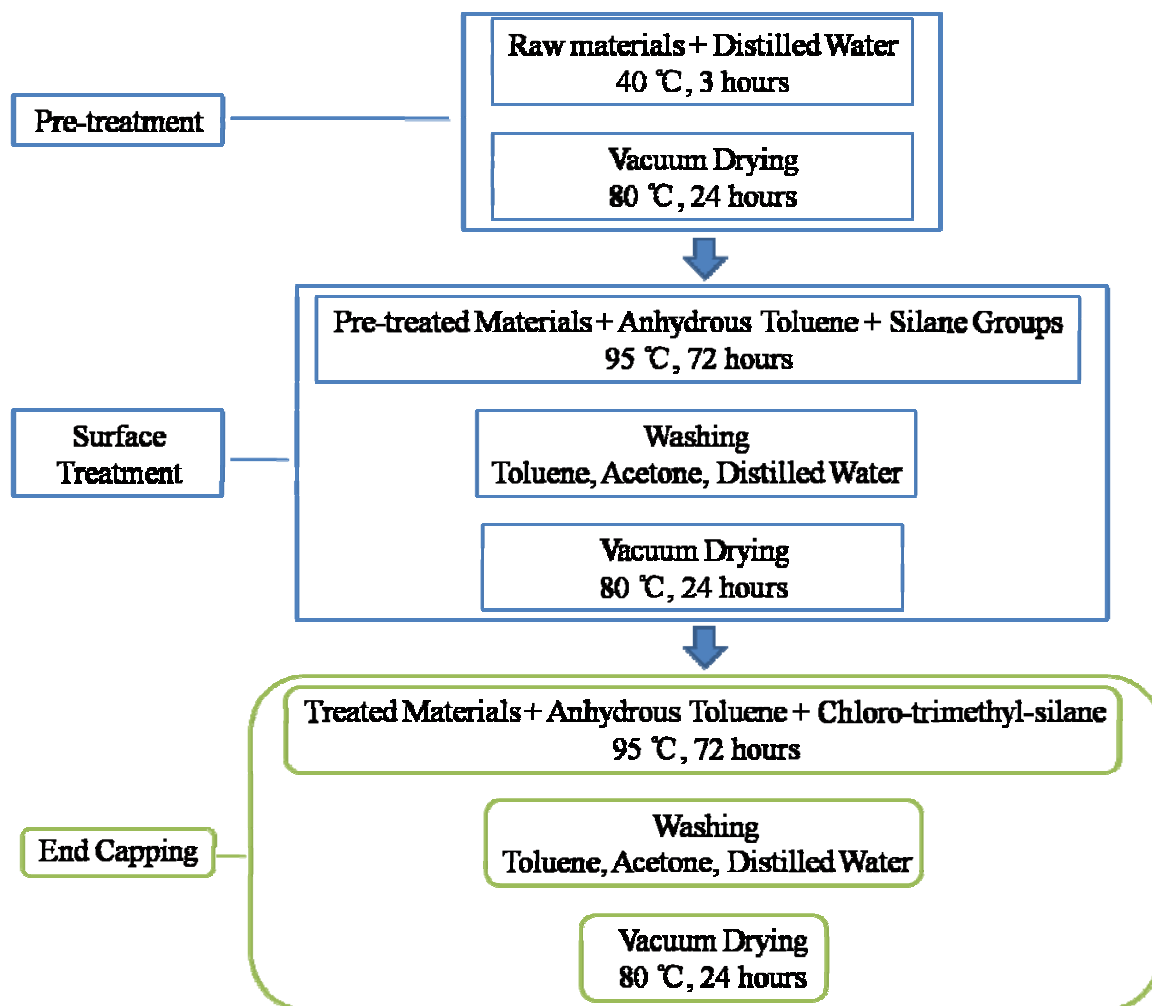
Figure 2-4 Typical procedure of surface treatment

2.3 MHA Treatment

Usually, the properties of a treated surface are quite stable; that is, unless degradation or leaching occurs, its behavior does not vary. To produce a "switchable" surface, the length of the surface groups must be sufficiently long and the chain configuration should be field responsive, so that the surface morphology can be adjusted. This concept has been investigated for large solid surfaces [8, 9]. The surfaces groups can be long chains with charged end groups. As a potential

difference is applied normal to the solid-liquid interface, the chain may be either bent or straight, exposing different chain sections to the exterior, and, thus, the overall surface properties are controllable. This technique may also lead to a a promising method that can stably suspend nanoporous particles in a liquid phase.

2.3.1 Experimental

Figure 2-5 Micromeritics ASAP-2020 porosimetry analyzer

We investigated a nanoporous carbon, provided by Cabot (BP2000). The as-received material was in powder form, with the particle size of about 50 μm. By using a Micromeritics ASAP-2020 porosimetry analyzer (Figure 2-5), its specific nanopore volume was measured as 2.2

cm^3/g; the specific nanopore area was 1200 m^2/g; and the average nanopore size was 17 nm. The material surface was cleaned in a tube furnace at 450 ℃ in nitrogen for 12 hours, followed by repeated washing in acetone and warm water and vacuum drying at 80 ℃ for 12 hours. Two surface modifiers were studied: chloro-trimethyl-silane and 16-mercaptohexadecanoic acid (MHA) [10, 11].

The first batch of material was sealed in a round bottom flask with 10 mL of 2.5% anhydrous toluene solution of chloro-trimethyl-silane. The mixture was stirred at 90 ℃ for 4 hours in a thermal mantle, followed by repeated rinsing in dry toluene, acetone and warm water, and vacuum drying at 80 ℃ for 24 hours. The second batch of material was first treated by chloro-trimethyl-silane and then treated by MHA. The molecular formula of MHA is $HS(CH_2)_{15}CO_2H$. The body of the chain is formed by trans-CH_2 links, which are hydrophobic [12]. The carboxylate end group is negatively charged, which may respond to an external electric field. The particles were mixed with 150 mL of anhydrous toluene and 2 g of MHA in a sealed flask. The mixture was stirred at room temperature for 10 min and refluxed at its boiling point for 48 hours. A drying tube was attached to the top of the reflux apparatus. The material was then filtered, washed in dry toluene, methanol, and deionized water, and dried in vacuum at 80 ℃ for 6 hours. The third batch of material was directly treated by MHA. The MHA was injected into the dry toluene in a round bottom flask with the mass ratio of 15 mg per ml. The mixture was stirred gently for 20 min at room temperature when 480 mg of nanoporous carbon was added. By using a thermal mantle, the temperature was maintained at 95 ℃ and the carbon-liquid mixture was

refluxed for 72 hours. Then, the carbon powders were filtered and thoroughly rinsed by dry toluene, acetone, and warm water, and dried in vacuum at 120 ℃ for 12 hours. The surface reaction happened at the hydroxyl sites [13, 14].

About 0.3 g of batch 1 or batch 2 sample was mixed with 6 g of saturated aqueous solution of potassium chloride (KCl) in a stainless steel cylinder. A steel piston was intruded into the cylinder by a type 5582 Instron machine at a constant rate of 0.5 mm/min, applying a quasi-hydrostatic pressure on the liquid phase. The cross-sectional area of the piston, A_p, was 286 mm^2. As will be discussed below, in a certain pressure range, an infiltration plateau could be observed. Once the infiltration was completed, the piston was moved out of the cylinder at the same rate. Figure 2-6 shows typical sorption isotherm curves, demonstrating the pressure as a function of the system volume change. During the testing procedure, the system temperature was controlled by a water bath at either 20 ℃ or 50 ℃.
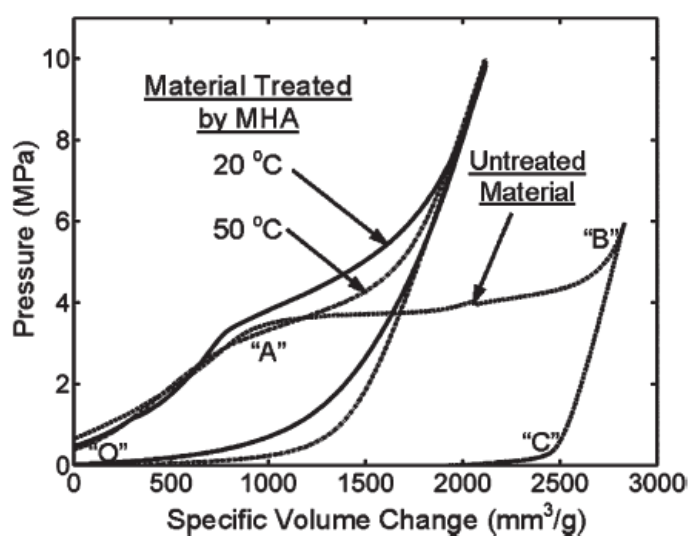
Figure 2-6 Typical infiltration curves of batch 1 and 2 with KCl solution
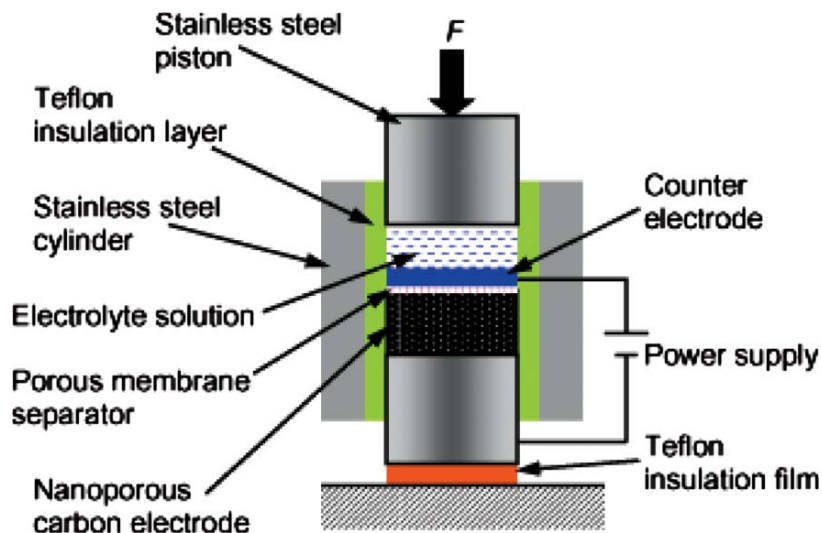
Figure 2-7 Schematic of the experimental setup

The batch 3 BP2000 sample was uniformly mixed with polyvinylidene fluoride with the mass ratio of 4:1. The mixture was compressed in a steel mode by the Instron machine under 5 MPa, forming disk-shaped electrodes. The diameter of the electrode disk was 12 mm and the thickness was 0.5 mm. In a stainless steel cylinder, as depicted in Figure 2-7, the electrode was separated from a platinum counterelectrode by a 50 μm thick porous polyethylene membrane separator and immersed in 20% aqueous solution of lithium chloride (LiCl). The electrolyte was added to enhance the liquid conductivity. The system was sealed by a stainless steel piston. The inner surface and the bottom of the cylinder were insulated by thin Teflon layers. By suing a DC power supply, a potential difference could be applied across the electrode and the counterelectrode. The voltage was either 0, +0.5, or -0.5 V. As the voltage was maintained constant, the material was tested as the same loading and unloading conditions as batch 1 and batch 2 samples. Figure 2-8 shows the typical sorption isotherm curves.
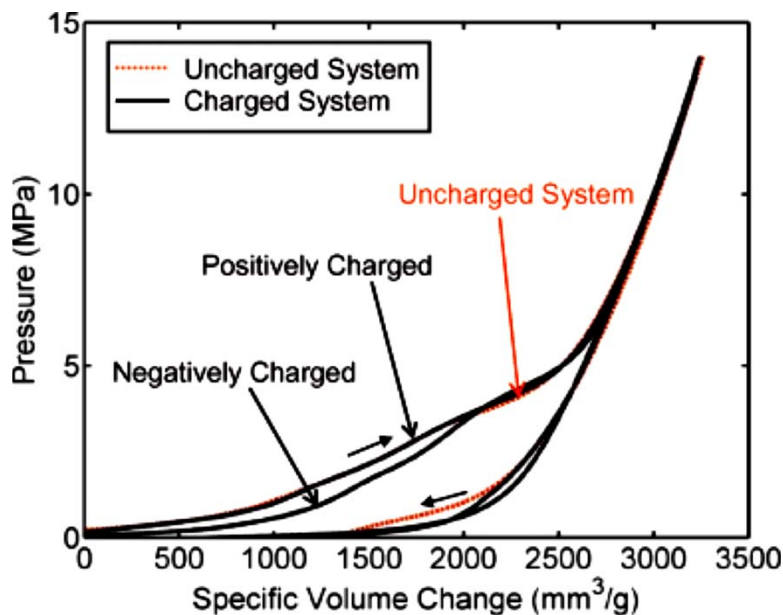
Figure 2-8 Typical sorption isotherm curves of batch 3 with LiCl solution

2.3.2 Results and Discussion of Silane Treatment

In the silane treatment process, the silane molecules react with the hydroxyl sites at both the inner surfaces of the nanopores and the outer surfaces of the particles, forming –CH$_3$ layers on the nanoporous carbon surfaces [15]. They repel water molecules, and, thus, the treated carbon surface becomes hydrophobic. When the silane treated carbon powders are added in the KCl solution, even after prolonged mixing, no stable suspension can be formed. The lightweight carbon particles would float on the top, and the clear liquid phase is left below. As the heterogeneous system is compressed by a quasi-static loading, initially when the pressure is relatively low, the carbon powder layer and the liquid layer deform separately. While the liquid phase is nearly incompressible, the carbon powders are only loosely packed and, thus, can be condensed easily. As shown in Figure 2-6, the system volume decreases with the increase in

pressure (section OA), with the slope of sorption isotherm curve of about 3.75 kPa·g/mm^3. When

the pressure is increased to nearly 3.5 MPa, an abrupt transition from the ramp (OA) to a plateau

(AB) is observed, which should be attributed to the infiltration of the pressurized liquid into the

nanopores. The addition of the electrolyte increases the surface tension of the liquid phase, and

makes the transition clearer [16]. The plateau is flat, indicating that the effective viscosity of the

confined liquid is low, so that the internal friction effect is negligible. The reduction in liquid

viscosity at small length scale is associated with the breakdown of the continuum interface

structure and the insufficient space for the development of velocity profile [16]. The infiltration

continues from "A" to "B", after which the slope of the sorption isotherm curve rapidly increases,

indicating that the nanopores are filled. The width of the infiltration plateau is around 1.8 cm^3/g,

close to but smaller than the gas adsorption measurement result of porosity. The difference

between the effective nanopore volumes in liquid infiltration and gas adsorption tests may be

related to the van der Waals distance of water molecules, which is about 0.2-0.3 nm [17].

Immediately next to the large nanopore surface, the inaccessible space is 240 to 360 mm^3/g. Due

to the relatively short treatment time, the surface coverage of the silane groups is far from being

saturated. If the treatment time is increased to 8 hours, the infiltration pressure would be

increased by about 20%. As the surface density of the silane groups is relatively low, their

influence on the effective pore volume is only secondary.

    When the pressure is lowered, the unloading path (BC) does not overlap with the loading

path; that is, the sorption isotherm curve is highly hysteretic. The effective compressibility of the

system is nearly the same as that at the high-pressure range of the loading path, larger than both

of the slopes in sections OA and AB. The effective compressibility should be mainly determined

by the machine compliance. Not until the pressure is reduced to about 0.2 MPa does the system

volume recovery start to accelerate, forming a defiltration plateau (CO). The difference in the

loading and unloading behaviors should be related to the irreversibility of the motion of the

confined liquid. Under a high pressure, the liquid molecules and ions can overcome the energy

barrier among the tetrahedral sites when they slide along the nanopore surface into the interior of

a nanoporous particle. During unloading, since no negative pressure difference can be applied, the

confined liquid must rely on thermal motion to overcome this internal friction effect, which needs

to be aided by additional driving force [18, 19]. The required driving force can be estimated as

3.3 MPa, the difference between the infiltration pressure and the defiltration pressure. As an

order-of-magnitude assessment, the difference in effective interfacial tensions in infiltration and

defiltration is about 13 mJ/m^2, which looks plausible compared with the system free energy

variation associated with the direct interaction among the liquid and solid molecules [8].

2.3.3 Results and Discussion of MHA Treatment

For batch 2 samples, the MHA molecules react with the active hydroxyl sites at carbon

surfaces and form long chains with negatively charged end groups. With such a polar structure,

the surface tends to be hydrophilic, opposite to the effect of the silane groups. Since the repelling

effect of the neutral CH_3 end of a silane group to water molecules is based on the relatively weak

van der Waals interaction while the attraction effect of a charged MHA group is based on the strong hydrogen bond, the latter tends to be dominant. As a result, with the MHA treatment, the carbon surface becomes hydrophilic. As the treated BP2000 powders are mixed with the liquid, they can be suspended uniformly. After mixing and being at rest for 12 hours, no evidence of phase separation can be observed. Clearly, the surface charges keep the carbon particles separate.

If the inner surface modification at the inner surfaces of nanopres is similar to that of the particle outer surface, the inner surface would also be hydrophilic. Under this condition, once the BP2000 is mixed with the KCl solution, the nanopores would be soaked up spontaneously; and as the pressure is applied no further infiltration should be observed. The testing curve in Figure 2-6, however, exhibits a clear infiltration plateau, suggesting that the inner surfaces of nanopores are still hydrophobic. An interesting phenomenon is that, with the addition of the hydrophilic MHA groups, the pressure at the onset of infiltration does not vary much. Moreover, as the infiltration continues, the infiltration pressure significantly increases. At the end of infiltration, the pressure is nearly 7.5 MPa, higher than the initial infiltration pressure by more than 100%. The average slope in the infiltration plateau is around 3 $kPa \cdot g/mm^3$, only slightly smaller than that of the low-pressure section.
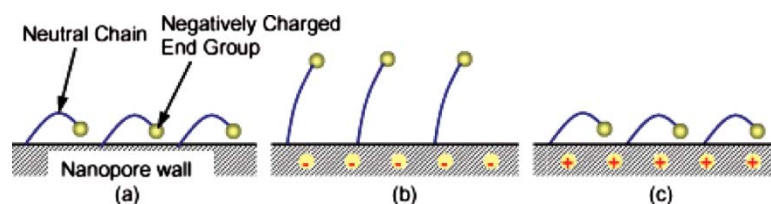
Figure 2-9 Schematic of the surface groups (a) at an uncharged surface; (b) at a negatively charged surface; and (c) at a positively charged surface

While there is no direct experimental method to determine the distribution profile of the surface group density inside the nanopores, since increasing MHA treatment time would not cause detectable changes in the sorption isotherm curve, the treatment effect is saturated. The high degree of hydrophobicity of the inner surface may be attributed to the unique chain configuration in the confining nanoenvironment, as depicted in Figure 2-9(a). In a nanopore, along the axial direction, the space is much less constrained than the radius direction. Thus, to minimized the system free energy, the relatively long MHA chains tend to extend along the pore wall, and, thus, the negatively charged end groups are buried by the nonpolar CH_2 groups. Note that the confinement effect of the nanopore walls on the configuration of silane groups is much less pronounced, since the silane group used is only around 0.3 nm long, much shorter than MHA. With the long MHA chains, the inner surfaces are of a high effective roughness, and, thus, when the liquid molecules and ions slide against the solid wall, the energy barrier that they must overcome at tetrahedral sites increases. As a first order approximation, the total internal friction acting on the confined liquid segment can be assumed proportional to the infiltration depth. Thus, as the infiltration volume increases, the pressure that is required to maintain the liquid intrusion rises linearly, as observed in the experiment. For each gram of the BP2000 sample, the additional work that the external pressure does during the infiltration process is around 2.3 J. That is, the energy barrier associated with liquid sliding along the nanopore inner surface is 1.9 mJ/m^2, about 10% of the effective solid-liquid interfacial tension. The increase in infiltration pressure may also be related to the surface charges of MHA groups at the outer surface near the nanopore opening,

which form an electric field normal to the liquid transport direction that requires additional work [20]. With the surface groups, the effective nanopore size is smaller, as depicted in Figure 2-2, which may promote the capillary effect, leading to a higher infiltration pressure. However, since these two factors are independent of the infiltration depth, they are secondary compared with the internal friction effect.

The presence of the MHA groups at inner nanopore surfaces is also validated by the gas adsorption analysis after the surface treatment. With the decoration of MHA groups, both the nanopore size and the nanopore volume are decreased. From the width of the infiltration plateau, the volume of the nanopores filled by the liquid phase is reduced by almost 35%, to 1.2 cm^3/g. Compared with the untreated material, it is equivalent to a reduction in nanopore radius about 0.5 nm. This value is much smaller than the MHA chain length (about 4 nm), which, again, implies that the MHA groups extend along the axial direction. The decrease in effective nanopore volume measured in the gas adsorption experiment is less pronounced, probably because of the relatively high mobility of gas molecules that can relatively easily penetrate into the space in between adjacent surface groups.

When unloading begins, defiltration occurs at a much lower pressure compared with infiltration, similar to the untreated material. The transition from the linear pressure decrease to the defiltration plateau, however, is much less sharp, indicating that even at a relatively high pressure defiltration can gradually take place, which can be attributed to the complicated configuration change of MHA chains subjected to the pressure variation.

Similar characteristics of infiltration and defiltration can be observed at an elevated temperature. In the temperature range under investigation, the infiltration volume is constant, indicating that the configuration of MHA chains at the inner surfaces does not vary. The liquid suspension is stable; that is, the surface charges at outer surfaces are not significantly affected. However, the infiltration pressure is considerably lowered by about 0.5 MPa, which agrees with previous experimental results on nanoporous silica gels that, when the temperature increase causes a decrease in the liquid surface tension, the effective solid-liquid interfacial tension is also reduced. The difference in infiltration and defiltration pressures is nearly the same, implying again that the MHA configuration, which dominates the energy barrier to the sliding of confined liquid segment along the inner surfaces, is relatively thermal insensitive.

Batch 3 samples are directly treated by MHA without prior silane treatment. Figure 2-8 shows that under ambient pressure the nanopores are empty. When a hydrostatic pressure is applied, it builds up a potential in the bulk liquid phase outside the nanoporous particles:

$$U = P^2 V / 2B \qquad (2.3)$$

where P is the pressure, V is the liquid volume, and B is the bulk modulus, which is around 2 GPa for aqueous solutions [21]. Thus, the driving force for liquid infiltration is

$$dU/dV = P^2 / 2B \qquad (2.4)$$

At the equilibrium condition, the driving force is balanced by the effective infiltration resistance

$$R = \Delta \gamma \cdot A \qquad (2.5)$$

where $\Delta \gamma$ is the excess solid-liquid infiltration tension and A is the increase in solid-liquid interface

area. For the sake of simplicity, assume that $A \approx 2V/r$, with r being the effective nanopore radius. Hence,

$$dR/dV = 2 \cdot \Delta\gamma/r \tag{2.6}$$

For a given r, $U = R$ and $dU/dV = dR/dV$ must be satisfied at the same pressure, at which with an infinitismal increment in P, $U > R$, and $dU/dV > dR/dV$. Not only it is energetically favorable for the liquid phase to enter into the nanopores (i.e. V tends to decrease), but also the driving force of infiltration increases; that is, the bulk liquid phase becomes unstable. It continuously transforms to the confined liquid phase inside nanopores, until the nanopores are filled. The critical pressure is:

$$P_{in} = 2\sqrt{B \cdot \Delta\gamma} \tag{2.7}$$

Because the pore size of the BP2000 distributes in a certain range, the infiltration begins with the relatively large nanopores and end with the relatively small ones, resulting in the infiltration plateau in sorption isotherm curve. The width of the plateau is around 2 cm^3/g, similar to the measured porosity, as it should be. The profile of the infiltration plateau is determined by the pore size distribution.

As discussed previously, the grafted MHA groups tend to be in the bent configuration, as depicted by Figure 2-9(a). This is confirmed by the testing result that, once a negative 0.5 V voltage is applied across the solid-liquid interface, the infiltration pressure considerably decreases; i.e., the degree of hydrophobicity, $\Delta\gamma$, is reduced. As shown in Figure 2-9(b), at a negatively charged surface, the carboxylate end groups are repelled and the MHA chains tend to be straight. Hence, the polarity of the effective solid-liquid interface increases. Note that even at -0.5 V, the nanopore

surfaces are still hydrophobic, suggesting that only a relatively small portion of the MHA chains are straight. This may be attributed to the confinement effect of the nanopore walls that were frequently reported in recent research [22, 23]. Since the opposite walls are relatively close to each other, the negatively charged end groups repel each other against the graphene surface, so that the MHA chains tend to be bent. When the external electric field is applied, the surface electrostatics effect is suppressed and, thus, more chains are straight.

If the applied voltage is positive, as shown in Figure 2-8, the variation in sorption isotherm curve is negligible, since such a potential difference would not cause much change in configuration of bent surface groups (Figure 2-9(c)). According to Figure 2-8, upon the application of the negative voltage, the most pronounced variation in P_{in} happens at the beginning of the infiltration plateau, where P_{in} is relatively low and the corresponding pore size is relatively large. At the end of the plateau, where the nanopore size is relatively small, the variation in sorption isotherm curve is secondary. Clearly, the effect of MHA groups is reduced in the smallest nanopores, probably because of the difficulty in infiltration of the relatively large MHA molecules in the surface treatment process.

2.3.4 Conclusions

To summarize, the modification effects of MHA on the outer and inner surfaces of a nanoporous carbon are considerably different. On the outer surface, the charged MHA chains trigger a hydrophobic-to-hydrophilic transition, so that the carbon particles can be stably

suspended in an aqueous solution. On the inner surface, the effective degree of hydrophobicity at the onset of infiltration does not vary much, while as the infiltration continues the required pressure becomes considerably higher. This may be attributed to the anisotropic morphology in the confining nanoenvironment that the charged end groups are buried and the nonpolar chains are exposed to the liquid phase. It agrees with the observation that the infiltration volume decreases after the MHA treatment. These characteristics are not sensitive to the temperature increase, except that the infiltration pressure is lowered.

It is also validated experimentally that the wettability of inner surfaces of nanopores can be electrically controllable, with the modification of morphing surface groups. The confinement effects of nanopore walls lead to the unique surface configuration and the pore size dependence of modification effect.

Chapter 2, in part, is a reprint of the material as it appears in Journal of Materials Research. Lu, Weiyi; Han, Aijie; Kim, Taewan; Lim, Hyuck; Qiao, Yu. Effects of surface charging treatment on outer and inner surfaces of a nanoporous carbon. 24, 2471-2475 (2009). The dissertation author was the primary investigator/author of this paper.

Chapter 2, in part, is a reprint of the material as it appears in Applied Physics Letter. Lu, Weiyi; Han, Aijie; Kim, Taewan; Qiao, Yu. Effect of 16-mercaptohexadecanoic acid modification on liquid transport in a nanoporous carbon. 94, 223120. 1-3 (2009). The dissertation author was the primary investigator/author of this paper.

References

[1]   Adamson, A; Gast, A. Physical chemistry of surfaces. Wiley. 1997.

[2]   Staroverov, S; Fadeev, A. Apparent simplicity of reversed stationary phases for high-performance liquid-chromatography. Journal of Chromatography. 1991. 544, 77-98.

[3]   Surani, F; Qiao, Y. An energy-absorbing polyelectrolyte gel matrix composite material. Composites Part A-Applied Science and Manufacturing. 2006. 37, 1554-1556.

[4]   Kong, X; Surani, F; Qiao, Y. Effects of addition of ethanol on the infiltration pressure of a mesoporous silica. Journal of Materials Research. 2005. 20, 1042-1045.

[5]   Han, A; Punyamurtula, V; Lu, W; Qiao, Y. Deformation of a nanoporous silica under compressive loading. Journal of Applied Physics. 2008. 103, 084318.

[6]   Fadeev, A; Staroverov, S. Geometric structural-properties of bonded layers of chemically modified silicas. Journal of Chromatography. 1988. 447, 103-116.

[7]   Fadeev, A; Eroshenko, V. Study of Penetration of Water into Hydrophobized Porous Silica. Journal of Colloid and Interface Science. 1997. 187, 275-282.

[8]   Tang, C; Makohliso, S; Heuschkel, M; Sharma, S; Keller, B; Voros, J. Dynamic, electronically switchable surfaces for membrane protein microarrays. Analytical Chemistry. 2006. 78, 711-717.

[9]   Chen, G; McCandless, G; McCarley, R; Soper, S. Integration of large-area polymer nanopillar arrays into microfluidic devices using in situ polymerization cast molding. Lab on a Chip. 2007. 7, 1424-1427.

[10] Lahann, J; Mitragotri, S; Tran, T; Kaido, H; Sundaram, J; Choi, I; Hoffer, S; Somorjai, G; Langer, R. A reversibly switching surface. Science. 2003. 299, 371-374.

[11] Liu, Y; Mu, L; Liu, B; Zhang, S; Yang, P; Kong, J. Controlled protein assembly on a switchable surface. Chemical Communications. 2004. 1194-1195.

[12] Xia, Y; Whitesides, G. Soft lithography. Angewandte Chemie-International Edition. 1998. 37, 550-575.

[13] Han, A; Qiao, Y. Controlling infiltration pressure of a nanoporous silica gel via surface treatment. Chemistry Letters. 2007. 36, 882-883.

[14] Han, A; Lu, W; Punyamurtula, V; Kim, Taewan; Qiao, Y. Temperature variation in liquid infiltration and defiltration in a MCM41. Journal of Applied Physics. 2009. 105, 024309.

[15] Han, A; Chen, X; Qiao, Y. Effects of the addition of Electrolyte on liquid infiltration in a hydrophobic nanoporous silica gel. Langmuir. 2008. 24, 7044-7047.

[16] Chen, X; Cao, G; Han, A; Punyamurtula, V; Liu, L; Culligan, P; Kim, T; Qiao, Y. Nanoscale fluid transport: size and rate effects. Nano Letters. 2008. 8, 2988-2992.

[17] Cao, G; Qiao, Y; Zhou, Q; Chen, X. Water infiltration behaviours in carbon nanotubes under quasi-static and dynamic loading conditions. Molecular Simulation. 2008. 34, 1267-1274.

[18] Han, A; Punyamurtula, V; Qiao, Y. Heat generation associated with pressure-induced infiltration in a nanoporous silica gel. Journal of Materials Research. 2008. 23, 1902-1906.

[19] Qiao, Y; Punyamurtula, V; Han, A; Kong, X; Surani, F. Temperature dependence of working pressure of a nanoporous liquid spring. Applied Physics Letters. 2006. 89, 251905.

[20] Reihs, K; Voetz, M. A reversibly switching block copolymer surface. Langmuir. 2005. 21, 10573-10580.

[21] Eisenberg, D; Kauzmann W. The structure and properties of water. Oxford University Press. 2005.

[22] Gong, X; Li, J; Lu, H; Wan, R; Li, J; Hu, J; Fang, H. A charge-driven molecular water pump. Nature Nanotechnology. 2007. 2, 709-712.

[23] Zhou, R; Eleftheriou, M; Royyuru, A; Berne, B. Destruction of long-range interactions by a single mutation in lysozyme. Proceedings of the National Academy of Sciences of the United States of America. 2007. 104, 5824-5829.

Chapter 3 Effects of the Viscosity of Liquid Phase

3.1 Introduction

The study on nanofluidic behaviors has provided a solid basis for understanding solid-liquid interactions in nanoenvironments [1, 2]. Through molecular dynamics simulations, it was predicted that in a nanochannel, liquid molecules can form a one dimensional chainlike structure, and their transportation can be "frictionless", [3-6] primarily because at the nanometer level the ordinary shearing and flowing processes break down.

As a liquid infiltrates in a nanoporous material, the large nanopore surface can greatly amplify the solid-liquid interaction [7-10]. For instance, Li [7] analyzed the damping properties of a hydrophilic nanoporous silica plate soaked by water. As a bending moment was applied on the plate, water moved from compressive parts to tensile parts and thus a certain amount of energy was dissipated. The energy dissipation efficiency, which was measured by the amount of energy absorbed by a unit mass of material, however, was lower than the expected level, indicating that in the nanopores the effective liquid viscosity was smaller than that of the bulk phase. In another set of experiments, Kong and Qiao [11] reported that the capillary effect of nanoporous materials is more controllable. By applying a nominally hydrostatic pressure on a system containing a hydrophobic nanoporous silica gel immersed in water, as the pressure was sufficiently high the liquid phase could be forced into the nanopores. It is remarkable that as the loading rate increased, in a Hopkinson bar arrangement of impact test [12], the energy absorption efficiency was increased

significantly. Since the excess solid-liquid interfacial tension should be rate independent, the increase in energy dissipation capacity was attributed to the liquid viscosity. It is thus envisioned that if more viscous liquids, such as glycerin, are employed, the rate dependence of energy absorption can be promoted.

3.2 Experimental

We investigated pressure induced infiltration of a hydrophobic Fluka 100 C_8 reversed phase silica gel synthesized through a sol-gel templating technique. The material was in powder form, with the particle size of 15–35 μm. The nanopore surfaces were treated by silane groups, so that they were highly hydrophobic [13]. Through a gas absorption test, it was measured that the particles contained 0.55 cm^3/g of nanopores, with the average pore size of 7.8 nm and the standard deviation of 2.4 nm. The liquid phase was chosen as Aldrich 7757 glycerin ($C_3H_8O_3$). Its molecular weight was 92.09, the molecular size was about 0.3 nm, and the viscosity was 1.5 Pa·s. It was stored in a drying hood so as to minimize the exposure to moisture [14]. The polarity of glycerin molecule is quite high, and, therefore, it can be easily mixed with water and is nonwetting to the nanopore surface. Its viscosity is higher than that of water by more than two orders of magnitude. Due to the small molecular size, when subjected to a high pressure, glycerin molecules were able to enter most of the nanopores in the silica gel.

Figure 3-1 Stainless steel testing cell
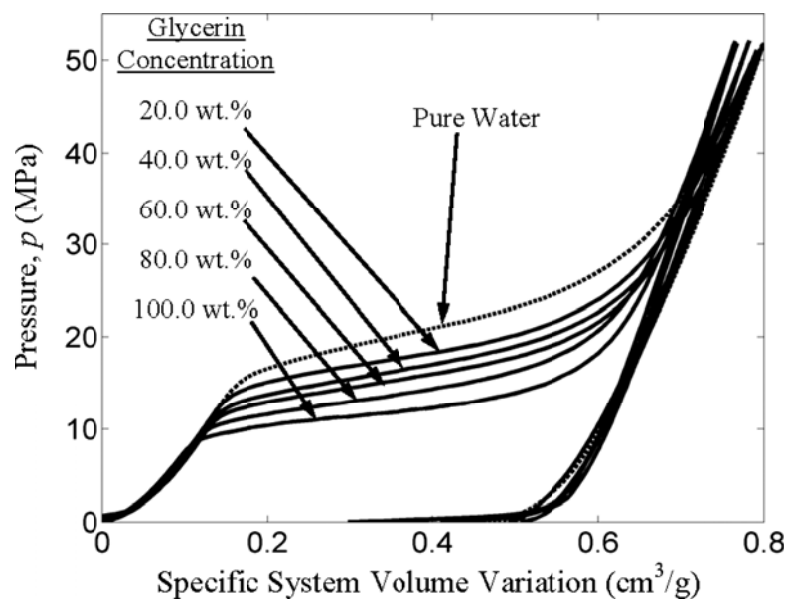
Figure 3-2 The sorption isotherm curves of systems of various glycerin concentrations

After mixing 0.5 g of the nanoporous silica gel with 7 g of aqueous solution of glycerin in a

stainless steel cylinder, the cylinder was sealed by a stainless steel piston (Figure 3-1). By using a

type 5582 Instron machine, the piston was compressed into the cylinder at a constant rate in the

range of 1–90 mm/min. When the pressure reached about 50 MPa, the crosshead was moved back

at the same speed. Figure 3-2 shows typical sorption isotherm curves of samples of various

glycerin concentrations at the loading rate of 1 mm/min. The glycerin concentration, c, varied from

0 (pure water) to 100 wt% (pure glycerin). Figure 3-3 shows the sorption isotherm curves of pure

glycerin based systems at various loading rates. The pressure was calculated as

$$P = F/A_p \tag{3.1}$$

with F being the force applied on the piston and A_p the cross-sectional area of the piston. The

specific system volume change was defined as

$$\Delta V = A_p \delta_p / m \tag{3.2}$$

with δ_p being the piston displacement and m the mass of the silica gel.
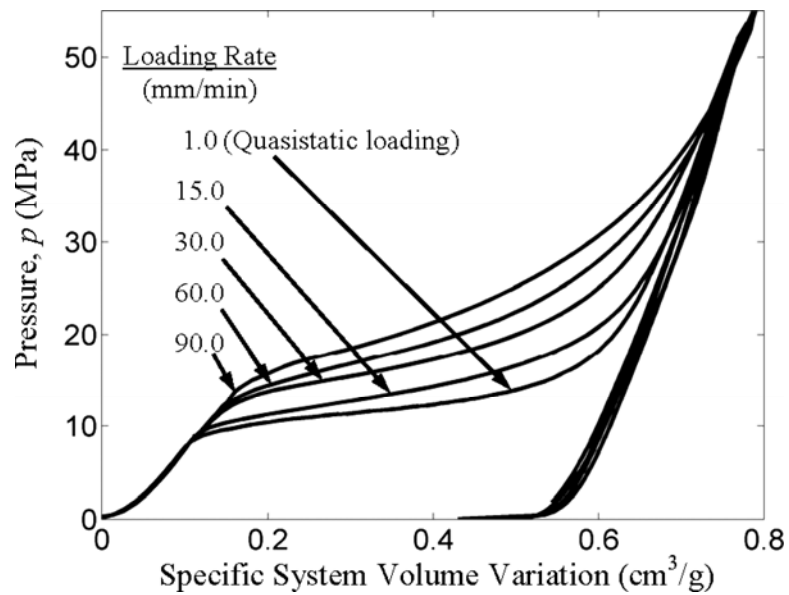
Figure 3-3 The loading rate effect on the pure glycerin based system

3.3 Results and Discussion

Through Figure 3-2, it can be seen clearly that the nanopore surfaces are lyophobic. As the

pressure is relatively low the system response is similar with that of neat liquid, indicating that the

liquid phase cannot enter the nanopores. As the pressure is sufficiently high, the liquid overcomes

the capillary effect and the pressure induced infiltration takes place. Note that this phenomenon is

different from the well known capillary condensation, which happens in lyophilic channels. As the

liquid enters the nanopores, the system compressibility increases considerably, resulting in the

formation of the infiltration plateau of sorption isotherm. Under quasi-static condition, the

infiltration plateau should be perfectly flat if the pore size was uniform. In the system under

investigation, because the silica gel exhibits a pore size distribution, the infiltration starts with the

largest nanopores at a relatively low pressure and ends with the smallest nanopores at a relatively

high pressure. Since the silica gel sample is of a relatively regular nanopore structure [15], in the

following discussion classic Young's equation will be employed to relate the quasi-static

infiltration pressure, P_{in}, to the pore size, D:

$$P_{in} = 4 \cdot \Delta\gamma/D \tag{3.3}$$

where $\Delta\gamma$ is the excess solid-liquid interfacial tension, i.e., the difference between the solid-liquid

interfacial tension and the summation of solid and liquid surface tensions. Based on the profiles of

infiltration plateaus in Figure 3-2, the pore size distribution can be calculated via a Washburn-type

analysis [16], as shown in Figure 3-4, with the values of $\Delta\gamma$ being assumed constant and

determined by fitting the average pore size to the gas absorption measurement result, $\overline{D} = 7.8$ nm.

The value of P_{in} is taken from the sorption isotherm curve of the lowest loading rate, 1 mm/min.

Further lowering the loading rate would not cause any detectable changes in infiltration pressure;

that is, it can be regarded as quasistatic. Figure 3-5 shows the excess solid-liquid interface tension,

where P_{in} is defined as the infiltration pressure at $\overline{D}$. Note that Equation (3.3) is valid only when the

loading rate effect is negligible.
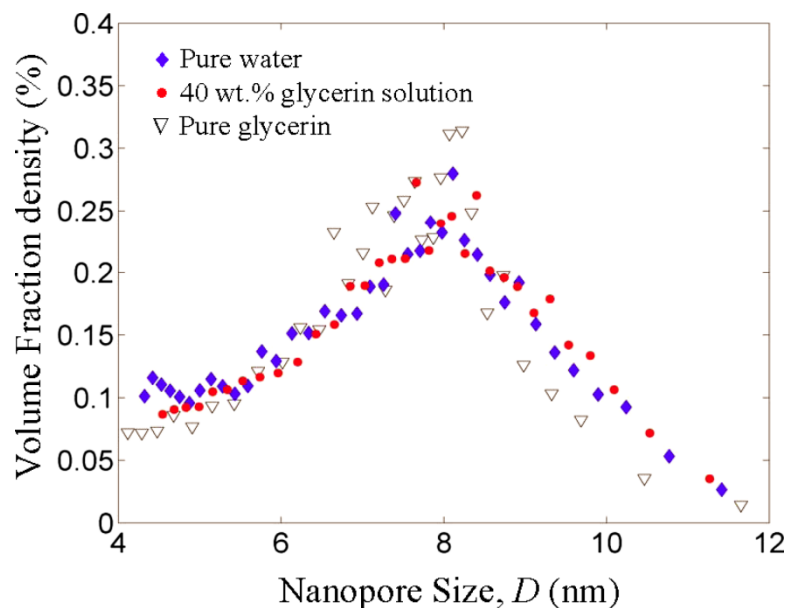
Figure 3-4 The pore size distribution curves
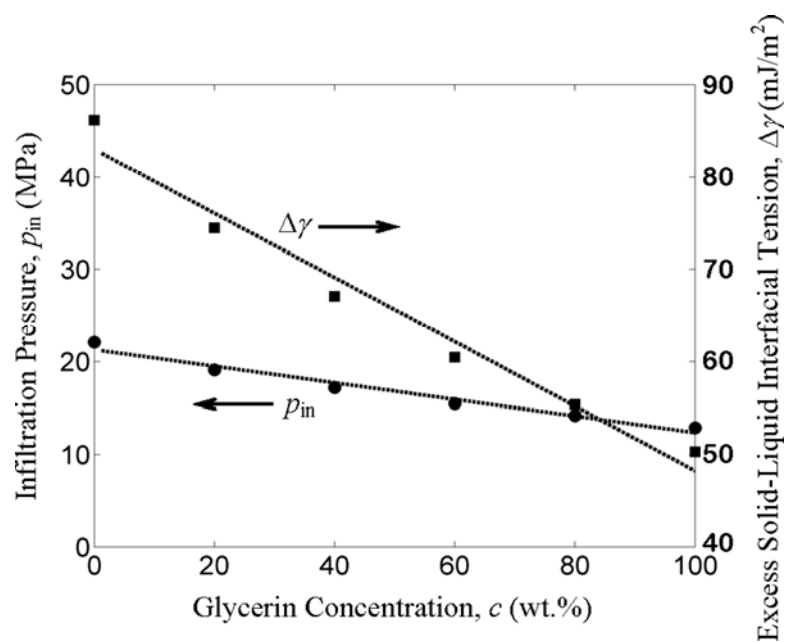
Figure 3-5 The infiltration pressure and the excess solid-liquid interfacial tension as functions of the glycerin concentration

The calculated pore size distributions of all the systems are similar to each other,

suggesting that in the nanopore size range under investigation, the classic capillary theory can describe the quasistatic liquid infiltration quite well. Moreover, $\Delta\gamma$ is insensitive to the pore size, D. However, at the lower end of pore size range, the pore size distribution data are relatively irregular, which may be attributed to that; as the pore size is comparable with the double layer thickness, the ordinary interface theory is no longer valid and the effective solid-liquid interfacial tension is affected by the confinement effect of pore walls. It may also be related to the influence of the gas phase entrapped in the nanopores, which, when under a high pressure, can dissolve in the confined liquid phase [17, 18]. The relationship between the glycerin concentration and P_{in} (or $\Delta\gamma$) is quite linear, suggesting that the effects of different components in the liquid phase can be analyzed by linear superposition.

As the loading rate increases, according to Figure 3-3, it is clear that the infiltration pressure of neat glycerin, P, becomes higher; that is,

$$P= P_{in}+\delta_p \tag{3.4}$$

where δp is the additional infiltration pressure related to the rate effect. The δp-P_{in} relation can be obtained by subtracting the quasistatic sorption isotherm curve from the high-loading-rate ones, which, by using Equation (3.3), can be converted to the δp-D relation, as shown in Figure 3-6. Note that there exists a sharp transition of δp at about 7.3 nm at all the loading rates. In the relatively small nanopores the additional infiltration pressure is higher by about 13 MPa than that in larger nanopores. This value does not vary much as the loading rate increases. The δp-D curve shifts as the loading rate varies. That is, when the loading rate becomes higher, the rate effect is more

pronounced, as it should be.
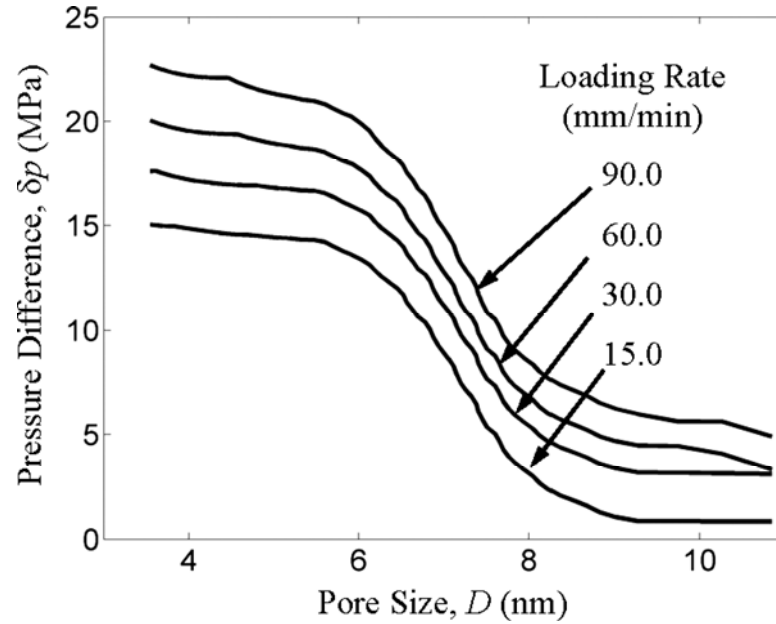
Figure 3-6 The increase in infiltration pressure caused by the loading rate effect

Based on the classic circular Poiseuille flow solution [19], as the first-order approximation,

we have

$$\delta_p = \frac{128\mu QL}{\pi D^4} \tag{3.5}$$

where μ is the effective liquid viscosity in nanopores, Q is the flow rate, and L is the effective

nanopore depth. During the infiltration experiment, since the piston speed, v, is constant, the

overall flow rate is fixed as vA_p, and the total infiltration time is $t_0 = V_p/vA_p$, with V_p=0.28

cm^3 being the nanopore volume. The time required to fill the nanopores of size D can then be

estimated as $t_D = ft_0$, where f is the volume density shown in Figure 3-4. Thus, the flow rate in a

nanopore can be assessed as

$$Q(D) = (fV_p)/(t_DN) = \pi vA_pD^2L/4fV_p \tag{3.6}$$

with $N = fV_p/(\pi D^2L/4)$ being the nmber of nanopores of size D. Consequently, Equation (3.5) can

be rewritten as

$$\mu = \alpha \delta_p D^2 f(D)/v \qquad (3.7)$$

where $\alpha = V_p/32A_pL^2$. If L is taken as one-half of the average silica particle size, 25 μm, the effective viscosity of glycerin in nanopores can be calculated based on the measurement result of δ_p, as shown in Figure 3-7.
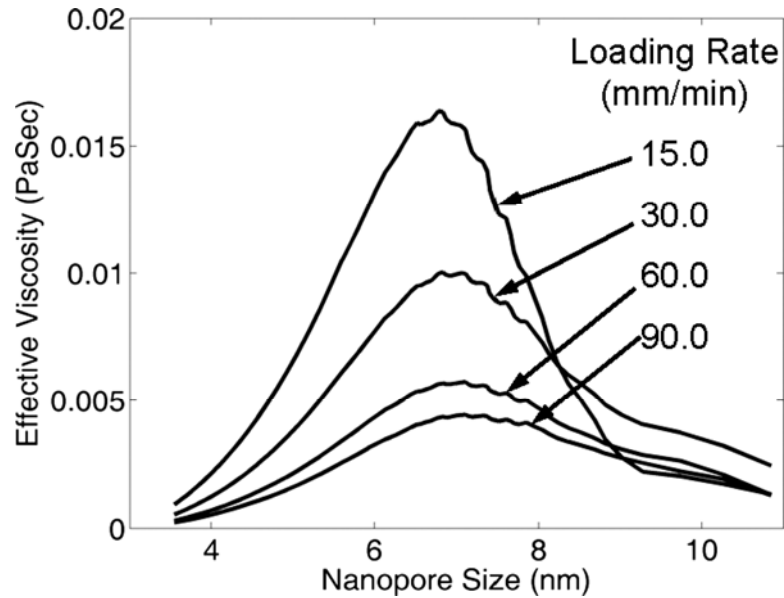
Figure 3-7 The effective liquid viscosity as a function of the loading rate and the nanopore size

The viscosity of bulk glycerin is 1.49 Pa·s [20]. According to Figure 3-7, the effective viscosity in nanopores is lower than this value by more than two orders of magnitude. Depending on the pore size and the loading rate, μ varies in the range of 10^{-3}–10^{-2} Pa·s. There exists a characteristic nanopore size, D_c, around 7 nm, at which the effective viscosity reaches the maximum value. This characteristic nanopore size slightly increases as the loading rate becomes higher. When the pore size is smaller than D_c, μ decreases with D. At a higher loading rate, the

effective μ is smaller. With a constant D, $d\mu/dv$ decreases with the increasing of v; i.e., when v is relatively large, the rate effect on the μ-D curve tends to saturate. When D is larger than D_c, $d\mu/dD$ is negative and the rate effect is less evident than in smaller nanopores.

The size and rate dependence of the effective viscosity should be associated with the confinement effect of nanopore walls. On the one hand, since the silica surface is lyophobic, it repels liquid molecules, and thus at the solid-liquid interface the density of liquid molecules should be lower. Moreover, the conformation of liquid molecules inside a nanopore is distinct from that of bulk liquid (including the number of nearest neighbors and average spacing), resulting in a different interaction rule. In particular, the fact that after the pressure is reduced to zero no obvious defiltration could be observed (Figure 3-2 indicates that the confined liquid molecules are retained at a local energy minimum. Such behavior is often associated with the lost of hydrogen bonds required for infiltration [18] and may cause a smaller viscosity force. Therefore, as the nanopore size is reduced and the solid-liquid interface layer becomes increasingly important, μ tends to decrease. On the other hand, as the nanopore diameter is comparable with the molecular size, across the pore cross section there are only a limited number of molecules, and the continuum theory is no longer valid. For instance, the velocity profile of a Poiseuille flow may not be fully developed. The liquid molecules may move along the nanopore wall. The two competing mechanisms determine the characteristic nanopore size, where the effective viscosity is maximized and the effects of internal friction and liquid density are balanced. When D is relatively small ($D<D_c$), the former mechanism is dominant; when $D>D_c$, the latter is more important. Note

that the effective viscosity decreases as the loading rate increases, indicating that the beneficial effect of using viscous liquids for energy absorption under dynamic loadings may be less pronounced than the prediction of continuum fluid mechanics, which is consistent with the experimental results reported by Li [7].

3.4 Conclusions

In summary, the current study provides experimental results that can be used for theoretical analysis of liquid infiltration in nanoenvironment. The testing data show that under a quasi-static loading, classic Young's equation can capture the infiltration pressure quite well. As liquid composition varies, superposition principle can be employed to analyze the solid-liquid interfacial tension. The effective liquid viscosity is not a material constant; it depends on the pore size and the loading rate, smaller than its bulk counterpart by two orders of magnitude. There exists a characteristic nanopore size at which the effective viscosity reaches the peak value.

Chapter 3, in part, is a reprint of the material as it appears in Journal of Applied Physics. Han, Aijie; Lu, Weiyi; Punyamurtula, Venkata; Chen, Xi; Surani, Falgun; Kim, Taewan; Qiao, Yu. Effective viscosity of glycerin in a nanoporous silica gel. 104, 124908. 1-4 (2008). The dissertation author was the primary investigator/author of this paper.

References

[1] Kalra, A; Garde, S; Hummer, G. Osmotic water transport through carbon nanotube membranes. Proceedings of the National Academy of Sciences of the United States of America. 2003. 100, 10175-10180.

[2] Eijkel, J; van den Berg, A. Nanofluidics: what is it and what can we expect from it. Microfluid Nanofluid. 2005. 1, 249-267.

[3] Hummer, G; Rasaiah, J; Noworyta, J. Water conduction through the hydrophobic channel of a carbon nanotube. Nature. 2001. 414, 188-190.

[4] Wan, R; Li, J; Lu, H; Fang, H. Controllable water channel gating of nanometer dimensions. Journal of the American Chemical Society. 2005. 127, 7166-7170.

[5] Sriraman, S; Kevrekidis, I; Hummer, G. Coarse nonlinear dynamics and metastability of filling-emptying transitions: water in carbon nanotubes. Physics Review Letter. 2005. 95, 130603.

[6] Liu, Y; Wang, Q; Zhang, L; Wu, T. Dynamics and density profile of water in nanotubes as one-dimensional fluid. Langmuir. 2005. 21, 12025-12030.

[7] Li, J. Damping of water infiltrated nanoporous glass. Journal of Alloys and Compounds. 2000. 310, 24-28.

[8] Borman, V; Belogorlov, A; Grekhov, A; Lisichkin, G; Tronin, V; Troyan, V. The percolation transition in filling a nanoporous body by a nonwetting liquid. Journal of Experimental and Theoretical Physics. 2005. 100, 385-397.

[9] Kong, X; Surani, F; Qiao, Y. Effects of addition of ethanol on the infiltration pressure of a mesoporous silica. Journal of Materials Research. 2005. 20, 1042-1045.

[10] Kong, X; Qiao, Y. Thermal effects on pressure-induced infiltration of a nanoporous system. Philosophical Magazine Letters. 2005. 85, 331-337.

[11] Kong, X; Qiao, Y. Improvement of recoverability of a nanoporous energy absorption system by using chemical admixture. Applied Physics Letters. 2005. 86, 151919.

[12] Surani, F; Kong, X; Panchal, D; Qiao, Y. Energy absorption of a nanoporous system

subjected to dynamic loadings. Applied Physics Letters. 2005. 87, 163111.

[13] Han, A; Qiao,Y. Effects of surface treatment of MCM-41 on motions of confined liquids. Journal of Physics D: Applied Physics. 2007. 40, 5743-5746.

[14] Kumar, M; Shankar, P. Experimental determination of the kinematic viscosity of glycerol-water mixtures. Proceedings of the Royal Society A. 1994. 444, 573-581.

[15] Terasaki, O; Ohsuna, T; Liu, Z; Kaneda, M; Kamiya, S; Carlsson, A; Tsubakiyama, T; Sakamoto, Y; Inagaki, S; Che, S; Tatsumi, T; Camblor, M; Ryoo, R; Zhao, D; Stucky, G; Shindo, D; Hiraga, K. Porous materials: Looking through the electron microscope. Studies in Surface Science and Catalysis. 2002. 141, 27-34.

[16] Giddings, J. Unified Separation Science. Wiley. 1991.

[17] Surani, F; Qiao, Y. Infiltration and defiltration of an electrolyte solution in nanopores. Journal of Applied Physics. 2006. 100, 034311.

[18] Qiao, Y; Cao, G; Chen, X. Effects of Gas Molecules on Nanofluidic Behaviors. Journal of the American Chemical Society. 2007. 129, 2355-2359.

[19] Fay, J. Introduction to Fluid Mechanics. MIT. 1994.

[20] White, F. Viscous Fluid Flow. McGraw-Hill. 2005.

Chapter 4 Effects of Electrolyte Concentration in Liquid Phase

4.1 Introduction

Developing high-performance smart materials has been a continuous effort since the discovery of the shape memory characteristic of titanium-nickel alloy [1]. Shape-memory alloys and polymers are activated via phase transformation [2]. As temperature changes, their atomic or molecular configurations can vary accordingly, accompanied by a significant volume increase or decrease. As a result, at the macroscopic scale the material shape can be thermally controlled. Conventional smart materials are solids. As the phase transformation is induced repeatedly and the local volume change occurs, fatigue damage and/or fracture may considerably limit the system reliability [3, 4]. Moreover, compared with the increasingly high functioned requirements, the energy density of these materials is still quite low [5]. To solve these problems, new mechanisms need to be investigated.
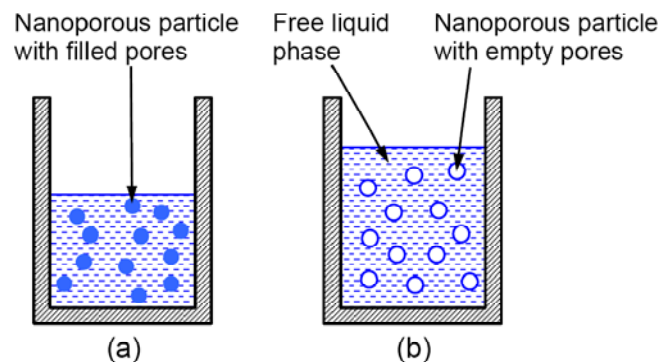
Figure 4-1 Schematic diagrams of the volume-memory liquid: (a) filled nanoporous particles and (b) empty nanoporous particles

The NMF liquid provided a promising direction [6]. The working mechanism is based on the well-known thermocapillary effect [7]; i.e. the solid/liquid surface tension and the solid-liquid interfacial tension are dependent on temperature. With appropriate surface treatment, a solid surface can be wettable to a liquid in a certain temperature range and non-wettable once temperature is beyond this range [8-10]. If this phenomenon is applied to a nanoporous material, it can lead to temperature-controlled liquid infiltration and defiltration. As depicted in Figure 4-1, such a NMF liquid is produced by dispersing nanoporous particles in a liquid phase. The particle size is typically 1-100 μm and the nanopore size is usually 1-10 nm. In Figure 4-1(a), the nanopore inner surfaces are wettable to the liquid, and, therefore, the nanoporous particles are soaked up. The total system volume can be assessed as

$$V_0 = V_l + V_s - V_p \tag{4.1}$$

with V_l, V_s, and V_p being the volumes of liquid, solid, and nanopores, respectively. When temperature changes, due to the difference in changing rates of surface tensions of liquid and solid phases, the interfacial tension, $\Delta\gamma$, may either increase or decrease [11], causing the variation in wettability. Figure 4-1(b) shows that when $\Delta\gamma$ becomes positive, i.e. when the nanopore surfaces are effectively nonwettable, the confined liquid can defiltrate out of the nanopores and thus the system volume expands. The expanded system volume can be estimated as

$$V_e = V_l + V_s \tag{4.2}$$

The deformability can be calculated as

$$\xi = V_p / (V_l + V_s) \tag{4.3}$$

which is typically 10-20% for zeolite Y based systems. Due to the small length scale involved in the liquid motion in nanoenvironment, the nature of liquid-solid interaction is quite different from that at large scale [12] and the infiltration/defiltration can be regarded as an effective phase transformation process [13], since the confined liquid phase and the free liquid phase are stable at different temperatures. The energy density of the smart liquid can be taken as

$$E=\Delta\gamma \cdot A \tag{4.4}$$

where $A \approx 10^2$-10^3 m^2/g is the specific surface area. Due to the large value of A, for solid-liquid systems with $\Delta\gamma$ around 10 mJ/m^2 [9, 10], E can be 1-10 J/g, which is two orders of magnitude higher than the value of 50 mJ/g reported for Ti-Ni alloys [14].

In the previous experiment on smart liquid [6], zeolite Y that had a well crystallized porous structure was employed as the nanoporous phase [15]. It was noticed that the liquid infiltration and defiltration behavior was dependent on the liquid composition. For instance, in a pure water based system, no volume memory behavior could be observed even when the temperature was adjusted in a broad range. The liquid phase should be modified by an electrolyte, after which the wetting-to-dewetting transition could be triggered by a relatively small temperature variation of only a few $^{\circ}$C. Since the liquid motion in nanopores is the key factor dominating the smart liquid properties, the influences of the electrolyte concentration and the temperature on the infiltration pressure will be investigated in the current study.

4.2 Experimental
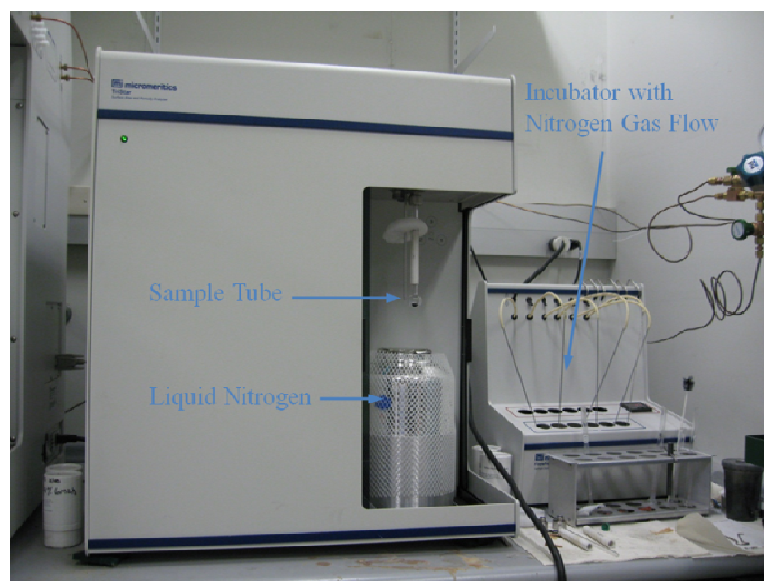
Figure 4-2 Micromeritics TriStar 3000 gas adsorption analyzer

The framework type for zeolite Y is FAU, which has 12-ring channel viewed along [111], with the nominal size of 0.74 nm×0.74 nm; its atomic structure was described in detail by Auerbach et al. [16]. The material was analyzed by using a Micromeritics TriStar 3000 gas adsorption analyzer (Figure 4-2). The effective nanopore size was determined as 0.6 nm, and the specific surface area was 710 m^2/g [6]. The specific nanopore volume was 220 mm^3/g. The initial silica/alumina ratio was 80. The material was heated at 120 ^{o}C for 3 hours so that it was dehydrated. It was then treated in saturated silicon tetrachloride vapor in nitrogen at 400 ^{o}C for 0.5 hours, followed by thorough rinsing with distilled water and calcination at 500 ^{o}C for 1 hours. The aluminum content was further decreased by hydrothermally treating the sample at 650 ^{o}C for 72 hours. Finally, the material was washed repeatedly by warm water and dried in vacuum.
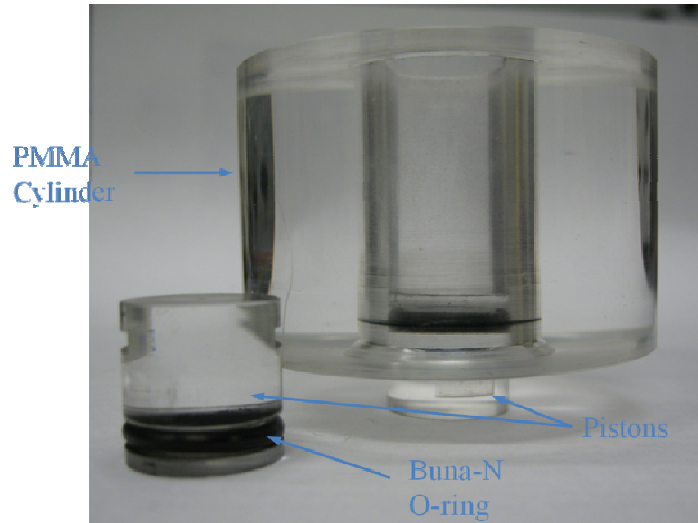
Figure 4-3 PMMA testing cell

About 1 g of the zeolite sample was suspended in 4 g of aqueous solution of potassium

chloride (KCl). The KCl concentration, [KCl], ranged from 18% to 24%. The suspension was

sealed in a poly(methyl methacrylate) cylinder (Figure 4-3). By intruding a stainless steel piston

into the cylinder, an external pressure, P, was applied on the liquid suspension. The piston motion

was controlled by the Instron machine in displacement-control mode at the rate of 1 mm/min. The

cross-sectional area of the piston, A_p, was 286 mm^2. When the applied load reached about 14.8 kN,

the piston was moved back at the same speed. The variation in specific volume of the zeolite

suspension, ΔV, was calculated as

$$\Delta V = d \cdot A_p / m \qquad (4.5)$$

with d being the piston displacement and m the mass of zeolite crystals. At a low pressure level, the

slope of sorption curve was relatively large. When the infiltration happened, the slope of sorption

curve became smaller. When the infiltration finished, the slope of the sorption curve became large

again. To investigate the thermally controlled liquid motion, the infiltration experiments were

performed with 18%, 20%, 22% and 24% of KCl solution at various temperatures in the range of 20

^{o}C to 80 ^{o}C. For each system, at least three samples were tested. It took about 0.9 min to complete a

loading process and about the same time for an unloading process. The temperature was maintained

by a water bath. Figures 4-4 and 4-5 show typical sorption curves at room temperature and at

elevated temperature, respectively. The infiltration plateau is shown as "AB", as will be discussed

below.
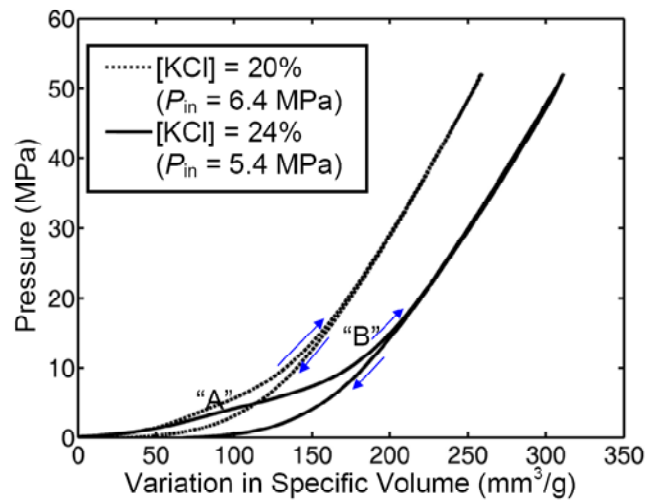
Figure 4-4 Typical sorption curves at 20 ^{o}C
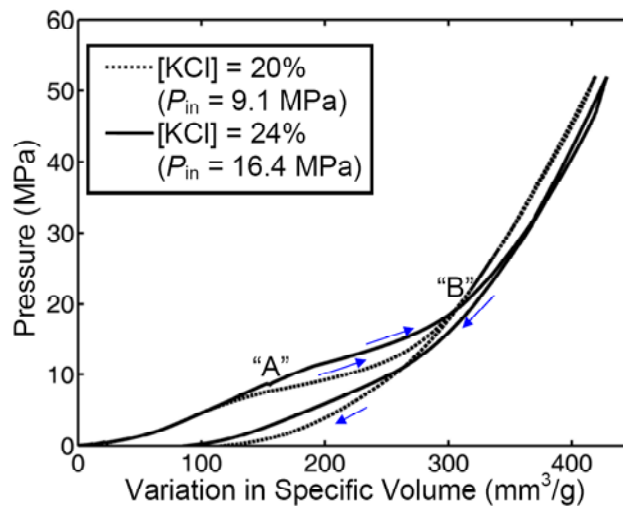
Figure 4-5 Typical sorption curves at 80 ^{o}C

4.3 Results and Discussion

Usually, if the silica/alumina ratio is higher than 18, a zeolite can be regarded as hydrophobic [17], which is in agreement with the phenomenon observed in gas adsorption analysis that an external pressure must be applied to force water vapor into the nanopores [18]. However, the wettability of nanopore inner surfaces is quite different in liquid water. When the zeolite sample is immersed in pure water, it can be soaked up immediately. Under this condition, because the nanopores are filled, the response of the zeolite suspension to external pressure is quite linear; that is, $K=P/\Delta V$ is nearly constant, which is dominated by the bulk modulus of water. Even after the material is treated by silicon tetrachloride and water vapors, spontaneous infiltration can still take place under ambient pressure. Clearly, it is much easier for water molecules to enter the nanopores in bulk phase than in vapor phase, probably because that in the confining nanoenvironment adjacent molecules can lead to the reduction in energy barrier between tetrahydral sites.

After the treatment, the effective degree of hydrophobicity of the zeolite has nearly been saturated. One way to further increase $\Delta\gamma$ is to modify the liquid composition to adjust the smart liquid properties. When [KCl] is relatively low, the zeolite sample is still wettable to the liquid phase. When [KCl] is lower than 20%, no infiltration plateau can be observed in the sorption isotherm curve. As shown in Figure 4-4, when [KCl] is 20%, pressure induced infiltration takes place. Shortly after the pressure increase, an infiltration plateau is formed, demonstrating the characteristics of a smart liquid. In the infiltration plateau, the system volume decreases rapidly

with a small pressure increment, indicating that the dominant deformation mechanism is no long

the linear compression of free liquid phase. That is, as the pressure rises, the barrier effect of the

nanopore surfaces can be overcome. Once the accessible nanopores are filled, the system

deformability significantly decreases, and the slope of sorption curve largely increases. The

infiltration pressure is close to that of 24% [KCl]. As [KCl] = 20%, the infiltration volume, i.e. the

width of the infiltration plateau, is only about 60 mm^3/g, 1/4 of the total nanopore volume,

suggesting that most of the nanopore surfaces have been wetted before the pressure is applied.   In

the following discussion, for self-comparison purpose, the infiltration plateau is defined as the part

of the sorption isotherm between the two points where the local slopes equal to 50% of that of the

high-pressure stage. The portion of the nanopores that are filled spontaneously is probably close to

the open ends, the details of which are still under investigation.

As [KCl] increases, the effective degree of hydrophobicity of the material keeps increasing.

When [KCl] = 24%, the infiltration plateau ("AB" in Figure 4-4) becomes much clearer. The

infiltration consists of two stages. At a low pressure level, the slope of sorption curve is relatively

large. At a higher pressure level, a smaller pressure increment is needed to reduce the system

volume, which may be associated with the promotion effect of confined liquid. The specific

infiltration volume is around 100 mm^3/g, still smaller than the nanopore volume measured by the

gas adsorption technique but much larger than that of the 20% KCl solution. Clearly, as [KCl] rises

the nanopore surfaces are more nonwettable and therefore little nanoporous space can be filled

under ambient pressure. Only when an external pressure is applied can the liquid infiltration take

place. The difference between the pore volumes in liquid infiltration and gas adsorption may be related to the van der Waals distance between the confined liquid molecules and the nanopore walls.

When temperature increases, the degree of hydrophobicity of zeolite becomes considerably higher, as shown in Figure 4-5. At 80 $^{\circ}$C, even in 20% KCl solution the infiltration profile is quite clear. The specific infiltration volume is about 100 mm^3/g, close to that of 24% KCl at 20 $^{\circ}$C, which represents the upper limit of nanoporous space. When the pressure is lower than 6 MPa, little evidence of infiltration can be observed. A regular infiltration plateau is formed in the pressure range from 6 MPa to 13 MPa. As the pressure further increases, the slope of sorption curve converges to that of free liquid phase. According to a Carnot cycle analysis, the net output energy is $\Delta\gamma\cdot A$ or $P_{in}V_{in}$, where P_{in} is the infiltration pressure and V_{in} is the infiltration volume. For the sake of simplicity, the infiltration pressure is taken as the pressure at the middle point of the infiltration plateau. If V_{in} is taken as 100 mm^3/g and P_{in} is taken as 9 MPa, the specific energy density can be calculated as 0.9 J /g, much larger than that of Ti–Ni alloys (50 mJ/g). When [KCl] is changed to 24%, these characteristics remain the same, except that the infiltration pressure range increases to 11-19 MPa by nearly 80%. If P_{in} is taken as 16.4 MPa, the specific energy density can be calculated as 1.6 J /g, much larger than that of 22% KCl at 80 $^{\circ}$C. It is clear that the degree of hydrophobicity is increased with temperature. Moreover, the infiltration and defiltration process is quite reversible, suitable to the applications of smart liquids.
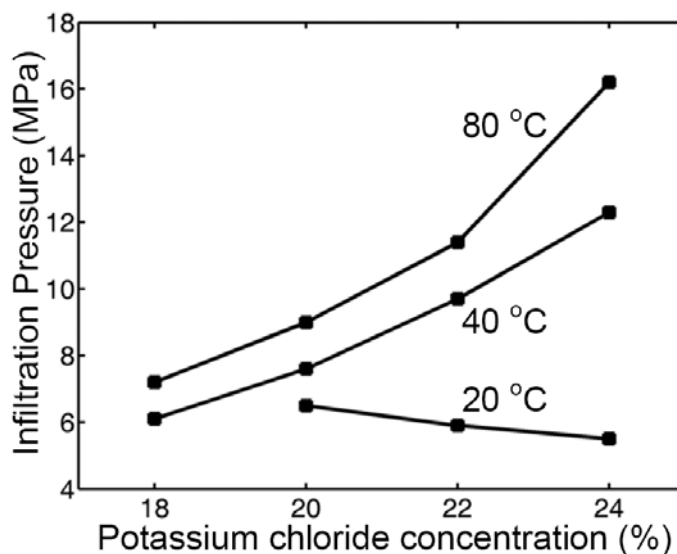
Figure 4-6 The infiltration pressure as a function of the potassium chloride concentration

Figure 4-6 shows the infiltration pressure as a function of the potassium chloride concentration and the temperature. In general, P_{in} increases with [KCl], as discussed above. At 20 °C, when the electrolyte concentration is relatively low, the pressure induced infiltration cannot occur fully. Since only the nanopores of high infiltration resistance are involved, the average value of P_{in} is higher than that at larger [KCl]. Note that this is caused by the limitation of the definition of infiltration pressure used in the current study, and may not reflect the variation in degree of hydrophobicity. At an elevated temperature, since the sorption curve reflects the behavior of all the accessible nanopores, the curves are more regular. According to the classic Laplace-Young equation [19], the effective solid-liquid interfacial tension can be estimated as

$$\Delta\gamma = P_{in} \cdot r/2 \tag{4.6}$$

with r=0.3 nm being the effective nanopore radius. At 40 °C, when [KCl] increases from 18% to 24%, $\Delta\gamma$ changes quite linearly from 0.9 mJ/m² to 1.8 mJ/m² by nearly 100%; that is, the effective

interfacial tension in nanopores is highly sensitive to the electrolyte concentration. The electrolyte

concentration effect is even more pronounced when the temperature is changed to 80 ^{o}C, where, as

[KCl] varies in the same range, $\Delta\gamma$ increases from 1.1 mJ/m^2 to 2.5 mJ/m^2 by about 130%. That is,

as the temperature increases, the hydrophobility increases more pronouncedly. At all the

temperatures, the reversibility of the NMF liquid is superior. The infiltration/defiltration curves can

be repeated more than ten times without detectable system degradation.

At a large solid surface, while the solid-liquid interfacial tension is dependent on the liquid

composition, the variation in $\Delta\gamma$ is typically only 20-30% between pure water and saturated

solutions [20]. In the nanopores, however, $\Delta\gamma$ changes by more than 100% when the potassium

chloride varies by only 6%. This may be attributed to the confinement effect of nanopore walls. At

a large surface, the solvated cations distribute in the Outer Helmholtz Plane (OHP), which is a few

Å from the solid phase [21, 22]. The interfacial tension is determined by the interaction among the

solid atoms, the solvated ions, as well as the water molecules. In a nanopore, especially when the

nanopore size is comparable with the OHP distance, the regular layered ion structure cannot be

formed. The solvated ions are surrounded by solid atoms from all the directions, and therefore the

effect caused by the increase in ion concentration, for instance the variation in interfacial tension

and the infiltration pressure, can be amplified. Since the nanoporous structure is stable in the

temperature range under investigation, similar electrolyte concentration effect can be observed at

all the testing temperatures. Such phenomenon can be used for adjusting the working temperature

range and/or the pre-loading range of smart liquids, depending of the functional requirements of

energy density, working condition, etc.

4.4 Concluding Remarks

The current study is focused on the experimental investigation on infiltration behaviors of electrolyte solutions in a zeolite Y. While the details of the liquid motion in nanopores are still under investigation, it is noticed that the effective solid-liquid interfacial tension in nanopores is highly sensitive to the electrolyte concentration, which may be related to the unique confinement environment in nanoporous material. As a result, with the addition of potassium chloride, both the infiltration pressure and the infiltration volume tend to increase. This finding provides a scientific basis for adjusting the ranges of temperature and pressure of nanoporous materials functionalized liquids.

Chapter 4, in part, is a reprint of the material as it appears in Smart Materials and Structures. Han, Aijie; Lu, Weiyi; Kim, Taewan; Punyamurtula, Venkata K.; Qiao, Yu. The dependence of infiltration pressure and volume in zeolite Y on potassium chloride concentration. 18, 024005.1-5 (2009). The dissertation author was the primary investigator/author of this paper.

References

[1]   Trochu, F; Brailovski, V; Galibois, A. Shape Memory Alloys: Fundamentals, Modeling and Industrial Applications . Warrendale. 1999.

[2]   Gandhi, M; Thompson, B. Smart Materials and Structures. Springer.1992.

[3]   Chopra, I. Review of state of art of smart structures and integrated systems. American Institute of Aeronautics and Astronautics Journal. 2002. 40, 2145-2187.

[4]   Kuna, M. Finite element analyses of cracks in piezoelectric structures: a survey. Archive of Applied Mechanics. 2006. 76, 725-745.

[5] Otsuka, K; Wayman, C. Shape Memory Materials. Cambridge: Cambridge University Press.1999.

[6]   Han, A; Qiao, Y. 2007. A volume memory liquid. Applied Physics Letters. 2007. 91, 173123.

[7]   Sefiane, K; Ward, C. Recent advances on thermocapillary flows and interfacial conditions during the evaporation of liquids. Advances in Colloid and Interface Science. 2007. 134-135, 201-223.

[8]   Qiao, Y; Cao, G; Chen, X. Effects of gas molecules on nanofluidic behaviors. Journal of the American Chemical Society. 2007. 129, 2355-2359.

[9]   Han, A; Qiao, Y. Thermal effects on infiltration of a solubility sensitive volume memory liquid. Philosophical Magazine Letters. 2007. 87, 25-31.

[10] Han, A; Qiao, Y. Infiltration pressure of a nanoporous liquid spring modified by an electrolyte. Journal of Materials Research. 2007. 22, 644-648.

[11] Erbil, H. Surface Chemistry of Solid and Liquid Interfaces. Wiley-Blackwell.2006.

[12] Qiao, Y; Punyamurtula, V; Han, A; Kong, X; Surani, F. Temperature dependence of working pressure of a nanoporous liquid spring. Applied Physics Letters. 2007. 89, 251905.

[13] Han, A; Kong, X; Qiao, Y. Pressure induced infiltration in nanopores. Journal of Applied Physics. 2006. 100, 014308.

[14] Wei, Z; Sandstrom, R; Miyazaki, S. Shape memory materials and hybrid composites for smart systems – Part I. Shape memory materials. Journal of Materials Science. 1998. 33, 3743-3762.

[15] Baerlocher, C; McCusker, L; Olson, D. Atlas of Zeolite Framework Types. Elsevier. 2007.

[16] Auerbach, S; Carrado, K; Dutta, P. Handbook of Zeolite Science and Technology. Marcel Dekker. 2003.

[17] Xu, R; Pang, W; Yu, J; Huo, Q; Chen, J. Chemistry of Zeolites and Related Porous Materials. John Wiley & Sons.2007.

[18] Yang, R. Gas Separation and Adsorption Processes. London. Imperial College Press. 1997.

[19] Shikhmurzaev, Y. Capillary Flows with Forming Interfaces. CRC Press.2007.

[20] Riviere, J; Myhra, S. Handbook of Surface and Interface Analysis. Marcel Dekker.1998.

[21] Schmickler, W. Interfacial Electrochemistry. Oxford University Press. 1996.

[22] Hartland, S. Surface and Interfacial Tension: Measurement, Theory, and Applications. Dekker. 2004.

Chapter 5 Effects of Anions in Liquid Phase

5.1 Introduction

Understanding behaviors of liquids in nanoporous materials has immense importance to a wide variety of scientific and engineering fields, including micro- and nano-transportation [1], phase transformation in heterogeneous liquids [2], surface processing in nanoenvironment [3], synthesis of nanostructured materials [4-6], advanced energy conversion and storage systems [7-9], etc. In the past, the study in this area was focused on spontaneous surface diffusion and reactions of guest molecules in host nanotubes or nanopores [10]. For instance, as a nanoporous material is immersed in a suspension of colloidal particles, it may selectively adsorb the species that are wettable to its inner surface, and hence the mixture is separated or purified [11]. As the guest molecules infiltrate into the nanopores, the system free energy must decrease; that is, the effective guest-host interfacial tension should be smaller than the summation of their surface tensions; otherwise, the guest infiltration is energetically unfavorable. Since the surface and interface tensions can be affected by temperature and electric potential, a few field-responsive systems have been developed so as to control the guest-host interactions under optimum conditions [12, 13].

Here, we investigate the new concept of NMF liquids: using mechanical method to control infiltration and defiltration has been an active area of research [14-16]. In such a system, the nanopore surface can be nonwettable to the liquid phase, so that under atmosphere pressure the

nanopores remain empty. As a quasi-static pressure is applied, the liquid phase can be compressed into the nanopores when the capillary effect is overcome. According to experimental investigation, under this condition multiple guest species, either wetting or nonwetting to the nanopore surface, tend to enter the host simultaneously, while the nanpore size must be sufficiently large and the structure of confined liquid may be highly nonuniform [17-19]. In some of the systems [20, 21], once the guest molecules enter the host, they are "locked" inside and do not come out even after the external pressure is released. In some other systems [22], the guest molecules can be separated from the host once the external pressure is relatively low, and these systems essentially become "liquid springs". Since the infiltration condition is dependent on temperature and electric potential, they can be employed for high-energy-density and large-displacement actuation [12, 13].

In addition to modifying nanopore size and surface properties, another important way to adjust system performance is to control the liquid composition. In the previous chapter, it has been shown that as an electrolyte was added into the liquid phase, the infiltration pressure can increase [23]. The conventional electrophysics theory often suggests that the solid-liquid interfacial tension is dominated by the cations [24, 25]. When an electrolyte dissolves in water, water molecules tend to form clusters surrounding cations, so that they are solvated. The anions can be unsolvated. As a solid is exposed to an electrolyte solution, immediately next to the solid surface there is a thin liquid layer of high density of solvated ions, which induce counter charges in the solid phase. The excess cations and the counter charges lead to a zeta potential normal to the solid-liquid interface. Under this condition, the influence of anions is secondary. These effects are captured by the classic

Good-Van Oss-Chaudhury (GVC) equation [26]:

$$\gamma_{12} = \gamma_1 + \gamma_2 - 2\left[\sqrt{\gamma_1^{LW}\gamma_2^{LW}} + \sqrt{\gamma_1^{+}\gamma_2^{-}} + \sqrt{\gamma_1^{-}\gamma_2^{+}}\right] \qquad (5.1)$$

where γ_{12} is the interfacial tension; the subscripts "1" and "2" refer to materials "1" and "2" across the interface, respectively; the superscripts of "LW", "+", and "-" refer to Lifshitz van der Waals, acidic, and basic components of surface tension, respectively. More detailed discussions of interfacial tension have been given elsewhere [27-29]. In this chapter, we experimentally investigate the anion effect on effective solid-liquid interfacial tension in the nanopores of a zeolite Y. The testing data show that in nanopores the effect of anions is comparable with that of cations, which may be attributed to the unique ion structure in the nanoenvironment.

5.2 Experimental

The testing system was produced by suspending 0.5 g of Zeolyst CBV-901 zeolite Y in 7.5 g of aqueous solution of sodium salts. The silica/alumina ratio of the Zeolite Y was 80. It was characterized in a gas adsorption analysis by using a Micromeritics ASAP-2020 system (Figure 2-5). The effective nanopore size was 0.74 nm; the specific nanopore surface area was 638 m^2/g; and the specific nanopore volume was 280 mm^3/g. The defect density at nanopore surface was modified through a 24 hours hydrothermal treatment. About 2 g of zeolite was placed in a quartz tube furnace, with the temperature maintained at 650 ^{o}C. Both ends of the tube were open to the air. At one end, warm water was pumped into the tube at a constant rate of 0.5 ml/sec. As water approached the heating zone, it rapidly evaporated and the steam passed through the zeolite to the

other end of the tube. During the treatment, the negatively charged hydroxyl groups were

deactivated, so that the nanopore surfaces were nearly perfect [30].
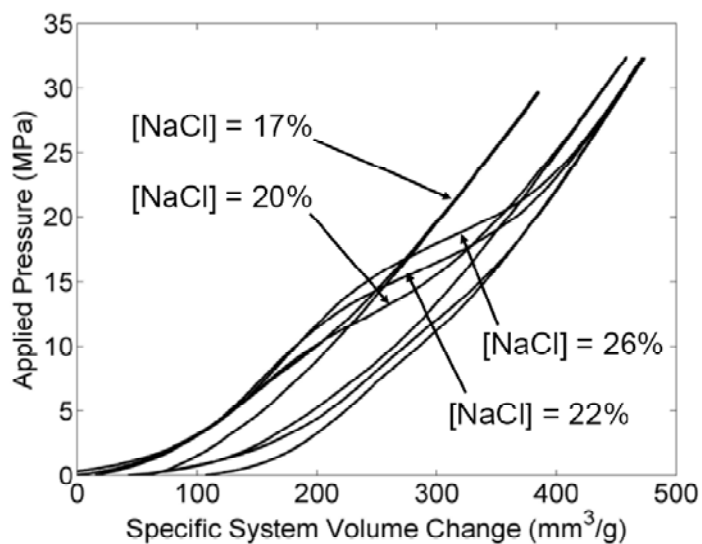
Figure 5-1 Sorption isotherm curves of sodium chloride based systems
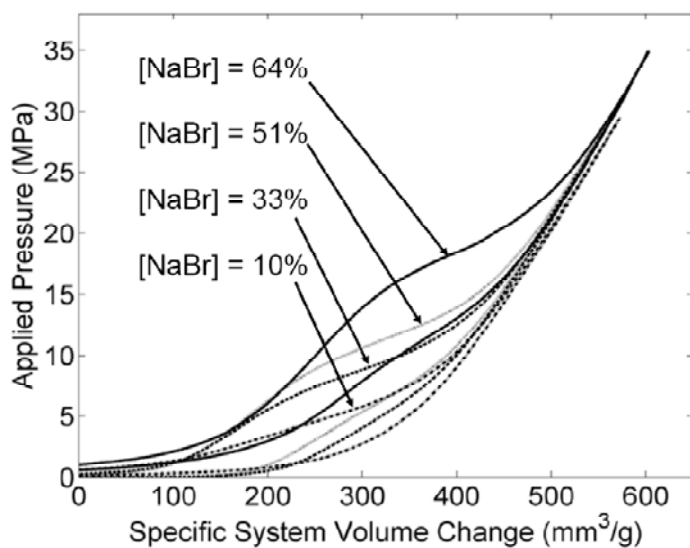
Figure 5-2 Sorption isotherm curves of sodium bromide modified systems

The zeolite suspension was placed in a steel cylinder. Its compressibility was analyzed by

driving a steel piston into the cylinder in a type 5582 Instron machine. The piston moved at a

constant rate of 1 mm/min. The gap between the piston and the cylinder was sealed by a reinforced

polyurethane o-ring. As the zeolite suspension was compressed, the inner pressure increased

continuously. After the infiltration was completed, the piston was moved out at the same speed. The

liquid phase was an aqueous solution of sodium chloride (NaCl) or a solution of sodium chloride

and sodium bromide (NaBr) mixture. In the NaCl solution, the concentration of NaCl, [NaCl],

varied in the range of 0 to 26%. In the NaCl and NaBr solution, [NaCl] was kept at 13% and the

NaBr concentration, [NaBr], varied in the range from 10% to 64%. Sodium bromide was employed

as the second electrolyte because its solubility is much higher than that of NaCl and the ion size of

bromine is larger than that of sodium ion. Typical infiltration curves are shown in Figure 5-1 and

5-2. Additional experiments were performed on systems based on saturated sodium chloride

solution ([NaCl] = 26%) at different temperatures, with the temperature being controlled by a water

bath. The measurement results of infiltration pressure are shown in Figure 5-3.
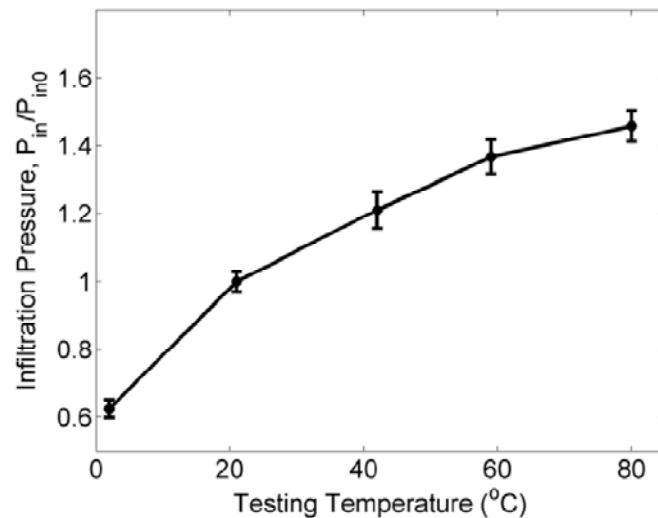
Figure 5-3 Thermal effect on infiltration pressure
of saturated sodium chloride solution based system

5.3 Results and Discussion

Since the silica/alumina ratio is high, the zeolite Y is hydrophobic in the gas absorption test (i.e. an external pressure must be applied to force the water vapor molecules into the nanopores). However, in liquid water the material is effectively hydrophilic. Once it is immersed in water, it would be soaked up spontaneously. Under this condition, the loading-unloading curve is quite linear, since the nanopores have been occupied and no further infiltration can take place. Similar behaviors are observed in all of the systems with [NaCl] lower than 17%. The difference in effective degrees of hydrophobicity of nanopore surfaces in water vapor and in liquid water may be related to the entrapped gas molecules [31] as well as the liquid-liquid interaction [32], the details of which are still under investigation.

When [NaCl] reaches 20%, as shown in Figure 5-1, a clear infiltration plateau shows up in the sorption isotherm curve in the pressure range of 7-17 MPa. If the external pressure is lower than this range, the system response is quite linear, indicating that the liquid phase does not enter the nanopores. When the pressure is above this range, the nanopores have been filled and, thus, the pressure-induced infiltration ceases. Within this pressure range, the liquid phase is forced into the nanoporous environment, leading to the rapid decrease in system volume. The total infiltration volume is around 200 mm^3/g, slightly smaller than the specific pore volume measured in the gas-absorption analysis, probably due to the van der Waals distance between the confined liquid molecules and the nanopore surface. Clearly, with the addition of NaCl, the zeolite Y becomes

nonwettable to the liquid phase, which is in agreement with the classic surface theory that the surface tension of an electrolyte solution increases with the electrolyte concentration [33]. That is, as more cations are solvated in the liquid phase, at a solid-liquid interface the surface ion density increases, and thus the solid-liquid interfacial tension tends to be higher. In the zeolite system under investigation, as [NaCl] is increased from 17% to 20%, the excess interfacial tension varies from negative to positive, causing the abrupt change in sorption isotherm profile. Note that, while the nanoporous structure of zeolite Y is highly regular, the slope of the infiltration plateau is significant, indicating that the nanopore walls offer a considerable resistance to liquid motion, which may be associated with the energy barrier among tetrahedral sites [34]. The details of the solid-liquid interaction in nanopores are still under investigation. By using the classic Laplace-Young equation [35], the effective excess interfacial tension can be assessed as $\Delta\gamma=P_{in}\cdot r/2=2.4$ mJ/m^2 when [NaCl] = 20%, where $r \sim 0.37$ nm is the nanopore radius and $P_{in} \sim 13$ MPa is the infiltration pressure. For self-comparison purpose, the value of P_{in} is taken as the pressure at the middle point of the infiltration plateau.

As the NaCl concentration increases, P_{in} increases rapidly. When [NaCl] reaches 26%, the infiltration pressure rises to about 20 MPa by nearly 100%, as shown by the solid line in Figure 5-4. Clearly, as more ions are added in the liquid phase, the repelling effect of the nanopore walls becomes more pronounced. The thermal effect on infiltration pressure shown in Figure 5-3 indicates that the effective excess interfacial tension is also quite sensitive to temperature, compatible with the previous experimental results on a thermally controllable smart liquid [36].
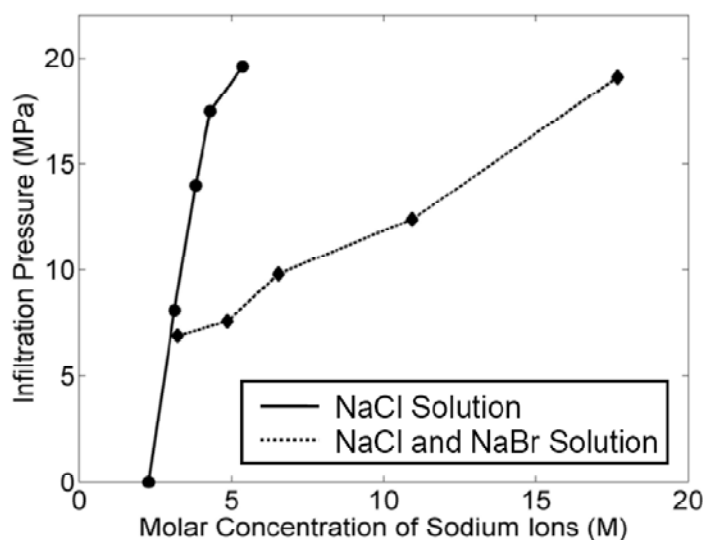
Figure 5-4 The infiltration pressure as a function of the molar concentration
of sodium cations

If in a nanopore $\Delta\gamma$ were dominated by the cations and the effect of anion were secondary,

when another sodium salt of a higher solubility, such as NaBr, is added, as the concentration of Na^+

becomes higher, the infiltration pressure should keep rising, until it saturates. However, the testing

data of NaCl/NaBr-mixture-based systems (Figure 5-2) show a contradictory trend. As [NaBr] =

10%, while the concentration of Na^+ is higher than that of the NaCl solution of [NaCl] = 20%, the

infiltration plateau is much lower. The value of P_{in} rises as [NaBr] becomes larger, but P_{in} exceeds 7

MPa only when [NaBr] = 33%, where the sodium cation concentration is nearly 50% higher than

that in the neat NaCl solution of [NaCl] = 20%. Eventually, when [NaBr] reaches 64%, the

infiltration pressure is about 18 MPa, still lower than that of the system based on saturated neat

NaCl solution (also see Figure 5-4). Note that the infiltration volumes of NaCl-based and

NaCl/NaBr-based systems are about the same, as it should be, since the nanoporous structure is

independent of the liquid composition.
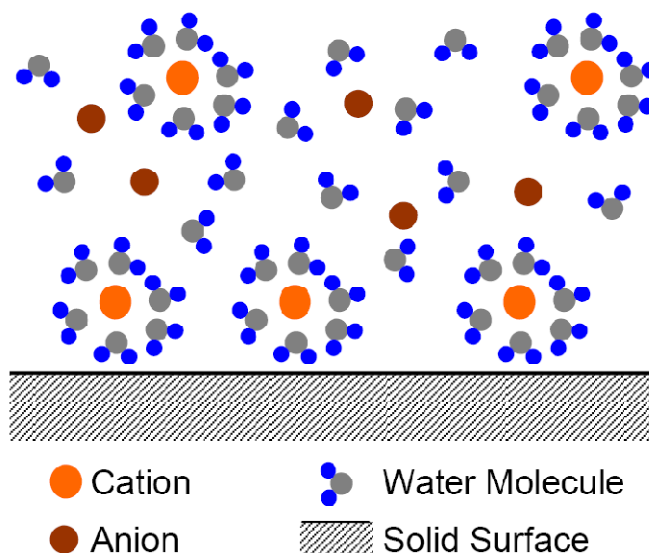
Figure 5-5 Schematics of liquid-solid interfaces at a large solid surface

The experimental observation must be attributed to the unique ion structure at the solid-liquid interfaces inside nanopores. As depicted in Figure 5-5, at a large solid-liquid interface the anion density in the double layer, which is often referred to as the Outer Helmholtz Plane (OHP), is quite low. Their concentration in the bulk phase has only a secondary effect on the interfacial potential and the interfacial tension. In a nanopore, especially when the nanopore size is comparable with the Debye length (Figure 5-6), the ordinary double-layer structure breaks down. Not only the water molecular cluster surrounding a solvated ion may not be fully developed, but also anions can enter the nanopore and be in direct contact with the solid surface [37]. Thus, the anion species can have a considerable influence on the effective solid-liquid interfacial tension. The van der Waals size of a bromine ion is 0.37 nm and that of a chlorine ion is 0.34 nm. In a nanopore

the solid-ion distance of bromine tends to be smaller, which may lead to a smaller effective

interfacial tension, the details of which need to be examined through first-principle simulations.
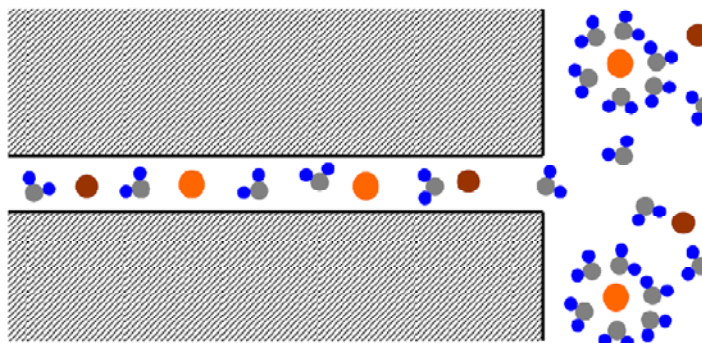
Figure 5-6 Schematics of liquid-solid interfaces in a nanopore

5.4 Conclusions

In summary, in a nanopore, anions have a pronounced influence on the effective

solid-liquid interfacial tension, which should be attributed to the unique ion structure in

nanoenvironment. The free energy of sodium bromide based system is much lower than that of

sodium chloride based system. At the saturation level of sodium salts, the effective interfacial

tension of the latter is higher, even though the solubility of the former is much larger.

Chapter 5, in full, is a reprint of the material as it appears in Physics Review E. Han, Aijie;

Lu, Weiyi; Kim, Taewan; Chen, Xi; Qiao, Yu. Influence of anions on liquid infiltration and

defiltration in a zeolite Y. 78, 031408.1-4 (2008). The dissertation author was the primary

investigator/author of this paper.

References

[1]   Meng, L; Li, Q; Shui, Z. Effects of size constraint on water filling process in nanotube. Journal of Chemical Physics. 2008. 128, 134703.

[2]   Han, A; Qiao, Y. A volume-memory liquid. Applied Physics Letters. 2007. 91, 173123.

[3]   Han, A; Qiao, Y. Effects of nanopore size on properties of modified inner surfaces. Langmuir 2007. 23, 11396-11398.

[4]   Sanchez, C; Boissiere, C; Grosso, D; Laberty, C; Nicole, L. Design, synthesis, and properties of inorganic and hybrid thin films having periodically organized nanoporosity. Chemistry of Materials. 2008. 20, 682-737.

[5]   Karami, D; Rohani, S. Progressive strategies for nanozeolite Y synthesis; a review. Reviews in Chemical Engineering. 2007, 23, 1-34.

[6]   Lee, J; Kim, J; Hyeon, T. Synthesis of new nanostructured carbon materials using silica nanostructured templates by Korean research groups. International Journal of Nanotechnology. 2006. 3, 253-279.

[7]   Van der Heyden, F; Stein, D; Dekker, C. Streaming currents in a single nanofluidic channel. Physical Review Letters. 2005. 95, 116104-116107.

[8]   Qiao, Y; Punyamurtula, V; Han. Mechanoelectricity of a nanoporous monel–electrolyte solution system. Power Sources. 2007. 164, 931-933.

[9]   Qiao, Y; Punyamurtula, V; Han, A. Thermally induced capacitive effect of a nanoporous monel. Applied Physics Letters. 2007. 91, 153102.

[10] Hoeltzel, A; Tallarek, U. Ionic conductance of nanopores in microscale analysis systems: Where microfluidics meets nanofluidics. Journal of Separation Science. 2007. 30, 1398-1419.

[11] Hillmyer, M. Block copolymers, advances in polymer science. 2005. 190, 137-181.

[12] Han, A; Qiao, Y. Thermal effects on infiltration of a solubility-sensitive volume-memory liquid. Philosophical Magazine Letters. 2007. 87, 25-31.

[13] Kong, X; Qiao, Y. An electrically controllable nanoporous smart system. Journal of Applied

Physics. 2006. 99, 064313.

[14] Han, A; Qiao, Y. Controlling infiltration pressure of a nanoporous silica gel via surface treatment. Chemistry Letters. 2007. 36, 882.

[15] Surani, F; Qiao, Y. Thermal recoverability of a polyelectrolyte-modified, nanoporous silica-based system. Journal of Materials Research. 2006. 21, 2389-2392.

[16] Surani, F; Qiao, Y. An energy-absorbing polyelectrolyte gel matrix composite material. Composites Part A: Applied Science and Manufacturing. 2006. 37, 1554-1556.

[17] Han, A; Qiao, Y. Pressure-induced infiltration of aqueous solutions of multiple promoters in a nanoporous silica. Journal of the American Chemical Society. 2006. 128, 10348-10349.

[18] Punyamurtula, V; Qiao, Y. Infiltration of pressurized promoter solutions in a mesoporous silica. Microporous Mesoporous Materials. 2007. 103, 35-39.

[19] Kong, X; Surani, F; Qiao, Y. Effects of addition of ethanol on the infiltration pressure of a mesoporous silica. Journal of Materials Research. 2005. 20, 1042-1045.

[20] Lefevre, B; Saugey, A; Barrat, J; Bocquet, L; Charlaix, E; Gobin, P; Vigier, G. Intrusion and extrusion of water in hydrophobic mesopores. Journal of Chemical Physics. 2004. 120, 4927-4938.

[21] Kong, X; Qiao, Y. Thermal effects on pressure-induced infiltration of a nanoporous system. Philosophical Magazine Letters. 2005. 85, 331-337.

[22] Eroshenko, V; Regis, R; Soulard, M; Patarin, J. Energetics: a new field of applications for hydrophobic zeolites. Journal of the American Chemical Society. 2001. 123, 8129-8130.

[23] Kong, X; Surani, F; Qiao, Y. Energy absorption of nanoporous silica particles in aqueous solutions of sodium chloride. Physica Scripta. 2006. 74, 531-534.

[24] Myers, D. Surface, interfaces, and colloids. Wiley-VCH. 1999.

[25] Shchukin, E; Pertsov, A; Amelina, E; Zelenev, A. Colloid and surface chemistry. Elsevier Science. 2001.

[26] Hartland, S. Surface and interface tension. CRC Press. 2004.

[27] Sugihara, G; Nagadome, S; Oh, S; Ko, J. A Review of Recent Studies on Aqueous Binary Mixed Surfactant Systems. Journal of Oleo Science. 2008. 57, 61-92.

[28] Hong, J; Shinar, T; Kang, M; Fedkiw, R. On boundary condition capturing for multiphase interfaces. Journal of Scientific Computing. 2007. 31, 99-125.

[29] Taylor, D; Thomas, R; Penfold, J. Polymer/surfactant interactions at the air/water interface. Advances in Colloid and Interface Science. 2007. 132, 69-110.

[30] van Bekkum, H; Flanigen, E; Jansen, J. Introduction to Zeolite Science and Practice. Elsevier Science. 1991.

[31] Qiao, Y; Cao, G; Chen, X. Effects of gas molecules on nanofluidic behaviors. Journal of the American Chemical Society. 2007. 129, 2355-2359.

[32] Hu, C; Li, D. Multiscale phenomena in microfluidics and nanofluidics. Chemical Engineering Science. 2007. 62, 3443-3454.

[33] Erbil, H. Surface chemistry of solid and liquid interfaces. Wiley-Blackwell. 2006.

[34] Liu, L; Qiao, Y; Chen, X. Pressure-driven water infiltration into carbon nanotube: the effect of applied charges. Applied Physics Letters. 2008. 92, 101927.

[35] Mott, R. Applied Fluid Mechanics. Prentice Hall. 2005.

[36] Han, A; Punyamurtula, V; Qiao, Y. Effects of cation size on infiltration and defiltration pressures of a MCM-41. Applied Physics Letters. 2008. 92, 153117.

[37] Tanimura, A; Kovalenko, A; Hirata, F. Structure of electrolyte solutions sorbed in carbon nanospaces, studied by the replica RISM theory. Langmuir. 2007. 23, 1507-1517.

Chapter 6 Field Responsive Liquid Motion in Nanopores – Indirect Control

6.1 Introduction

As a potential difference is generated across a solid-electrolyte interface, the system free energy can be changed considerably, which in turn affects the surface wettability [1]. Very often, electrowetting measurement is performed at the surface of a large, nonconductive flat layer, which separates a drop of electrolyte solution from an electrode, e.g. the experiment discussed in Chapter 6 [2]. The thickness of the nonconductive surface layer is typically in the range of a few μm to a fraction of mm [3, 4]. By applying a voltage between the electrode and the liquid, the contact angle can be adjusted in a wide range [5, 6]. According to the classic electrochemistry theory

$$\gamma = \gamma_1 - C\phi^2/2 \tag{6.1}$$

where γ is the interfacial tension, γ_1 is the reference wettability, C is the interfacial capacity, and ϕ is the applied potential difference. Note that no matter whether the applied voltage is positive or negative, the interfacial tension always decreases as the magnitude of ϕ increases. The effective interfacial tension, γ, can be taken as $\gamma_{sv}-\gamma_{sl}$, with γ_{sv} and γ_{sl} being the solid-vapor and solid-liquid interfacial energies, respectively.

For the past decade, many studies revealed important wetting and dewetting phenomena under external electric fields [7-10] and/or other forms of loadings [11-14]. These investigations were focused on the wettability of outer (non-confining) surfaces of nanostructures. In a confining

nanoenvironment, e.g. at inner surfaces of nanochannels, nanotubes, or nanopores, the electrowetting phenomena can be quite different. For instance, Prins et al. [15] developed a microtransport device by using a membrane containing straight microchannels. The inner surface of microchannel was coated by an insulation layer. As an external electric field was applied across the solid and the liquid phases, the wetting characteristics of channel walls could be controlled quite precisely, which caused a surface tension driven microfluidic motion. In this study, the microchannel size was at the level of 10^2 μm, and the variation of interfacial tension fitted well with the data of contact angle measurements. Other applications of electrowetting techniques include adjustment of liquid morphology [16], nanomaterials processing [17], etc.

One of the key parameters that dominate the performance of NMF liquids is the transport pressure of the confined liquid, P_{in}, i.e. the critical pressure that overcomes the capillary effect of nanopore walls. Previously, a few techniques have been developed to control P_{in}, by adjusting the nanoprous structure [18], surface treatment [19-21], and/or using chemical admixtures [22-25]. However, if the system works in a changing environment, the value of P_{in} may vary over time, which can cause unexpected loss in energy dissipation capacity. For instance, it was noticed that if temperature increases, P_{in} can be significantly decreased [26]. This softening effect must be taken into consideration for systems where stable performance is required in broad temperature ranges.

A possible environmental factor that can be employed to control P_{in} is the external electric field. However, the study on the electric field effect on solid-liquid interfacial tension in confining nanoenvironment is still at its early stage. As suggested by a number of researchers [27-30], many

physical and chemical concepts, including the definitions of density, viscosity, and phase diagram of liquids, need to be re-investigated at the nanometer scale, for which not only fundamental understanding but also basic testing data are still lacking. In a recent study [31] it was argued that in a nanopore the classic Laplace-Young equation is no longer valid. A new term that takes into account the column resistance of nanopore wall must be added to explain the testing data.

6.2 Experimental

The concept of contact angle breaks down in a nanopore, since there are only a limited number of liquid molecules in the cross section. Even if an effective contact angle could be defined, e.g. at a Gibbs surface, observing it in the interior of a nanoporous particle is prohibitively difficult. To analyze the solid-liquid interaction in confining nanoenvironment, a PII experimental setup was employed. The nanoporous phase was produced by using a nanoporous silica provided by Davisil. The as-received material was in particle form, having a large volume fraction of relatively regular nanopores [32]. The particle size was 20-50 μm. In order to increase the degree of hydrophobicity, the inner surfaces of nanopores were modified by silyl groups. About 2 g of the particles were first dehydrated at 100 ^{o}C for 36 hours, and then immediately immersed in 40 ml 1.5% dry toluene solution of chlorotrimethylsilane. The mixture was refluxed at 90 ^{o}C for 20 hours. During this process, the hydroxyl groups at nanopores surfaces were deactivated by chlorotrimethylsilane molecules, forming a hydrophobic monolayer [33], the details of which have been discussed elsewhere [34, 35]. The treated silica particles were filtered, washed with dry toluene and warm

water, and dried in vacuum at 50 $^{\circ}$C for 12 hours. The dried silica was placed in a steel mold and

compressed by a type 5582 Instron machine at 20 MPa, leading to the formation of nanoporous

silica disks. The mass of each disk was 16.5 mg and the thickness was around 100 μm, with the

cross-sectional area of 285 mm^2. Through a gas absorption analysis by using a Micromeritics

ASAP-2020 Analyzer (Figure 2-5), it was confirmed that the nanopores were open, as shown in

Figure 6-1. The average nanopore size was 7.4 nm and the specific nanopore volume was 560
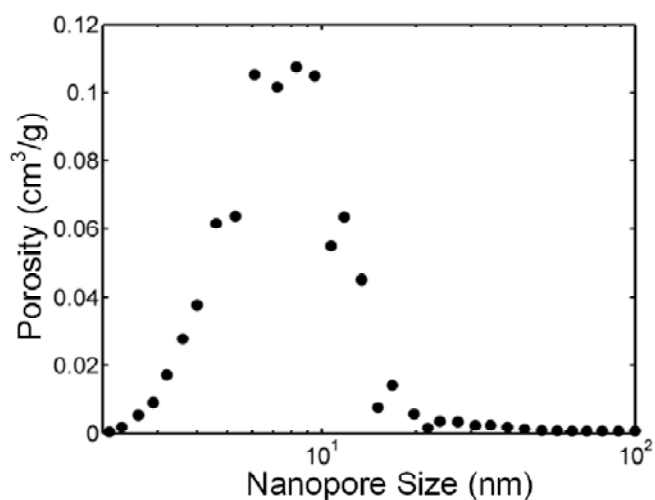
mm^3/g.
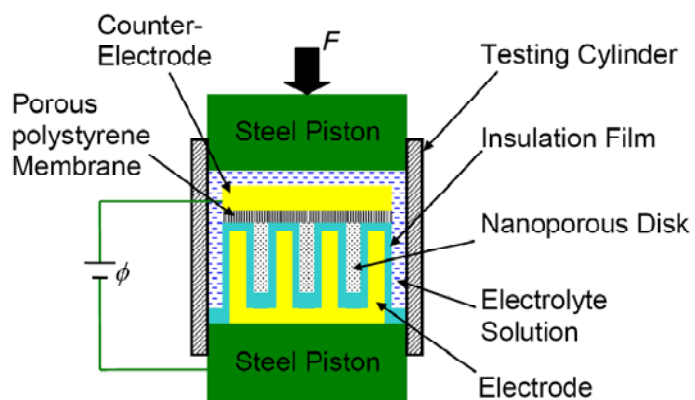
Figure 6-1 The nanopore volume distribution

Figure 6-2 Schematic of the experimental setup

By repeatedly folding an aluminum foil coated with Teflon thin film and inserting the silica

disks in between adjacent aluminum layers, a nanoporous layer stack was produced, as depicted in

Figure 6-2. The Teflon film thickness was 50 μm. This structure was condensed in the Instron

machine in a steel mold under 0.1 MPa, so that the layers were firmly compressed together. The

electrode was placed on a steel piston, with the edges of the aluminum layers in direct contact with

the steel. The rest area of the steel piston was insulated from the liquid phase by a thick layer of

epoxy adhesive. The steel piston, together with the layer stack, was placed at the bottom of a steel

cylinder, inside which 10 g of 15% potassium chloride (KCl) solution was sealed by another steel

piston from the top. The inner surface of the cylinder was insulated from the liquid phase by a

Teflon layer. By using a DC power source, an open-circuit voltage, ϕ, was applied between the

lower piston and a platinum counter-electrode, which was separated from the silica-aluminum layer

stack by a porous polystyrene membrane. The porous membrane thickness was 80 μm, and the pore

size was 1-2 μm. The value of ϕ was in the range of -380 V to +420 V. By using the Instron machine,

the upper piston was intruded into the cylinder at a constant rate of 0.5 mm/min. As the applied load,

F, exceeded 4.5 kN, the crosshead was moved back. The quasi-hydrostatic pressure in the liquid

phase was calculated as $P = F/A_p$, where $A_p = 286$ mm^2 is the cross-sectional area of the piston.

Figure 6-3 shows typical sorption isotherm curves. The measured ion transport pressure (P_{in}) is

given in Figure 6-4 as a function of the applied voltage. In order to minimize the influence of the

definitions of the starting and the ending points of infiltration, the value of P_{in} was taken as the

pressure at the middle point of the infiltration plateau, where the slope of sorption isotherm curve is

quite small. Compared with the pressure at the beginning of infiltration, the so-defined P_{in} better

reflects the energy exchange between the solid and liquid phases [31].
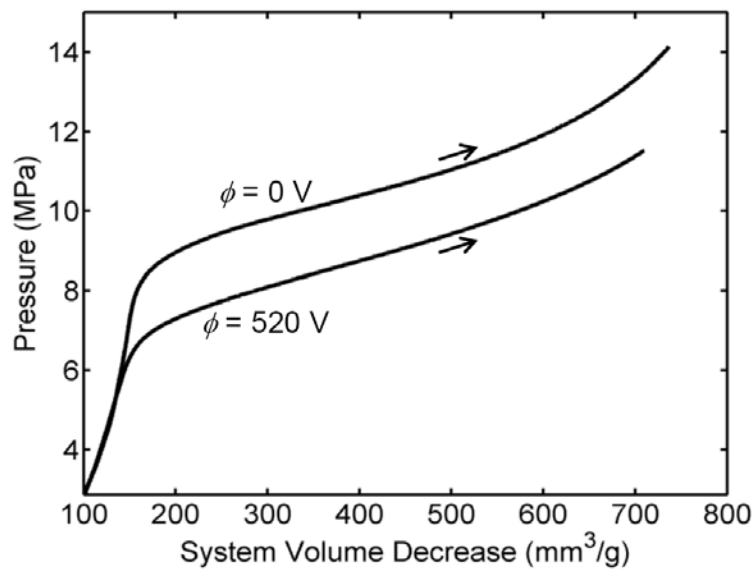
Figure 6-3 Typical sorption isotherm curves
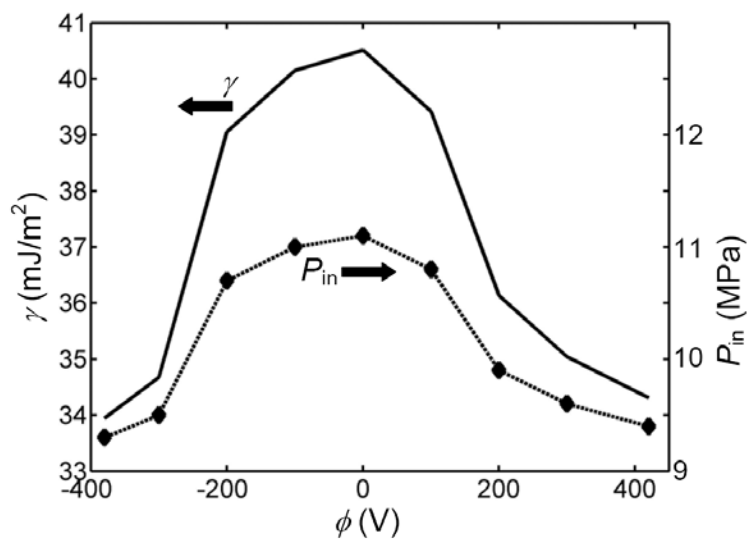
Figure 6-4 The ion transport pressure (P_{in}) and the effective interfacial tension (γ) as functions of the applied potential difference (ϕ)
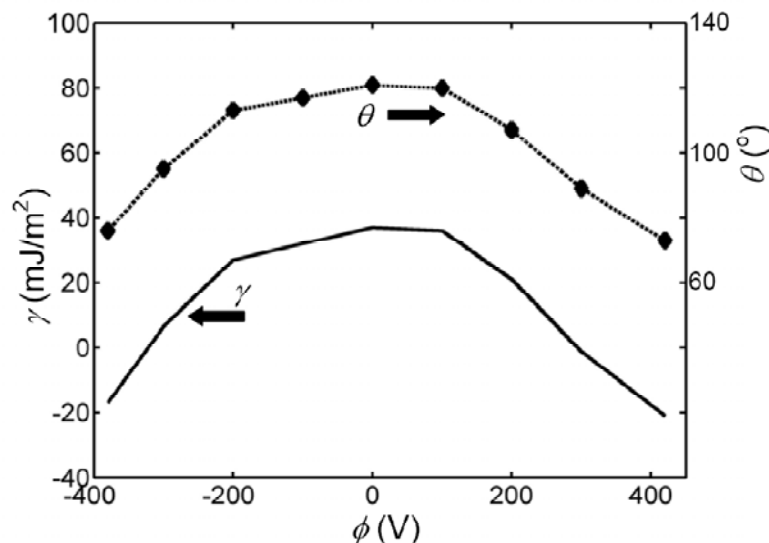
Figure 6-5 The contact angle (θ) and the interfacial tension (γ) as functions of the applied potential difference (ϕ) at a large flat surface

A reference test was performed on a large 60 μm thick glass slide, which was surface treated by chlorotrimethylsilane through a process similar with that of the nanoporous silica. A 50 μm thick Teflon layer was firmly compressed with the slide on top of a large aluminum electrode. A drop of 15% potassium chloride solution was placed on the Teflon layer, and its contact angle was measured in situ through a horizontal optical microscope. The external voltage applied between the aluminum electrode and the electrolyte solution was in the same range of -380 V to +420 V. The measurement results are shown in Figure 6-5.

6.3 Results and Discussion

At 0 V, the contact angle of the KCl solution at the large glass slide is 121°, indicating that the surface treated glass is highly hydrophobic. According to the classic Laplace-Young equation, the solid-liquid interfacial tension can be calculated as

$$\gamma_{sv}\text{-}\gamma_{sl}=\gamma_0\cdot cos\,\theta \;\; [36] \hspace{4cm} (6.2)$$

with γ_0=74 mJ/m^2 being the surface tension of the potassium chloride solution. From Figure 6-5, it can be seen that when the applied voltage is relatively low, the variation in interfacial tension is mild; as ϕ increases, γ decreases with an increasing rate. The direction of the electric field does not have a pronounced influence on the interfacial tension, and thus the ϕ-γ curve is quite symmetric. All these phenomena fit well with the prediction of the conventional electrochemistry theory [37]. As the voltage is applied between the electrode and the electrolyte solution, the glass slide and the Teflon layers serve as the insulation phase.

In the setup depicted in Figure 6-2, the interface of the liquid and solid phases is inside the nanopores. Due to the silyl treatment, the inner nanopore surfaces are hydrophobic. Therefore, under ambient pressure when the nanoporous silica samples are immersed in the potassium chloride solution, the liquid cannot enter the nanopores, due to the repelling effect of the nanopore walls. When an external pressure is applied by the upper piston, the mechanical work leads to the increase in system free energy. When the system free energy is sufficiently high, the capillary effect would be overcome, and the liquid infiltration starts. Associate with the liquid infiltration, the system volume rapidly decreases with a relatively small pressure increment, and thus a plateau region is formed in the sorption isotherm curve (Figure 6-3). The liquid transports in the nanopores until the entire nanoporous space is occupied. The width of the infiltration plateau is close to the specific nanopore volume. When the peak pressure is reached and the piston moves out, the pressure in the liquid phases keep decreasing. The unloading behavior of the system is quite

different from the loading path, indicating that the system is energy absorbing. The hysteresis may be related to the sliding of liquid molecules and ions along the solid surface [38, 39], the effects of entrapped gas/vapor nanophase [40, 41], etc., which is still under investigation and is not the focus of the current study. Note that while the pressure induced infiltration experimental procedure is somewhat similar with mercury porosimetry, the results should not be analyzed by a Washburn type method, since the interfacial tension is not a constant.

By compressing a unit volume of liquid phase into the nanopores, the work done by the external load is P_{in}. As the nanopore surfaces are in contact with the confined liquid, the system free energy increases by $\gamma \cdot A$, where $A \approx 2/r$ is the specific nanopore area per unit nanopore volume and r is the effective nanopore size. At equilibrium, $\gamma = P_{in} \cdot r/2$; i.e the system free energy change associated with the liquid infiltration is captured by the effective interfacial tension. According to the gas absorption measurement shown in Figure 6-1, the media nanopore size is 7.4 nm. The ion/liquid transport pressure corresponding to it, P_{in}, is assessed as the pressure at the intersection of the sorption isotherm curve and the median line between the low-pressure section of loading path and the unloading path. Thus, the values of γ can be calculated as a function of the applied voltage.

When $\phi = 0$, the values of γ of the nanoporous silica and the large glass slide are different. It can be caused by not only the confinement effect of the nanoporus environment, which will be discussed below, but also the different surface coverage due to the distinct surface reaction conditions as well as the differences in the electric loading mode and the thickness and configuration of silica layer. In the current study, we focus on the relative variation of γ associated

with the change in external electric field.

It is clear that the measured effective interfacial tension in nanopores decreases as the electric field is stronger. The change in γ is quite symmetric with respect to $\phi=0$. In the setup shown in Figure 6-2, the dielectric layer between the confined liquid phase and the electrode is the bilayer of Teflon film and silica nanopore wall. While near the Teflon-silica interface the silica layer thickness is quite small, the average silica layer thickness is comparable with that of the large glass slide used in the reference experiment. As the nanopores are filled by the electrolyte solution, the insulation effectiveness of the silica phase is reduced. Hence, if the interface properties in nanopores were similar with that at a large surface, the electrowetting effect on the nanoporous silica should be stronger than the result of the reference experiment.

However, the testing data show that the magnitude of variation of the interfacial tension of the nanoporous sample is much smaller than that in the reference test, even though the average silica layer thickness is thinner. When ϕ is increased from 0 to 420 V, the effective interfacial tension decreases by only about 15%, while in the reference test in the same voltage range the interfacial tension changes from positive to negative by more than 140%, nearly 10 times larger. The effective interfacial tension can be regarded as the increase in system free energy per unit area of nanopore inner surface, after the liquid infiltrates into the nanopore. Its dependence on the applied voltage may be attributed to the confinement effect of nanopore walls on the ion transport behavior (Figure 6-6). At a large surface, outside the Outer Helmholtz Plane (OHP) there exists a bulk liquid phase, which can be regarded as an infinitely large ion reservoir. When the interface

potential becomes different, the electrode-liquid electrostatic energy and the double layer at the insulator-liquid interface would change, both of which lead to the variation in surface ion density; that is, ions tend to move across the OHP into or out of the bulk phase. In the bulk phase, ions are in thermal disarrays. The effective surface ion density can be assessed as the total number of confined ions normalized by the nanopore surface area. In a nanopore, the surface to volume ratio is ultrahigh. Due to the lack of a bulk liquid phase in the interior of a nanopore, when the surface potential varies, the motion of ions can quickly make the confined liquid monopolar, creating a reverse double-layer-like structure that prevents the ion structure in the interface layer from being fully developed; that is, the interface capacity tends to be lower compared with that of a large surface. Therefore, while the tendency of interfacial tension variation is the same, its magnitude is reduced.
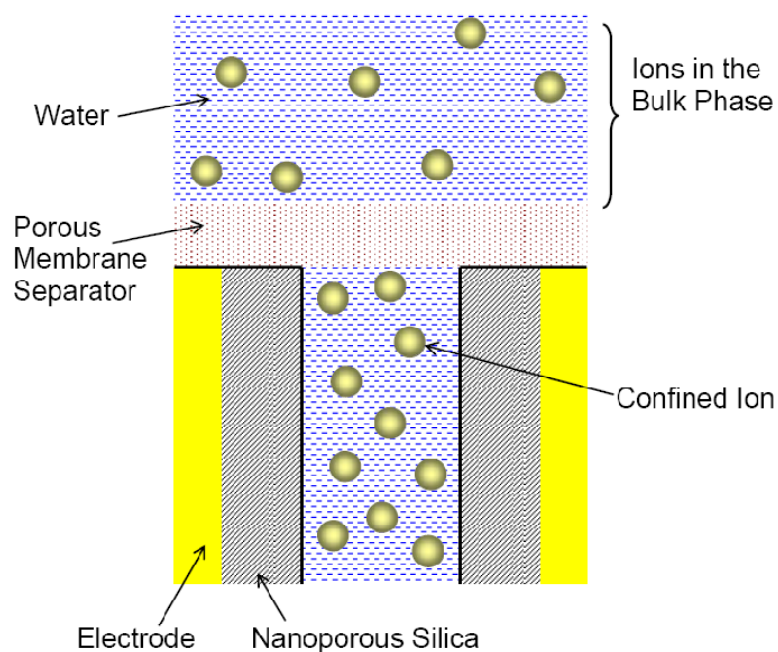

Figure 6-6 Schematic of confined ions in a nanopore

Another interesting observation is that the γ-ϕ relation of the nanoporous system cannot be described by the classic equation of $\gamma=\gamma_1-C\phi^2/2$. Around 200 V, the variation rate of the interfacial tension greatly decreases. In the negative voltage range, there is a similar step. Above the critical voltage, $d\gamma/d\phi$ keeps decreasing as ϕ rises. When ϕ is close to 400 V, the slope of the γ-ϕ curve is smaller than that at the low-voltage section by about an order of magnitude. The saturation of the electric field effect can also be caused by the small volume to surface area ratio of the confined liquid. As the excess ion concentration in the interior is balanced, further increase in potential difference would not cause much variation in the effective ion density in the interface layer, unless ions diffuse away or into the nanopores along the axial direction. In a previous experiment [42], it was observed that ion exchange between the confined liquid phase and the bulk liquid phase outside the nanoporous particles can be quite slow. The suppression of the ion density change can result in reductions in variations in electrode-liquid electrostatic effect and in silica-liquid interaction, which in turn stabilize the system free energy, so that the effective interfacial tension is less sensitive to the external electric field.

Note that the above analysis based on the assumption that the lack of bulk liquid phase in nanopores suppresses the electrowetting effect is not directly supported by the experimental evidence. More comprehensive experiments and computer simulations must be performed to eventually validate it, which will be the focus of our future work.

6.4 Conclusions

The effective solid-liquid interfacial tension in a nanoporous silica is measured as a function of the applied potential difference. Similar to the prediction of classic electrochemistry theory, the interfacial tension decreases with the increase in potential difference, and the effect of electric field direction is negligible. However, compared with a large solid surface, in the nanopores the electrowetting effect is quite weak, and it tends to be saturated when the voltage is relatively low. One possible cause of these phenomena is the large surface-volume ratio of the confined liquid phase, where the interior cannot be regarded as a neutral, infinitely large ion reservoir. This assumption needs to be verified through further experimental study and computer simulation.

Chapter 6, in full, is a reprint of the material as it appears in Langmuir. Lu, Weiyi; Kim, Taewan; Han, Aijie; Chen, Xi; Qiao, Yu. Electrowetting effect in a nanoporous silica. 25, 9463-9466 (2009). The dissertation author was the primary investigator/author of this paper.

References

[1] Cho, S; Moon, H. Electrowetting on dielectric (EWOD): new tool for bio/micro fluids handling. BioChip Journal. 2008. 2, 79-96.

[2] The, S; Lin, R; Hung, L; Lee, A. Droplet microfuidics. Lab on a Chip. 2008. 8, 198-220.

[3] Haeberle, S; Zengerle, R. Microfluidic platforms for lab-on-a-chip applications. Lab on a Chip. 2007. 7, 1094-1110.

[4] Gras, S; Mahmud, T; Rosengarten, G; Mitchell, A; Kalantar-Zadeh, K. Intelligent control of surface hydrophobicity. ChemPhysChem. 2007. 8, 2036-2050.

[5] Mugele, F; Baret, J. Electrowetting: from basics to applications. Journal of Physics: Condensed Matter. 2005. 17, R705-R774.

[6] Darhuber, A; Troian, S. Principles of microfluidic actuation by modulation of surface stresses. Annual Review of Fluid Mechanics. 2005. 37, 425-455.

[7] Verplanck, N; Galopin, E; Camart, J; Thomy, V; Coffinier, Y; Boukherroub, R. Reversible electrowetting on superhydrophobic silicon nanowires. Nano Letters. 2007. 7, 813-817.

[8] Brunet, P; Lapierre, F; Thomy, V; Coffinier, Y; Boukherroub, R. Extreme resistance of superhydrophobic surfaces to impalement: reversible electrowetting related to the impacting/bouncing drop test. Langmuir. 2008. 24, 11203-11208.

[9] Bahadur, V; Garimella, S. Preventing the Cassie−Wenzel transition using surfaces with noncommunicating roughness elements. Langmuir. 2009. 25, 4815-4820.

[10] Staicu, G; Manukyan, G; Mugele, F. Microscopic structure of electrowetting-driven transitions on superhydrophobic surfaces available. arXiv: 0801.2683v1 [physics.flu-dyn]. 2008.

[11] Bartolo, D; Bouamrirene, F; Verneuil, E; Buguin, A; Silberzan, P; Moulinet, S. Bouncing or sticky droplets: Impalement transitions on superhydrophobic micropatterned surfaces. Europhysics Letters. 2006. 74, 299–305.

[12] Reyssat, M; Pepin, A; Marty, F; Chen, Y; Quere, D. Bouncing transitions on microtextured materials. Europhysics Letters. 2006. 74, 306–312.

[13] Lafuma, A; Quéré, D. Superhydrophobic states. Nature Material. 2003. 2,457-460.

[14] Bormashenko, E; Pogreb, R; Whyman, G; Erlich, M., Vibration-induced Cassie-Wenzel wetting transition on rough surfaces. Applied Physics Letters. 2007. 90, 201917.

[15] Prins, M; Welters, W; Weekamp, J. Fluid control in multichannel structures by electrocapillary pressure. Science. 2001. 291, 277-280.

[16] Chang, C; Yang, R. Electrokinetic mixing in microfluidic systems. Microfluid. Nanofluid. 2007. 3, 501-525.

[17] Kim, D; Lu, W. Self-organized nanostructures in multi-phase epilayers. Nanotechnology. 2004. 15, 667-674.

[18] Punyamurtula, V; Qiao, Y. A selectively-energy-absorbing nanoporous system. Materials Letters. 2008. 62, 2928-2930.

[19] Kim, T; Han, A; Qiao, Y. Effects of surface-group length on liquid defiltration in a MCM-41. Journal of Applied Physics. 2008. 104, 034304.

[20] Han, A; Qiao, Y. Effects of gas-solid reaction on liquid defiltration in a MCM-41. Chemical Engineering Journal. 2008. 141, 379-382.

[21] Han, A; Punyamurtula, V; Qiao, Y. Effects of decomposition treatment temperature on infiltration pressure of a surface modified nanoporous silica gel. Chemical Engineering Journal. 2008. 139, 426-429.

[22] Kim, T; Lu, W; Han, A; Punyamurtula, V; Chen, X; Qiao, Y. Effects of anion concentration on ion-transport pressure in nanopores. Applied Physics Letters. 2009. 94, 013105.

[23] Han, A; Lu, W; Kim, T; Punyamurtula, V; Qiao Y. The dependence of infiltration pressure and volume in zeolite Y on potassium chloride concentration. Smart Materials and Structures. 2009. 18, 024005.

[24] Han, A; Punyamurtula, V; Qiao, Y. Effects of cation size on infiltration and defiltration pressures of a MCM-41. Applied Physics Letters. 2008. 92, 153117.

[25] Han, A; Qiao, Y. Infiltration pressure of a nanoporous liquid spring modified by an electrolyte. Journal of Materials Research. 2007. 22, 644-648.

[26] Han, A; Qiao, Y. Thermal effects on infiltration of a solubility-sensitive volume-memory liquid. Philosophical Magazine Letters. 2007. 87, 25-31.

[27] Mattia, D; Gogotsi, Y. Review: static and dynamic behavior of liquids inside carbon nanotubes. Microfluid. Nanofluid. 2008. 5, 289-305.

[28] Hoeltzel, A; Tallarek, U. Ionic conductance of nanopores in microscale analysis systems: where microfludics meets nanofluidics. Journal of Separation Science. 2007. 30, 1398-1419.

[29] Han, A; Lu, W; Punyamurtula, V; Chen, X; Surani, F; Kim, T; Qiao, Y. Effective viscosity of glycerin in a nanoporous silica gel. Journal of Applied Physics.2008. 104, 124908.

[30] Han, A; Lu, W; Kim, T; Chen, X; Qiao, Y. Influence of anions on liquid infiltration and defiltration in a zeolite Y. Physical Review E. 2008. 78, 031408.

[31] Qiao, Y; Liu, L; Chen, X. Pressurized liquid in nanopores: A modified Laplace-Young equation. Nano Letters. 2009. 9, 984-988.

[32] Terasaki, O; Ohsuna, T; Liu, Z; Kaneda, M; Kamiya, S; Carlsson, A; Tsubakiyama, T; Sakamoto, Y; Inagaki, S; Tatsumi, T; Camblor, M; Ryoo, R; Zhao, D; Stucky, G; Shindo, D; Hiraga, K. Porous materials: looking through the electron microscope. Studies in Surface Science and Catalysis. 2002. 141, 27-34.

[33] Han, A; Qiao, Y. Controlling infiltration pressure of a nanoporous silica gel via surface treatment. Chemistry Letters. 2007. 36, 882-883.

[34] Han, A; Qiao, Y. Effects of nanopore size on properties of modified inner surfaces. Langmuir. 2007. 23, 11396-11398.

[35] Lim, M; Stein, A. Comparative studies of grafting and direct syntheses of inorganic−organic hybrid mesoporous materials. Chemistry of Materials. 1999. 11, 3285-3295.

[36] Fay, J. Introduction to Fluid Mechanics. MIT Press. 1994.

[37] Bockris, J; Khan, S. Surface electrochemistry: a molecular level approach. Plenum Press. New York. 1993.

[38] Chen, X; Cao, G; Han, A; Punyamurtula, V; Liu, L; Culligan, P; Kim, T; Qiao, Y. Nanoscale fluid transport: size and rate effects. Nano Letters. 2008. 8, 2988-2992.

[39] Cao, G; Qiao, Y; Zhou, Q; Chen, X. Infiltration behavior of water in a carbon nanotube under external pressure. Philosophical Magazine Letters. 2008. 88, 371-378.

[40] Qiao, Y; Cao, G; Chen, X. Effects of gas molecules on nanofluidic behaviors. Journal of the American Chemical Society. 2007. 129, 2355-2359.

[41] Han, A; Kong, X; Qiao, Y. Pressure induced infiltration in nanopores. Journal of Applied Physics. 2006. 100, 014308.

[42] Qiao, Y; Punyamurtula, V; Han, A; Lim, H. Thermal-to-electric energy conversion of a nanoporous carbon. Journal of Power Sources. 2008. 183, 403-405.

Chapter 7 Field Responsive Liquid Motion in Nanopores - Direct Control

7.1 Introduction

In a nanochannel, especially when the characteristic length scale is comparable with the Debye length, the solvated structures of ions would be influenced by the channel wall [1, 2]. The distribution of water molecules can be highly distorted along the axial direction, which would be energetically unfavorable in a bulk phase [3-7]. As most of ions are exposed to the nanochannel wall, the amount of ions in the interior is much smaller than that at a large solid surface. As a result, the mass and energy exchange between the interface zone and the bulk phase is significantly suppressed [8-10]. The equilibrium conditions at the Gouy-Chapman and Stern layers and their dependence on environmental factors can be affected by the far field [11-14]. The time constants of surface adsorption/desorption may increase [15, 16]. Moreover, anions may directly interact the solid atoms, causing a "squeezing" effect [17].

As ions are adsorbed by a solid surface, countercharges can be induced in the solid phase, leading to the formation of electrostatics [18]. This phenomenon has been observed in nanoporous electrodes under various conditions [19-22]. If a low voltage is applied, additional oppositely charged ions would be adsorbed; that is, the equilibrium surface ion density is dependent on the external electric field [23]. While this concept has been studied intensively by a number of research groups [24], the influence of applied electric field on ion transport behaviors is still relatively

un-investigated. Experimental results that can validate and/or provide system parameters for the simulations are scarce.

One difficulty in the experimental study on field responsiveness of ion transport in nanochannels is the lack of direct measurement method of system free energy. As ions transport in a nanochannel, at the steady state the system free energy would be different from that of the initial state. In a test where spontaneous ion diffusion is dominant, such information would be lost. The pressure-induced infiltration (PII) technique provides a promising way to solve this problem [25-27]. In a PII test, the nanochannel surfaces must be hydrophobic, so that under ambient condition the nanochannels are empty. The liquid phase enters the nanochannels only when a sufficiently high external pressure, P, is applied.

7.2 Experimental

We investigated a zeolite Y (ZY) obtained from the Zeolyst. The as-received material was in powder form, with the particle size of about 10 μm and the silica-to-alumina ratio of 80. According to a gas absorption analysis by using a Micrometrics ASAP-2020 Analyzer (Figure 2-5), the nanopore size was 0.7 nm; the specific surface area was 710 m^2/g; and the porosity was 220 mm^3/g. The x-ray diffraction analysis result showed that the material was well crystallized. About 2 g of the ZY sample was dried in vacuum at 120 ^{o}C for 6 hours and then sealed in a vertical furnace with a cylindrical quartz reactor. At 400 ^{o}C, a slow nitrogen flow carrying silicon tetrachloride ($SiCl_4$) vapor was maintained across the reactor for 2 hours. The ZY sample was filtered, repeatedly

rinsed by acetone, methanol, and warm water, until the pH value reached 7. The material was

combusted in air at 600 ^{o}C for 1.5 hours, and finally rinsed in warm water and dried in vacuum at
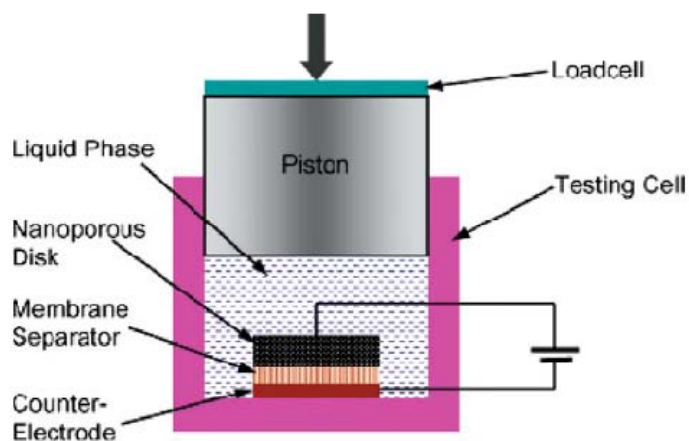
120 ^{o}C for 12 hours.

Figure 7-1 Schematic of the charged experimental setup

The treated ZY sample was hydrophobic. As it was immersed in an aqueous solution, it

could not be soaked up spontaneously. The behavior of the non-charged system has been described

elsewhere [28]. In order to produce a charged system, the electrical conductivity of the nanoporous

phase must be improved, for which 2 parts of Dendritic-3μ copper powders were uniformed mixed

with 1 part of ZY. The copper particle size was 3 μm, fitting well into the gaps among the zeolite

crystals. The ZY-Cu mixture was placed in a steel cylinder and compressed at 50 MPa for 5 minutes

by a type 5582 Instron machine, forming a dense disk. Each disk contained 0.2 g of ZY crystals and

had a diameter of 19 mm. Figure 7-1 depicts the experimental setup of the charged samples. A

ZY-Cu disk was placed on a platinum counter-electrode, separated by a 30 μm thick Celgard-3501

membrane. The electrodes were immersed in a saturated lithium chloride solution (819 g/L) in a

stainless steel cylinder, sealed by a stainless steel piston. The cross-sectional area of the piston was

A_p=286 mm^2. Two silver wires were extended from the electrode and the counter-electrode, respectively, through which an external voltage was applied by a Proteck 6030 DC power supply. The piston was driven into the testing cell at a constant rate of 1 mm/min by the Instron machine. When the pressure reached 85 MPa, the piston was moved out of the testing cell at the same speed. Typical sorption isotherm curves are shown in Figure 7-2. During the loading process, the applied voltage was maintained at either 500 mV or -500 mV.
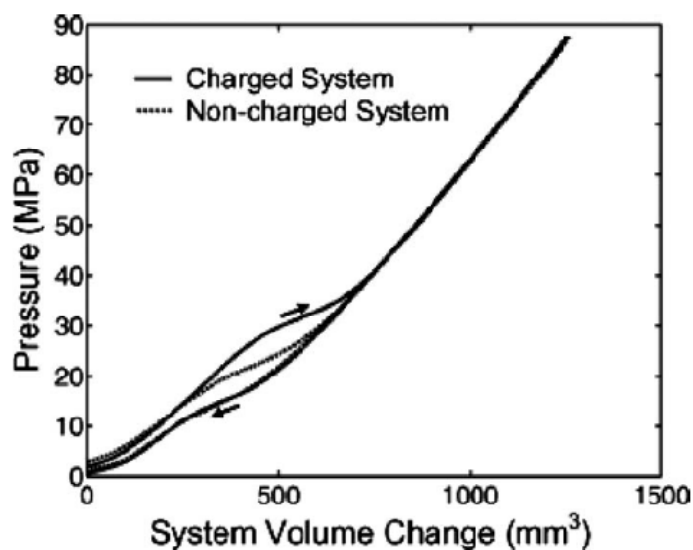

Figure 7-2 Typical sorption isotherm curves

7.3 Results and Discussion

At the beginning stage, the quasi-hydrostatic pressure in the liquid phase, P, is relatively low, which cannot overcome the capillary effect of the nanopores. With a large pressure increase, the system volume variation is relatively small. When P reaches the critical value, the increase in

effective interfacial tension can be balanced by the release of pressure, and thus the pressure-induced infiltration takes place. Around this pressure range, the system volume decreases rapidly, causing the formation of an infiltration plateau in the sorption isotherm curve. In the current study, for self-comparison purpose, the critical infiltration pressure, P_{in}, is taken as the pressure at the middle point of the infiltration plateau. Eventually, when the nanopores are filled, the infiltration plateau ends and the sorption isotherm curve converges back to the low-compressibility profile. The unloading path is different from the loading path, probably due to the influences of entrapped vapor molecules [11, 26], the energy barriers among tetrahedral sites along nanopore surfaces [29], and the heat exchange between the confined liquid and the environment [30], the detailes of which are still under investigation.

The testing data show that the values of P_{in} of the charged system and the non-charge system are considerably different. The P_{in} of the non-charged system is 23 MPa, and that of the systems charged at 500 mV and -500 mV are 33 and 33.2 MPa, respectively. Within the tolerance of the current testing setup, no significant difference can be detected. Clearly, the dominant factor of P_{in} variation is the magnitude of the external electric field, not its direction. Note that the critical pressure of nanopore collapse is at the level of a few hundreds MPs [31]. In the pressure range of the current study the nanoporous structure is quite stable.

The change in interfacial tension with external field has long been known as the electrowetting effect [32]. When a liquid phase and a solid phase contact each other, near the interface the ions in the liquid phase are subjected to different forces from the solid atoms and from

the liquid molecules, and thus the local ion density would be different from that of the bulk phase,

forming a layered structure. The ions in the Gouy-Chapman layer are adsorbed; those in the Stern

layer are relatively mobile. Farther from the solid-liquid interface, the effect of solid surface tends

to vanish [33]. The surface ions induce counter charges in the solid phase, causing a zeta potential,

ϕ. At a constant temperature, the zeta potential can be related to the interfacial tension, γ, through

the Lippmann equation [34]:

$$\partial\gamma/\partial\phi = -\sigma \tag{7.1}$$

where $\sigma = \int C_e \cdot d\phi$ is the surface ion density and C_e is the interface capacity. As a first-order

approximation, C_e may be simplified as a material constant and the interfacial tension can be

calculated by the classic Helmholtz-Perrin equation [35]

$$\gamma = \gamma_0 - \varepsilon\varepsilon_0\phi^2/2d \tag{7.2}$$

where γ_0 is a reference interfacial tension, ε is the dielectric constant, ε_0 is the permittivity of free

space, and d is the characteristic length of the interface double layer. As an external electric field is

applied, the zeta potential is changed and the interfacial tension varies. If the solid and the liquid

phases are in direct contact, usually the applied voltage should be below the thresholds of surface

chemical reactions. In this voltage range, the variation in ϕ can be 20-30%, depending on the ion

properties and concentration [36]. It can be seen that no matter whether ϕ is positive or negative,

the interfacial tension always decreases with the increase of the applied voltage, since the induced

charges in the solid phase would always attract oppositely charged ions. The distribution of ions

tend to be in the most energetically favorable configuration, and therefore the system free energy is

lowered.

The testing data in Figure 7-2 indicate that as a 500 mV voltage is applied, the infiltration pressure changes significantly. As the liquid phase enters the nanopores, the system free energy varies by $\gamma \cdot A$, where $A \approx 2\pi r d_i$ is the area of the nanopore surface exposed to the liquid phase, r is the nanopore radius, and d_i is the effective infiltration depth. The released mechanical energy in the bulk liquid phase can be estimated as $P_{in} \cdot V$, where $V \approx \pi r^2 d_i$ is the infiltration volume. At the equilibrium condition, $\gamma = P_{in} r/2$. For the non-charged system, γ is about 3.4 mJ/m^2; for the charged system, γ is nearly 4.9 mJ/m^2, higher than the former by about 50%. The magnitude of the interfacial tension variation is larger than but close to the prediction of the classic theory. It is insensitive to the direction of the external electric field, which fits with Equation (7.2). The electrode in Figure 7-1 may be regarded as zeolite crystals embedded in a semi-continuous copper matrix. As the external voltage is applied on the copper matrix, it induces surface charges at the nanopore surfaces, which affects the zeta potential.

+ Countercharge in nanopore wall
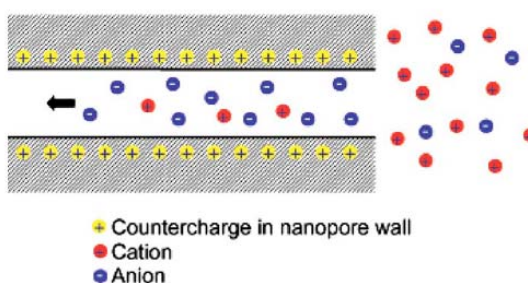● Cation
● Anion

Figure 7-3 Schematic of ion transport in a charged nanopore

A remarkable phenomenon is that, as the external electric field is applied the value of the effective interfacial tension increases. This observation cannot be explained by the classic theory

discussed above, since at a large solid surface the rearrangement of the ions should reduce the system free energy. It may be related to the confinement effect of the nanopore walls, as depicted in Figure 7-3. In a nanopore, the induced charges in nanopore walls would attract oppositely charged ions in the liquid phase and repel like-charged ones. Different from a solid electrode, in the nanoenvironment there is no space for the bulk phase. Since the nanopore size is comparable with the ion size, by taking into account the van der Waals distance, across the cross section there would be only one or a few ions, all of which are directly exposed to the solid atoms. The thermal disarrays that usually exist immediately next to the interface double layer are left outside the nanoporous crystals, far away from the confined liquid. Consequently, a confined, monopolar liquid phase can be formed. To separate the confined ions from the bulk phase, additional work must be done and thus the system free energy tends to increase.

The amount of the additional work done on the charged system can be estimated from Figure 7-2 as the area in between the infiltration plateaus of the charged and non-charged systems, which is around 2 J/g, or 2.8 mJ/m^2. If the intrinsic interfacial tension decrease caused by the applied voltage is 20% (i.e. 0.7 mJ/m^2), the additional work associated with the charge separation in nanopores should be ΔU_s=2.2 mJ/m^2. If the nanopore radius is taken as 0.3 nm, the system free energy change can be calculated as ΔU=$2\Delta U_s/r$=14.7 mJ/mm^3. As a first-order approximation, the amount of the separate charge may be assessed as Q=$\Delta U/C$=3.6 × 10^{-9} C/mm^3, or 2.2 × 10^{10} e/mm^3, where C≈$\varepsilon_e\varepsilon_0/2D$ is the effective system capacity per unit area, ε = 40 is the dielectric constant of the liquid phase, D=5 μm is the average radius of ZY crystals, and "e" indicates electron

charge. It can be seen that Q is around one-billionth of the ion density of saturated lithium chloride solution $(1.2 \times 10^{19}$ e/mm^3).

Because of the small nanopore size of the zeolite, the confined ions cannot be fully solvated by water molecules, and thus both cations and anions may be in direct contact with the solid atoms. Since the ion charges of lithium cation and chlorine anion are the same and the solid nanopore surface is quite neutral [37], as the direction of the external electric field is shifted the ion behaviors in nanopores would not be significantly affected, which explains why the value of system free energy change is only dependent on the magnitude of the applied voltage.

7.4 Conclusions

In summary, it is observed in experiment that the characteristics of field responsiveness of ion transport in nanopores are fundamentally different from that at a large solid surface. The effective interfacial tension increases significantly as an external electric field is applied, which can be attributed to the charge separation associated with the formation of a monopolar confined liquid phase.

Chapter 7, in full, is a reprint of the material as it appears in Applied Physics Letter. Lu, Weiyi; Han, Aijie; Kim, Taewan; Punyamurtula, Venkata K.; Chen, Xi; Qiao, Yu. Field-responsive ion transport in nanopores. 94, 023106.1-3 (2009). The dissertation author was the primary investigator/author of this paper.

References

[1] Joeseph, S; Mashl, R; Jakobsson, E; Aluru, N. Electrolytic transport in modified carbon nanotubes. Nano Letters. 2003. 3, 1399-1403.

[2] Cory, S; Liu, Y; Glavinovic, M. Interfacial interactions of glutamate, water and ions with carbon nanopore evaluated by molecular dynamics simulations. Biochimica et Biophysica Acta. 2007.1768, 2319-2341.

[3] Sumikama, T; Saito, S; Ohmine, I. Mechanism of ion permeation in a model channel: free energy surface and dynamics of K+ ion transport in an anion-doped carbon nanotube. Journal of Physical Chemistry B. 2006. 110, 20671-20677.

[4] Huang, L; Shao, Q; Lu, L; Lu, X; Zhang, L; Wang, J; Jiang, S. Helicity and temperature effects on static properties of water molecules confined in modified carbon nanotubes. Physical Chemistry Chemical Physics. 2006. 8, 3836-3844.

[5] Murray, R. Nanoelectrochemistry: metal nanoparticles, nanoelectrodes, and nanopores. Chemical Reviews. 2008.108, 2688-2720.

[6] Lu, D; Aksimentiev, A; Shih, A; Cruz-Chu, E; Freddolino, P; Schulten, K. The role of molecular modeling in bionanotechnology. Physical Biology. 2006. 3, S40-S53.

[7] Zhang, Y; Zhang, B; White, H. Electrochemistry of nanopore electrodes in low ionic strength solutions. Journal of Physical Chemistry B. 2006. 110, 1768-1774.

[8] Cao, G; Qiao, Y; Zhou, Q; Chen, X. Infiltration behaviour of water in a carbon nanotube under external pressure. Philosophical Magazine Letters. 2008. 88, 371-378.

[9] Weng, M; Lee, W; Ju, S; Chao, C; Hsieh, N; Chang, J; Chen, H. Adsorption of water molecules inside a Au nanotube: a molecular dynamics study. Journal of Chemical Physics. 2008. 128, 174705.

[10] Liu, L; Qiao, Y; Chen, X. Pressure-driven water infiltration into carbon nanotube: The effect of applied charges. Applied Physics Letters. 2008. 92, 101927.

[11] Qiao, Y; Cao, G; Chen, X. Effects of gas molecules on nanofluidic behaviors. Journal of the American Chemical Society. 2007. 129, 2355-2359.

[12] Liu, W; Karpov, E; Zhang, S; Park, H. An introduction to computational nanomechanics and materials. Computer Methods in Applied Mechanics and Engineering. 2004. 193, 1529-1578.

[13] Han, A; Chen, X; Qiao, Y. Effects of the addition of electrolyte on liquid infiltration in a hydrophobic nanoporous silica gel. Langmuir. 2008. 24, 7044-7047.

[14] Han, A; Qiao, Y. Effects of nanopore size on properties of modified inner surfaces. Langmuir. 2007. 23, 11396-11398.

[15] Qiao, Y; Han, A; Punyamurtula, V. Electrification of a nanoporous electrode in a continuous flow. Journal of Physics D: Applied Physics. 2008. 41, 085505.

[16] Qiao, Y; Punyamurtula, V; Han, A. Thermally induced capacitive effect of a nanoporous monel. Applied Physics Letters. 2007. 91, 153102.

[17] Tanimura, A; Kovalenko, A; Hirata, F. Structure of electrolyte solutions sorbed in carbon nanospaces, studied by the replica RISM theory. Langmuir. 2007. 23, 1507-1517.

[18] McCash, E. Surface Chemistry. Oxford Univesrsity Press. 2001.

[19] Yang, J; Lu, F; Kostiuk, L; Kwok, D. Electrokinetic power generation by means of streaming potentials: a mobile-ion-drain method to increase the streaming potentials. Journal of Nanoscience and Nanotechnology. 2005. 5, 648-652.

[20] Van der Heyden, F; Stein, D; Besteman, K; Lemay, S; Dekker, C. Charge inversion at high ionic strength studied by streaming currents. Physical Review Letters. 2006. 96, 224502.

[21] Qiao, Y; Punyamurtula, V; Han, A. Mechanoelectricity of a nanoporous monel–electrolyte solution system. Journal of Power Sources. 2007. 164, 931-933.

[22] Qiao, Y; Punyamurtula, V; Han, A. Thermal-to-electric energy conversion of a nanoporous carbon. Journal of Power Sources. 2008. 183, 403-405.

[23] Bockris, J; Khan, S. Surface Electrochemistry. Springer. 1993.

[24] Shukla, A; Sampath, S; Vijayamohanan, K. Electrochemical supercapacitors: energy storage beyond batteries. Current Science. 2000. 79, 1656-1661.

[25] Han, A; Qiao, Y. Pressure-induced infiltration of aqueous solutions of multiple promoters in a nanoporous silica. Journal of the American Chemical Society. 2006. 128, 10348-10349.

[26] Han, A; Kong, X; Qiao, Y. Pressure induced liquid infiltration in nanopores. Journal of Applied Physics. 2006. 100, 014308.

[27] Kong, X; Qiao, Y. Thermal effects on pressure-induced infiltration of a nanoporous system. Philosophical Magazine Letters. 2005. 85, 331-337.

[28] Han, A; Qiao, Y. A volume-memory liquid. Applied Physics Letters. 2007. 91, 173123.

[29] Chen, X; Cao, G; Han, A; Punyamurtula, V; Liu, L; Culligan, P; Kim, T; Qiao, Y. Nanoscale fluid transport: size and rate effects. Nano Letters. 2008. 8, 2988-2992.

[30] Qiao, Y; Punyamurtula, V; Xian, G; Karbhari, V; Han, A. Conversion of mechanical work to interfacial tension in a nanoporous silica gel. Applied Physics Letters. 2008. 92, 063109.

[31] Han, A; Punyamurtula, V; Lu, W; Qiao, Y. Deformation of a nanoporous silica under compressive loading. Journal of Applied Physics. 2008. 103, 084318.

[32] Bagotsky, V. Fundamentals of Electrochemistry. Wiley Interscience. 2005.

[33] Girault, H. Analytical and Physical Electrochemistry. EFPL Press. 2004.

[34] Bockris, J; Reddy, A. Modern Electrochemistry. Springer. 2001.

[35] Adamson, A; Gast, A. Physical Chemistry of Surfaces. Wiley Interscience. 1997.

[36] Hamann, C; Jamnett, A; Vielstich, W. Electrochemistry. John Wiley & Sons. 1998.

[37] Jansen, J; Stocker, M; Weitkamp, J; Karge, H. Advanced Zeolite Science and Applications. Elsevier Science. 1994.

Chapter 8 Polymer Based System

8.1 Introduction

Composite materials, especially polymer matrix composites (PMC), have been intensively studied for energy absorption applications [1]. When the temperature is close to or higher than the glass transition temperature (T_g), the polymer matrix is usually viscoelastic. With an external loading, either dynamic or quasi-static, the relaxation of the network polymer chains would cause a considerable energy dissipation effect, which works quite well under cyclic loadings [2]. The reinforcements can be continuous fibers, short fibers, particulates, and/or platelets [3-5]. They can significantly enhance the overall stiffness, strength, and toughness, as well as the anisotropic and heterogeneous properties [6]. If the bonding between the matrix and the reinforcements is relatively weak, debonding can take place when the local stress exceeds the critical value, which is often promoted by the stress concentration and/or wave redispersion [7]. As a first-order estimation, debonding of reinforcements of an overall interfacial area of A would result in an energy dissipation of

$$E = \gamma_d \cdot A \qquad (8.1)$$

where γ_d is the effective surface free energy.

It can be seen that if the interfacial area, A, increases, the theoretical upper limit of the energy absorption capacity is higher, and, thus, using nanometer (nm) sized fillers of ultralarge surface to volume ratios becomes an attractive concept [8]. For instance, if 1 g of carbon nanotubes

(CNTs) are embedded in a polymer matrix and if they can fully debond, 10^2 to 10^3 Joules of energy can be dissipated. The very high stiffness and strength of CNTs assure that they have the ability to store sufficient strain energy to trigger the interface debonding.

However, under a compressive loading, especially when the strain rate is high, debonding would inevitably cause local weakening, which makes the stress wave distribution highly nonuniform [9]. As a result, shear localization can significantly limit the overall energy absorption efficiency. In a few narrow shear bands, local deformation can rapidly develop, and catastrophic failure may happen without bulk-distributed damages; i.e. the large interface area cannot be fully utilized [10]. This embrittlement effect has become a major challenge that must be overcome before nanocomposites can be widely applied in engineering practice. Moreover, while interface debonding can occur relatively easily under a tensile or shear stress, in a compressive stress field it can be difficult.

The concept of NMF liquid provides a promising way to circumvent these problems. In an NMF liquid, the matrix must be a liquid or a gel, which is flowable under an external loading. The fillers are nanoporous particles. The particle size can be quite large, in the range of a fraction of μm to a few mm. The particles contain large volume fractions of nm-sized pores, with the pore size of 0.6 to 100 nm. While the outer surface area is relatively small, the area of the nanopore inner surface is ultralarge, usually 10^2 to 10^3 m^2 per gram.

One difficulty associated with the NMF materials technique is that the liquid phase must be contained in a packaging system, either a cellular or a vascular structure, which increases the

system complexity. While hydrogel matrix NMF composites have been developed [11, 12], they can merely stand alone and still cannot be directly used for load-bearing components.

When a material is subjected to intense stress waves, due to the small time scale of deformation, the dissipated energy cannot be transported and thus the local temperature can greatly increase by a few hundreds ^{o}C in a short period of time, which may cause melting of polymers and even metals [13]. The energy dissipation can be caused by debonding, cell buckling, internal friction, etc. [14], or by the shock viscosity effect, which is related to the irreversibility of loading and unloading paths [15]. It is envisioned that, if a nanoporous phase is embedded in a composite, the softened materials, e.g. a low melting point polymer, may be intruded into the nanopores. The small mass density of the nanoporous phase also helps with reducing the overall weight. However, flow of viscous materials in confining nanoenvironment may be difficult. Currently, little experimental data are available in open literature.

8.2 Experimental

In the current study, we investigated a Cabot BP-2000 nanoporous carbon. The material was dried in air at 80 ^{o}C for 2 hours, and heated in a tube furnace in nitrogen environment at 550 ^{o}C for 6 hours. After rinsing in acetone and warm water repeatedly, the carbon sample was soaked with saturated water steam at 180 ^{o}C for 12 hours. The steam flow rate was maintained at 30 ml/min. After vacuum drying at 80 ^{o}C for 4 hours, 2.5 g of carbon was mixed with 40 ml of dry toluene in a round-bottom flask. The mixture was gently stirred for 10 minutes, during which 1 ml of

chlorotrimethylsilane was injected. Then, the temperature was increased to 95 ^{o}C by a thermal mantle and the mixture was vigorously stirred for 48 hours. The silane treated material was filtered, washed with dry toluene and warm water repeatedly, and dried in vacuum at 80 ^{o}C for 6 hours. The nanoporous structure was characterized in a Micromeritics ASAP-2020 Analyzer (Figure 2-5), as shown in Figure 8-1 and 8-2.
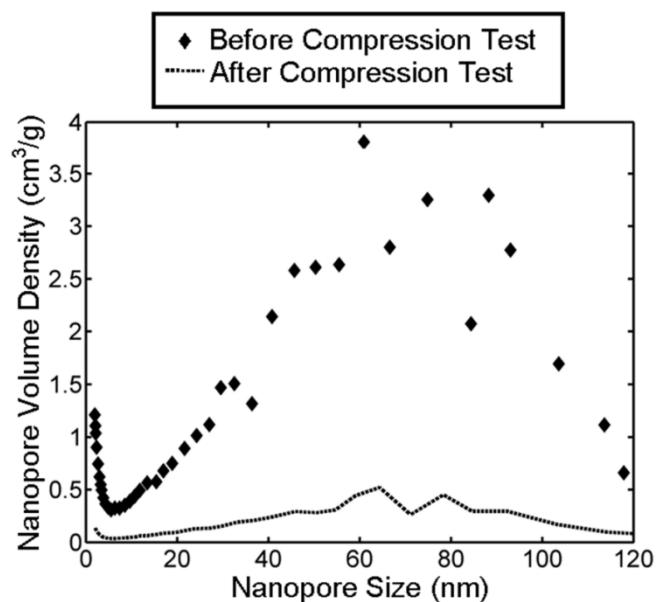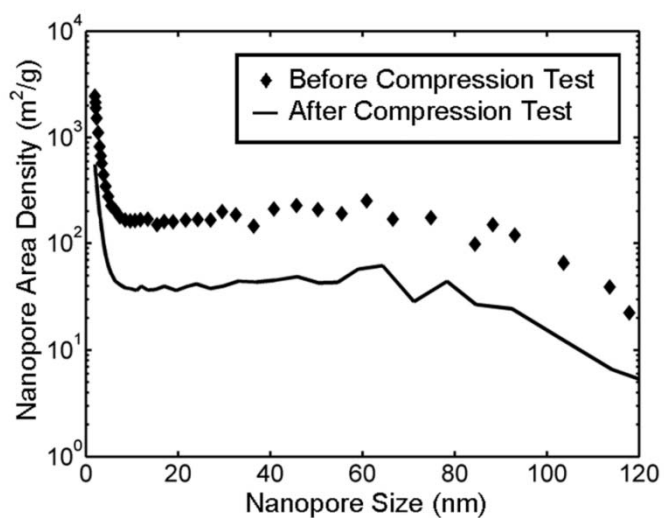

Figure 8-1 The nanopore volume distributions before and after the compression test

Figure 8-2 The nanopore surface area distributions before and after the compression test

The surface treated nanoporous carbon was mixed with polypropylene (PP) pellets, with the mass ratio of 1:20. By using a heating plate, PP was melted and the mixture was blended at 200 rpm for 10 minutes, so that the carbon particles dispersed uniformly, and then at 10 rpm for 10 minutes, so that the content of entrapped air was minimized. The mixture was cooled in air, forming a PP matrix composite, and cut into cylinders with the diameter of 19 mm.

In a stainless steel cylinder, a PP composite cylinder was sealed from the top by a stainless steel piston. The cross-sectional area of the piston was 286 mm^2. The sealing was assured by two reinforced Teflon o-rings. The testing temperature was controlled by an oil bath either at room temperature (20 ^{o}C) or at elevated temperature (280 ^{o}C). In a type 5582 Instron machine, the piston was compressed into the cylinder at a constant rate of 0.5 mm/min. When the load reached about 700 N, the piston was moved out at the rate of -0.5 mm/min. Similar loading-unloading cycles were repeated for two times. Figure 8-3 shows typical compression isotherm curves.
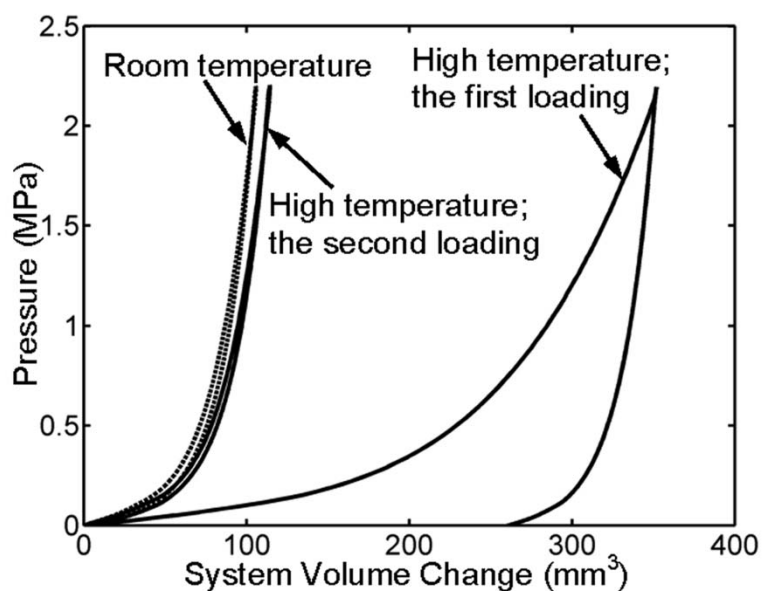

Figure 8-3 Typical compression curves

After the compression test, the composite was cooled in air, milled into powders, and washed and filtered in acetone and methanol repeatedly, until about 20 mg of carbon particles were collected. The collected carbon powders were characterized again in the Micromeritics ASAP-2000 Analyzer.

8.3 Results and Discussion

Figure 8-1 shows clearly that, before the compression test, the nanopore volume follows a bimodal distribution. The higher peak is at about 60 nm, and the lower peak is at about 2 nm. Figure 8-2 shows that, although the small nanopores are of a relatively low volume fraction, their surface area is quite large, as it should be, since the surface area is proportional to V/d, with V being the characteristic volume and d being the characteristic size. The nanopore volume density at the lower peak is about 1/3 of that at the higher peak, and the nanopore area density of the former is nearly 10 times larger.

The dashed lines in Figure 8-3 indicate the system behavior at room temperature, which is quite linear. The compressibility is determined by the bulk modulus of the composite material and the compliance of the loading machine. At the peak load of 700 N, the pressure is around 2.2 MPa. In this pressure range, no plastic deformation takes place in both the PP phase and the carbon phase, and therefore the loading and unloading paths nearly overlap with each other.
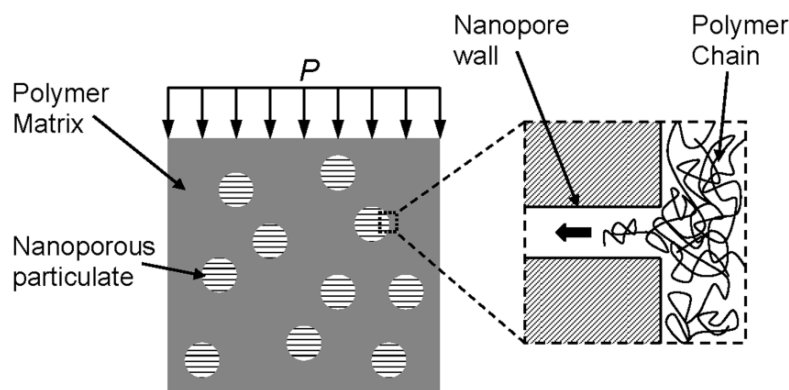
Figure 8-4 Schematic of the thermally sensitive composite functionalized by nanoporous carbon

The melting point of polypropylene is $T_m = 160\ ^{\circ}$C. It is softened when the temperature is raised to 280 $^{\circ}$C. At this temperature, as the external pressure is applied a large deformation occurs. Since the compressibility of the liquid phase is even smaller than its solid counterpart [16], the deformation must be attributed to the infiltration of PP melt into the nanopores, as depicted in Figure 8-4. The inner surface of nanopores of the BP2000 under investigation is coated by a silane monolayer, which is nonwettable to the PP macromolecules [17]. When the carbon particles and the PP melt are mixed under ambient pressure, the PP chains would stay outside the nanopores to minimize the system free energy. Above T_m, the free volume among the PP chains greatly increases and they can relatively easily slide against each other. As the piston is compressed into the cylinder, a strain energy builds up in the PP matrix:

$$U = P^2/2B \tag{8.2}$$

where P is the pressure and B is the effective bulk modulus. When the PP chains enter the nanopores, the system free energy increases by

$$U_I = \Delta\gamma \cdot A_i \qquad (8.3)$$

where $A_i = 2/r$ is the specific contact area, with r being the effective nanopore radius. When U and U_I are balanced by each other, the equilibrium condition is reached, at which

$$P = \sqrt{4B \cdot \Delta\gamma/r} \qquad (8.4)$$

According to the measured curve, P is in the range of 0.05 to 2 Mpa. The average infiltration pressure is about 1 Mpa. If the corresponding pore size is taken as the higher modal value, 60 nm, the value of $\Delta\gamma$ can be estimated as 600 mJ/m^2, with the value of B being set to 2500 MPa. This value of interfacial tension is relatively large compared with that of carbon-water system [18], compatible with the fact that the surface tension of PP melt is larger.

When unloading begins, the slope of the sorption isotherm curve is quite large, and does not decrease until the pressure is relatively low. When P is 0.2 MPa, the slope is reduced by nearly 50%. As P is entirely removed, there is still a significant amount of residual deformation of about 270 mm^3. Clearly, the confined PP melt does not defiltrate, and thus the sorption isotherm curve is highly hysteretic. The non-defiltration may be related to the large aspect ratio of the nanopores, where the liquid phase in the middle section may be regarded as being confined in an infinitely long channel. Under this condition, the driving force of defiltration associated with the positive interfacial tension is balanced. The difficulty in formation and growth of nanobubbles can also lead to the blocking of confined matters, especially when the nanopore size is larger than 1-2 nm [19, 20].

At the second loading, the loading and unloading paths are nearly identical, both of which

are similar to the unloading section of the first loading. The slope is close to that at the high-pressure segment, suggesting that no infiltration or defiltration is involved. It is clear that, as the nanopores remain being occupied, the system compressibility is relatively small; i.e. the infiltration mechanism works only in the first loading loop, suitable to one-time protection applications. After the first loading cycle, the nanoporous carbon particulates are strongly bonded with the matrix by the penetrating PP phase.

According to Figure 8-1 and 8-2, the porosity changes significantly after the compression test. After the test, the peak in the larger nanopore size range vanishes. The relatively small residual nanopore volume may be caused by the loss of confined PP during the filtering and washing process. The peak of the smaller nanopore size, although considerably lowered, is still evident. That is, most of the smallest nanopores of the sizes around 1-2 nm remain empty. If they were filled by the PP phase during loading and the confined PP macromolecules defiltrated during unloading, associated with the significantly different nanopore sizes of the two peaks, the infiltration plateau in Figure 8-3 would contain two stages, which is not observed in the experiment. If the excess interfacial tension is at the same level in the small and large nanopores, the infiltration pressure in the smallest nanopores should be higher than that of the large nanopores by 30-60 times, beyond the capacity of the current system. In fact, under such a high pressure, the nanoporous carbon pariculates can be crushed, which is another possible energy absorption mechanism but not the focus of the current study.

8.4 Conclusions

Through a compression experiment, it is validated that as nanoporous carbon particulates are embedded in a polypropylene matrix, at an elevated temperature the polymer phase can be forced into the nanopores, leading to a significant energy dissipation effect. As the pressure is lowered, the confined polymer chains do not defiltrate. The accessible nanopores are of relatively large sizes. In the smallest nanopores around 1-2 nm, in the pressure range of the current study, infiltration does not occur.

Chapter 8, in full, is a reprint of the material as it appears in Journal of Materials Research. Lu, Weiyi; Punyamurtula, Venkata K.; Han, Aijie; Kim, Taewan; Qiao, Yu. A thermally sensitive energy-absorbing composite functionalized by nanoporous carbon. 24, 3308-3312 (2009). The dissertation author was the primary investigator/author of this paper.

References

[1] Barbero, E. Introduction to composite materials design. Taylor Francis. 1999.

[2] Brinson, H; Brinson, L. Polymer engineering science and viscoelasticity. Springer. 2008.

[3] Bunsell, A. Fiber reinforcements for composite materials. Elsevier. 1988.

[4] Mazumdar, S. Composites manufacturing: materials, product, and process engineering. CRC Press. 2002.

[5] Pinnavaia, T; Beall, G. Polymer-clay nanocomposites. John Wiley Sons. 2000.

[6] Daniel, I; Ishai, O. Engineering mechanics of composite materials. Oxford University Press. 1994.

[7] Lu, G; Yu, T. Energy absorption of structures and materials. Woodhead Publishing. 2003.

[8] Twardowski, T. Introduction to nanocomposite materials. Destech Publishing. 2007.

[9] Park, H; Liu, W. An introduction and tutorial on multiple scale analysis in solids. Computer Methods in Applied Mechanics and Engineering. 2004. 193, 1733-1772.

[10] Kong, X; Chakravarthula, S; Qiao, Y. Evolution of collective damage in a polyamide 6-silicate nanocomposite. International Journal of Solids and Structures. 2006. 43, 5969-5980.

[11] Surani, F; Han, A; Qiao, Y. Thermal recoverability of a polyelectrolyte modified, nanoporous silica based system. Journal of Materials Research. 2006. 21, 2389-2392.

[12] Surani, F; Qiao, Y. Energy absorption of a polyacrylic acid partial sodium salt modified nanoporous system. Journal of Materials Research. 2006. 21, 1327-1330.

[13] Nesterenko, V. Dynamics of heterogeneous materials. Springer. 2001.

[14] Han, A; Punyamurtula, V; Qiao, Y. Heat generation associated with pressure induced infiltration in a nanoporous silica gel. Journal of Materials Research. 2008. 23, 1902-1906.

[15] Yoganandan, N; Zhang, J; Pintar, F. Force and acceleration corridors from lateral head impact. Traffic Injury Prevention. 2004. 5, 368-373.

[16] Kleman, M; Lavrentovich, O. Soft matter physics. Springer-Verlag. 2003.

[17] Ibach, H. Physics of surfaces and interfaces. Springer-Verlag. 2006.

[18] Han, A; Qiao, Y. Controlling infiltration pressure of a nanoporous silica gel via surface treatment. Chemistry Letters. 2007. 36, 882-883.

[19] Qiao, Y; Cao, G; Chen, X. Effects of gas molecules on nanofluidic behaviors. Journal of the American Chemical Society. 2007. 129, 2355-2359.

[20] Han, A; Kong, X; Qiao, Y. Pressure induced infiltration in nanopores. 2006. Journal of Applied Physics. 100, 014308.

Chapter 9 Future Research Plan

9.1 Particle Size Effect
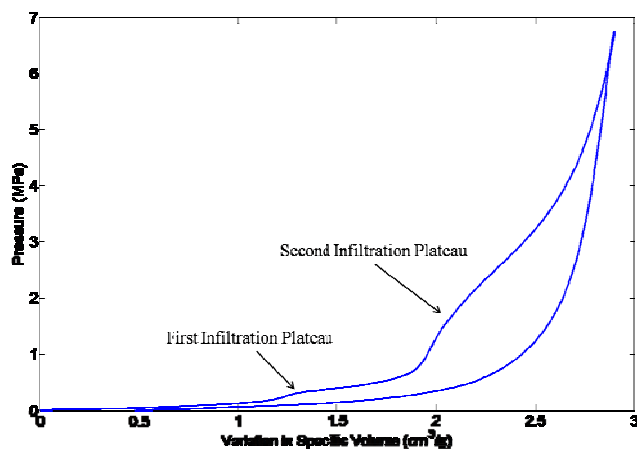
Figure 9-1 A Two-step compression curve of nanoporous silica

In some experiments, we observed an interesting phenomenon: A two-step infiltration behavior could be formed as shown in figure 9-1. The nanoporous material was SP-1000-5 silica from Daiso. The material was in powder form, with the particle size of 4.2 μm. It was analyzed by using a Micromeritics TriStar 3000 gas adsorption analyzer. The effective nanopore size was 102 nm. The specific surface area was 26 m^2/g and the specific nanopore volume was 0.87 cm^3/g. The material was treated by chloro-octyl-dimethyl-sliane, and followed by a chloro-trimethyl-sliane end capping. The surface treatment procedure was similar to the process described in Appendix B.

About 0.2 g treated silica gel was mixed in 6.5 g of saturated aqueous solution of lithium chloride (LiCl). The mixture was sealed in a steel cylinder and tested by a type 5582 Instron

machine. The loading rate was 1 mm/min. When the applied load reached about 1.9 kN, the piston was moved back at the same speed.

Apparently, the higher-pressure plateau was caused by the intrusion of the liquid phase into the nanopores. Since the pose size distribution of this material was narrow, the lower-pressure plateau could not be related to the liquid infiltration. The lower-pressure plateau is equivalent to the beharvior of a porous material with micron sized pores. Note that the particle size of the Dasio silica gel was 5 micron.

As discussed in Chapter 2, due to the density mismatch between the solid and liquid phases, the particles may float on the surface of the liquid phase. Although there are no chemical or physical bonds between the particles, when an external pressure is applied, they "stick" to each other and perform as the micron-pored clusters. That is, the free space in between the particles may act as temporary "pores".

More experiments are needed to understand the mechanism of the lower-pressure "infiltration":

1) Investigate systems with various particle sizes. This is a direct method to validate the above onsideration. Surface treated solid silica particles could be used. Hydrophobic polymer particles such as polypropylene, polyethylene, teflon [1] could also be relevant candidates.

2) Evaluate the effects of surface treatment. As described in Chapter 2, by using different surface modifiers and through end capping, both P_{in} and V_{in} would change.

3) Analyze the effects of the liquid phase. The ion species and concentration in the liquid phase

would significantly affect P_{in}.

9.2 Dynamic Testing

The quasi-static compression experiments shed much light on the fundamental, thermodynamic behaviors of the NMF liquids. However, in many energy absorption applications, the external loadings are dynamic. Thus, dynamic tests such as live blast tests and split Hopkinson pressure bar (SHPB) tests [2, 3] are essential to further investigate the system performance. Figure 9-2 is a schematic of SHPB test setup. During the test, the incident and transmitted signals are recorded by two strain gauges. According to the theory of elasticity, the stress-strain curve of the bars could be calculated. Consequently, the dynamic responses of the NMF liquid, could be analyzed.
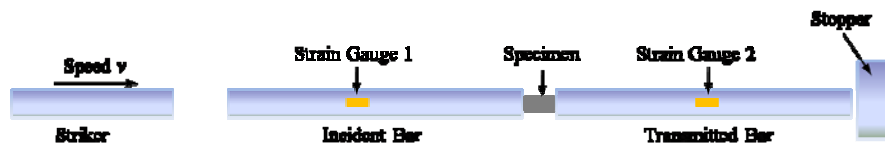
Figure 9-2 Schematic of SHPB test setup

References

[1] Fujinamia, A; Matsunakab, D; Shibutanib, Y. Water wettability non-wettability of polymer materials by molecular orbital studies. Polymer. 2009. 50, 716-720.

[2] Song, B; Chen, W. SHPB techniques for characterizing soft materials. Latin American Journal of Solids and Structures. 2005. 2, 113-152.

[3]   Jiang, F; Vecchio, K; Rohatgi, A. Analysis of modified split Hopkinson pressure bar dynamic fracture test using an inertia model. International Journal of Fracture. 2004. 126, 143-164.

Appendix A Surface Treatment Procedure for Micro- and Meso-Porous Materials

1. Activation

About 1 g of nanoporous silica, [Supelco 13662 (Sigma-Aldrich)], was hydroxylated in 100 mL distilled water in a round-bottom flask at 40 ℃ for 3 hours. After that, the powders were filtered out, washed by distilled water and dried at 80 ℃ for 48 hours in a VWR 1410 vacuum oven (Figure A-1).

Figure A-1 VWR 1410 vacuum oven

2. Chloro-octyl-dimethyl-silane treatment

The activated silica particles were dispersed in a solvent, 40 mL of anhydrous toluene, and 10 mL chloro-octyl-dimethyl-silane (Sigma-Aldrich) was added into the mixture, (Figure A-2), and stirred for 10 minutes. The flask was put in a heating mantle and the mixture was

refluxed at 95 ℃ for 72 hours. The treatment was completed by using a simplified Dean-Stark

apparatus, as shown in Figure A-3. The cooled mixture was filtered and washed consecutively on

a filter (Figure A-4) with 100 mL toluene, 100 mL acetone, and 100 mL distilled water to remove

the residual of reagent and by-products such as HCl. The particles were dried at 80 ℃ under

vacuum for 48 hours.

Figure A-2 Adding surface modifier
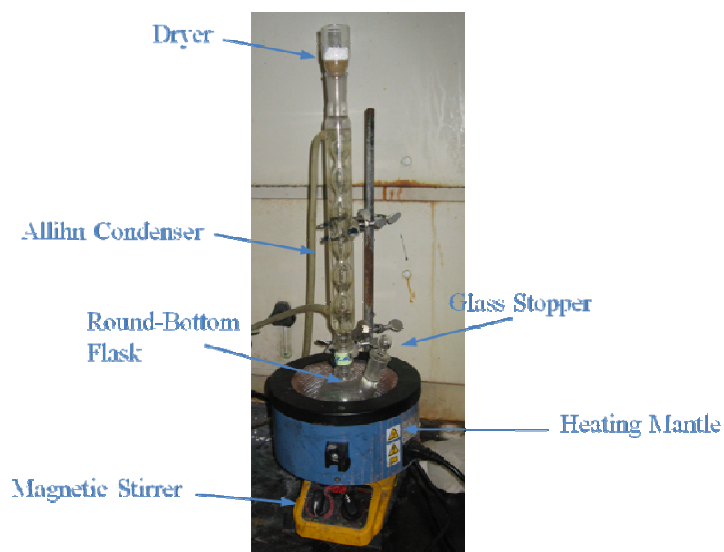
Figure A-3 Simplified Dean-Stark apparatus
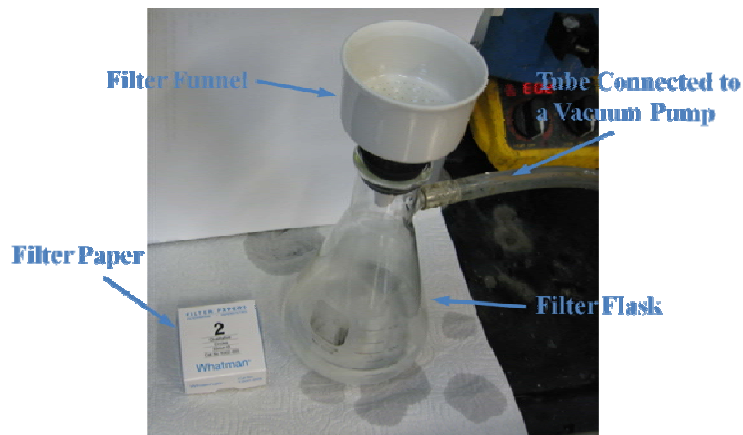
Figure A-4 Filtering system of surface treatment

3. Chloro-trimethyl-silane end capping

End capping may be regarded as a second round surface treatment by using smaller-sized surface modifier. Here, chloro-trimethyl-silane (Sigma-Aldrich) was used as the modifier. The surface treatment, washing, and drying conditions are similar to the previous step 2.

Appendix B Surface Treatment Procedure for Macro- Porous Materials

1. Dehydration

About 0.5 g of nanoporous silica, SP-1000-5 (Daiso), was mixed with 50 mL anhydrous toluene and stir vigorously for 3 hours at 90 ℃ in the simplified Dean-Stark apparatus. After that, the heating mantle was turned off and the mixture was cooled down to room temperture.

2. Chloro-octyl-dimethyl-silane treatment

At room temperature, 10 mL chloro-octyl-dimethyl-silane (Sigma-Aldrich) was added into the cooled mixture and stirred for 10 minutes. Then, 1 mL pyridine was added into the flask and stirred for 10 minutes. The temperature was then increased to 95 ℃ and maintained for 5 hours. When the surface treatment was completed, the mixture was quenched by ethanol. Ethanol was also used to wash the material for 3 rounds in the filter. The particles were vacuum dried at 70 ℃ for 48 hours.

3. Chloro-trimethyl-silane end capping

Similar as the treatment for mico- and meso-porous materials, end capping was employed to improve the surface properties. Here, chloro-trimethyl-silane (Sigma-Aldrich) was used as the modifier. The surface treatment, quenching, washing, and drying conditions were similar to the previous step 2.

Appendix C Technical Drawings
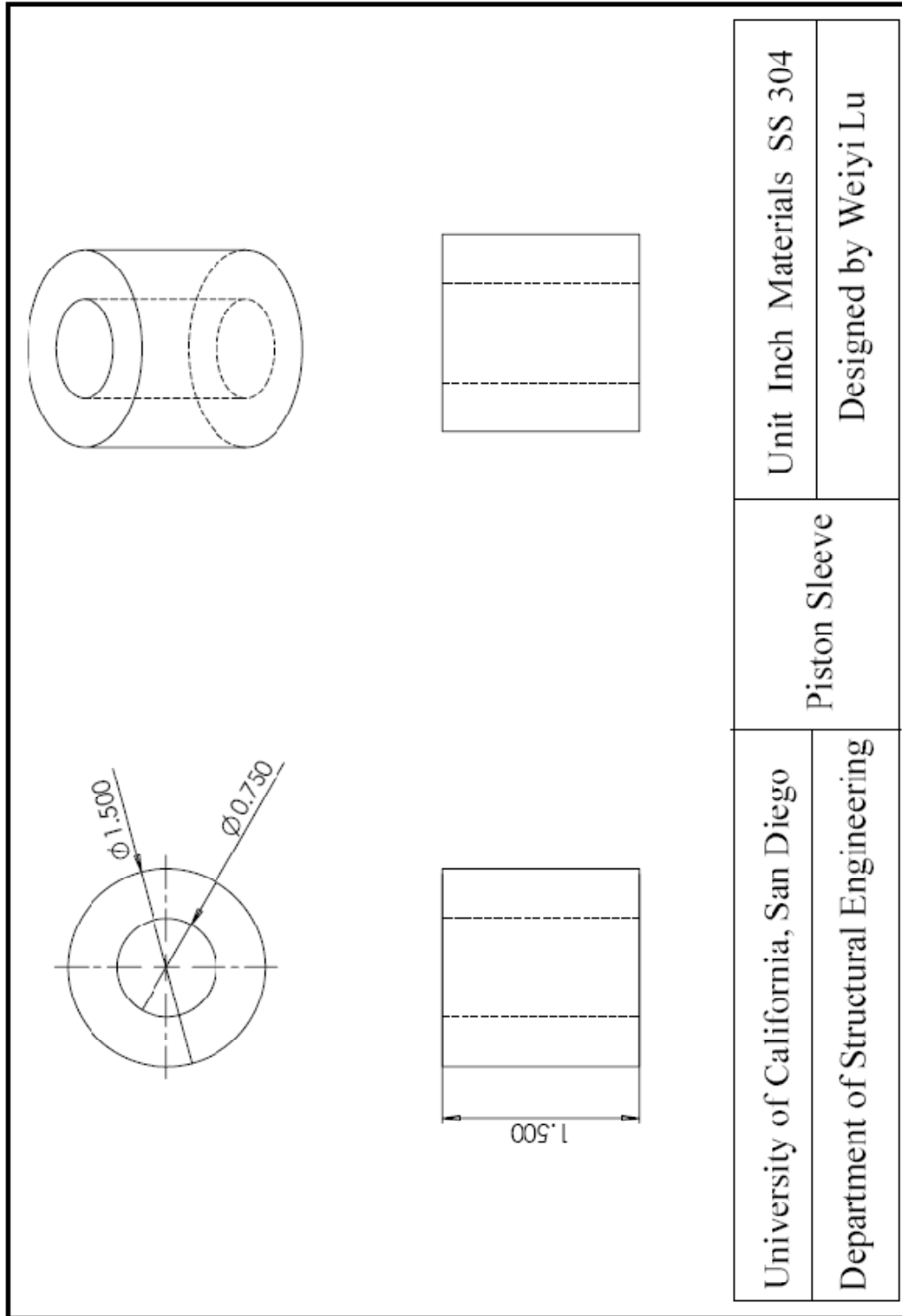
Figure C-1 Compression test cell - Piston sleeve
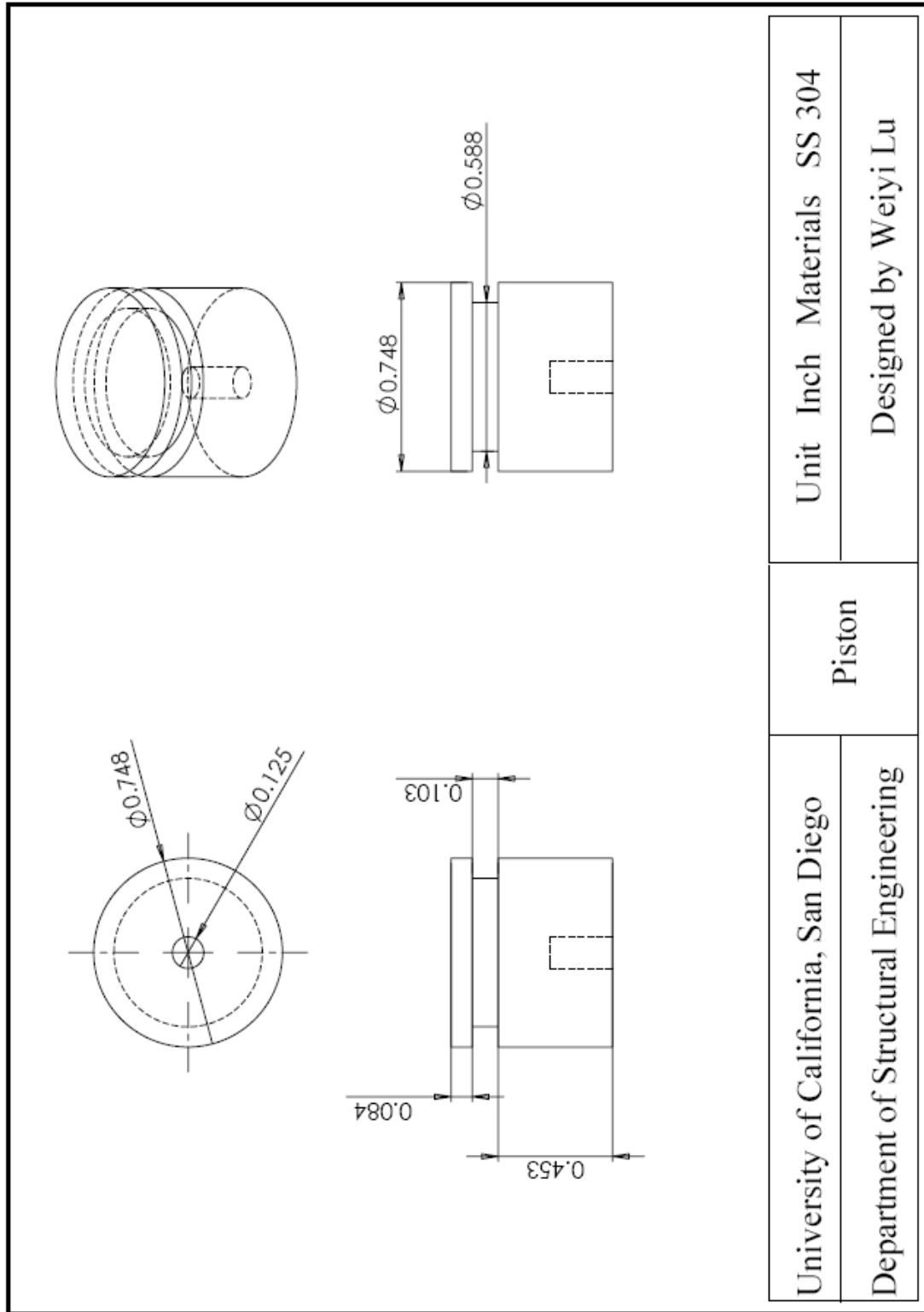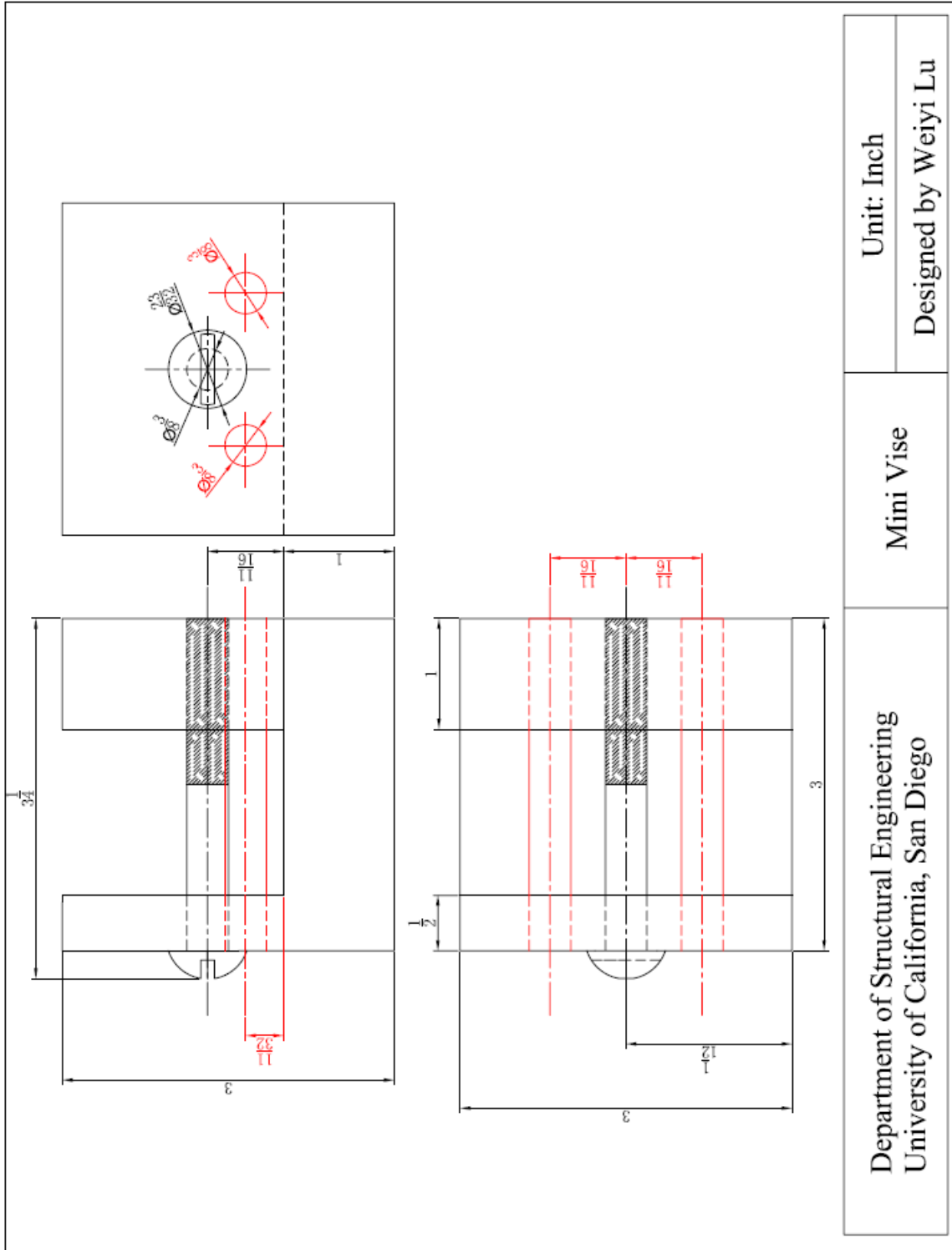
Figure C-2 Compression test cell - Piston

Figure C-3 Mini Vise

Figure C-4 Fatigue test system - Piston
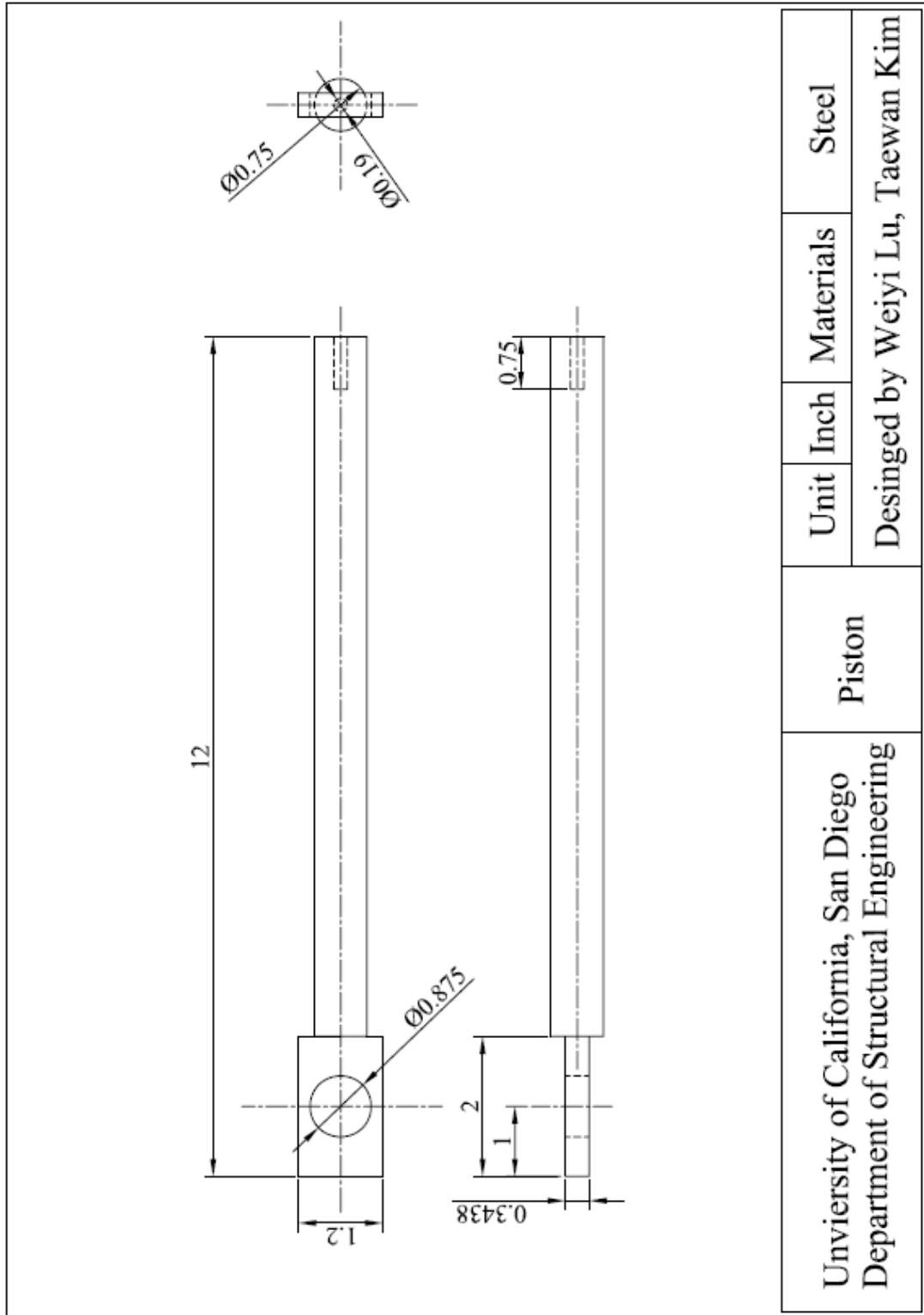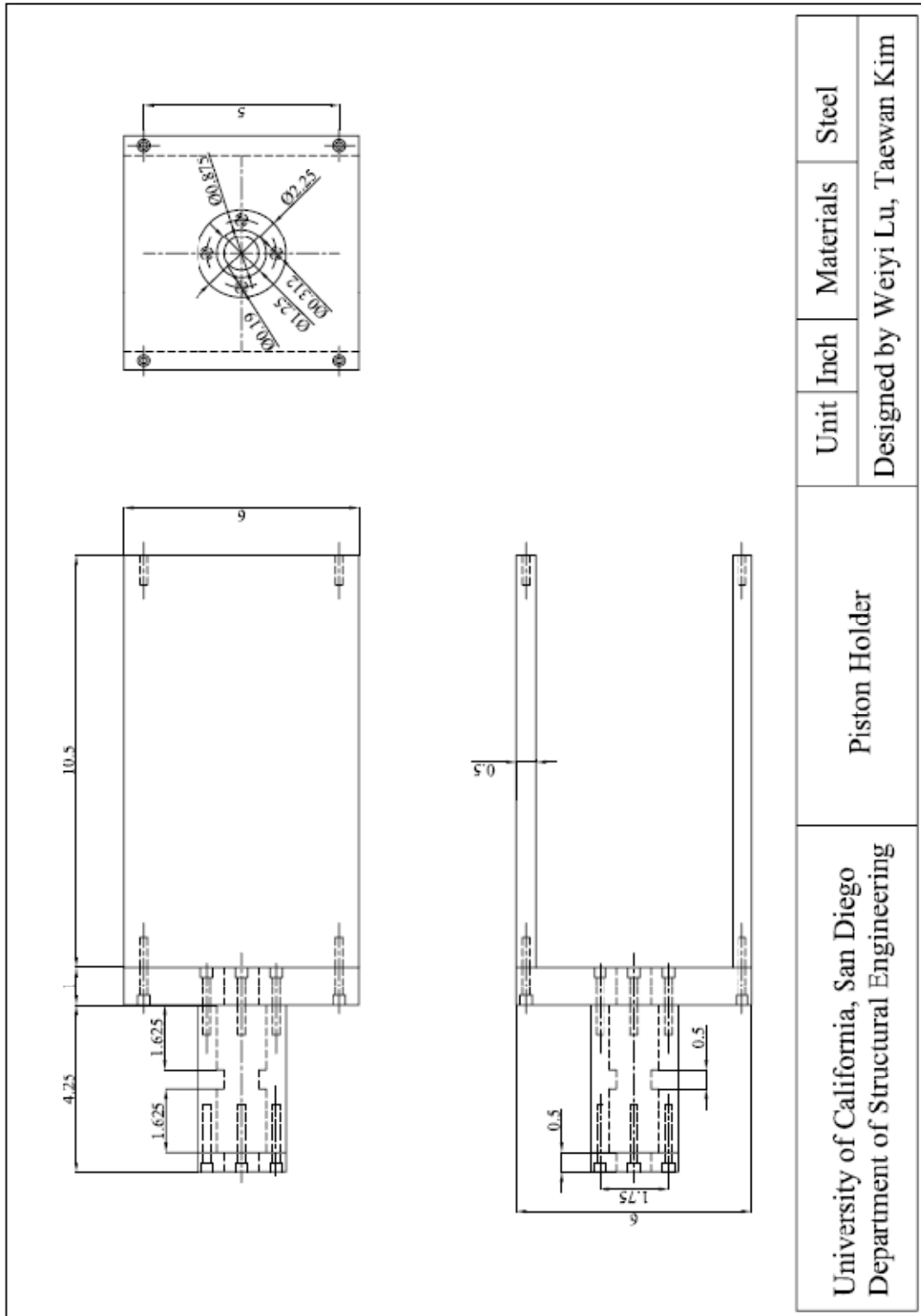
Figure C-5 Fatigue test system - Piston holder
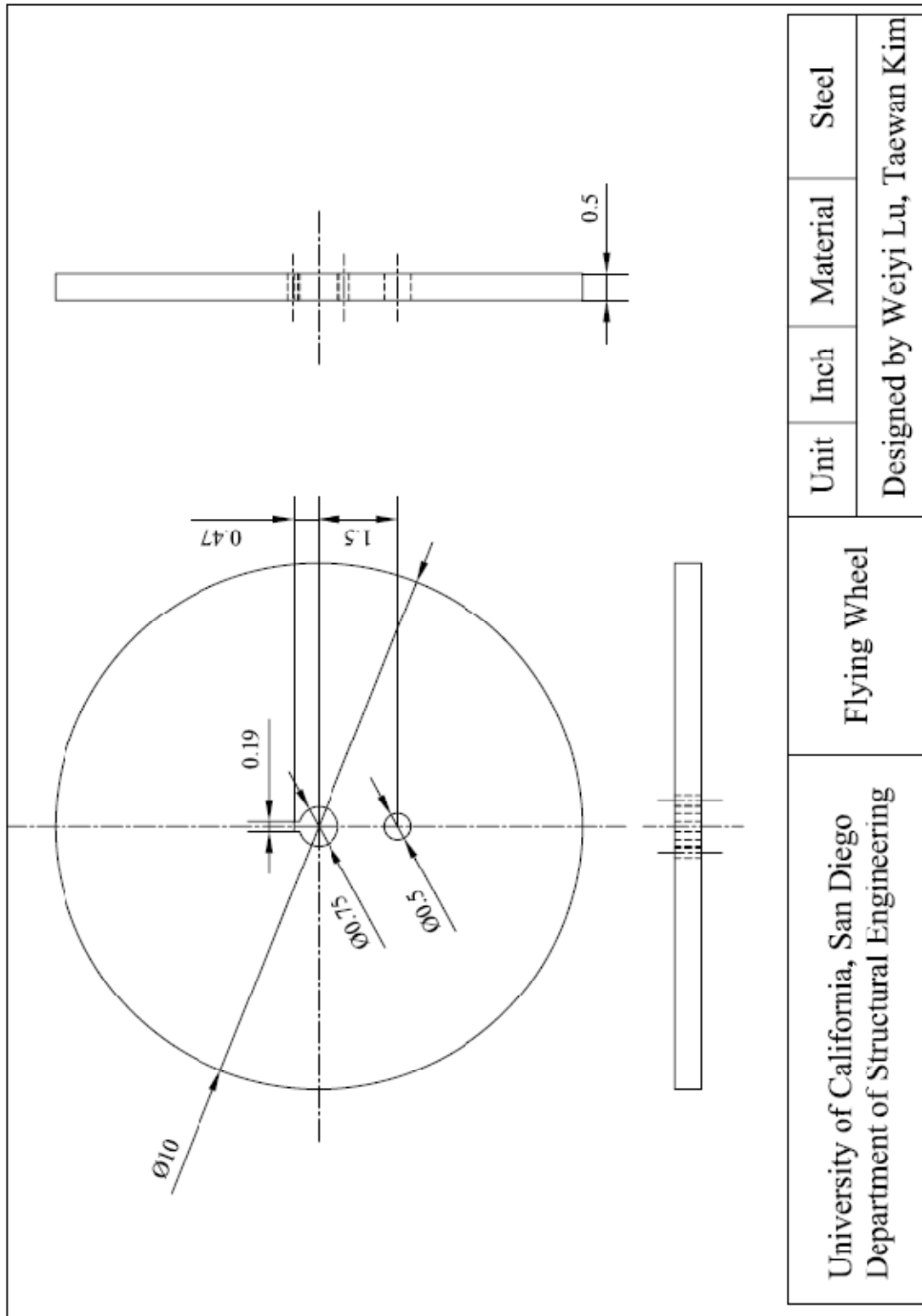
Figure C-6 Fatigue test system - Flying wheel

Ø0.125

0.25

Ø1.4

Ø0.75

0.47

0.19

Ø2

Ø0.19

Unit	Inch	Materials	Alloy 6020

Designed by Weiyi Lu, Taewan Kim

Rear Flying Wheel Holder

University of California, San Diego
Department of Structural Engineering
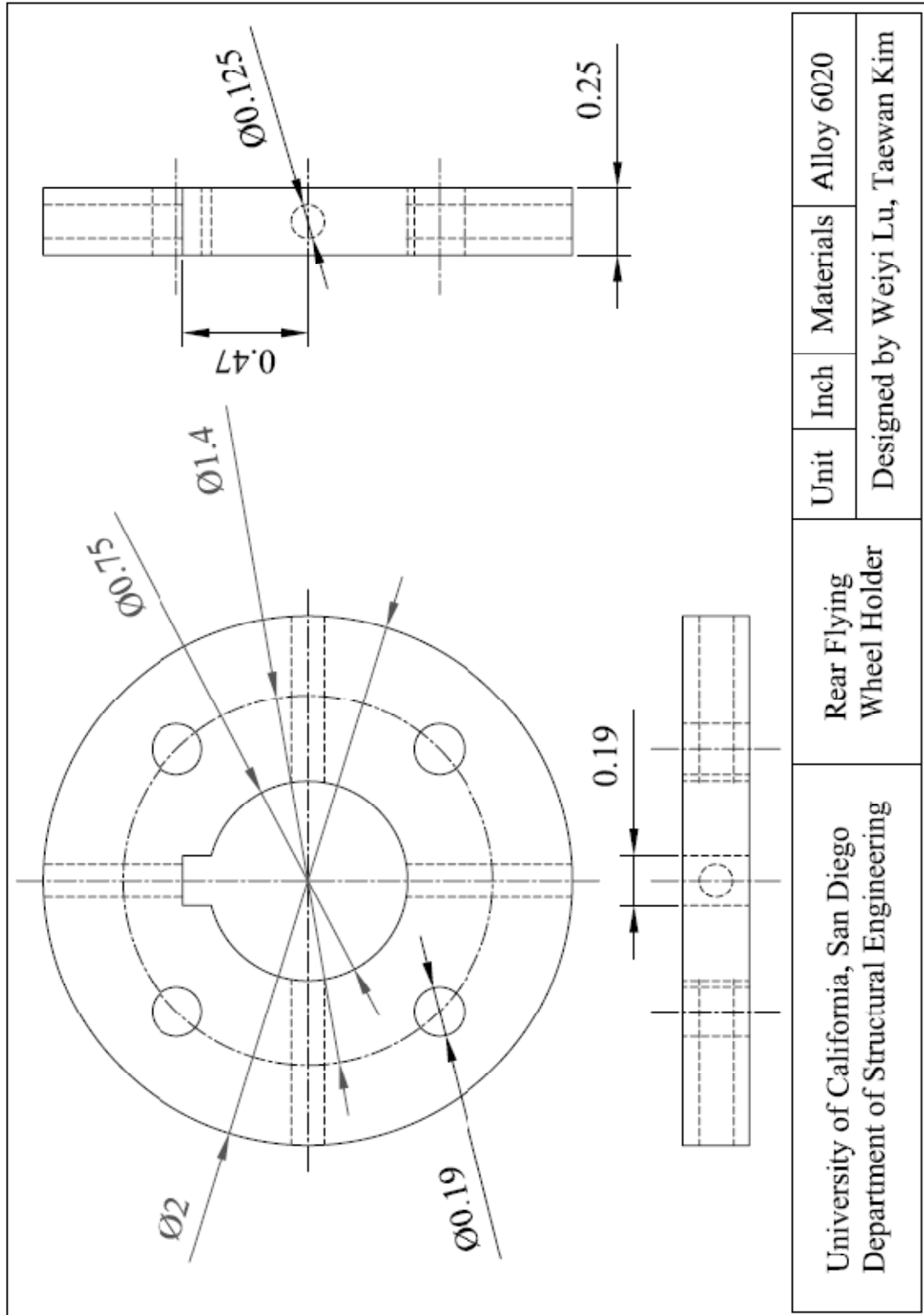
Figure C-7 Fatigue test system - Rear flying wheel holder
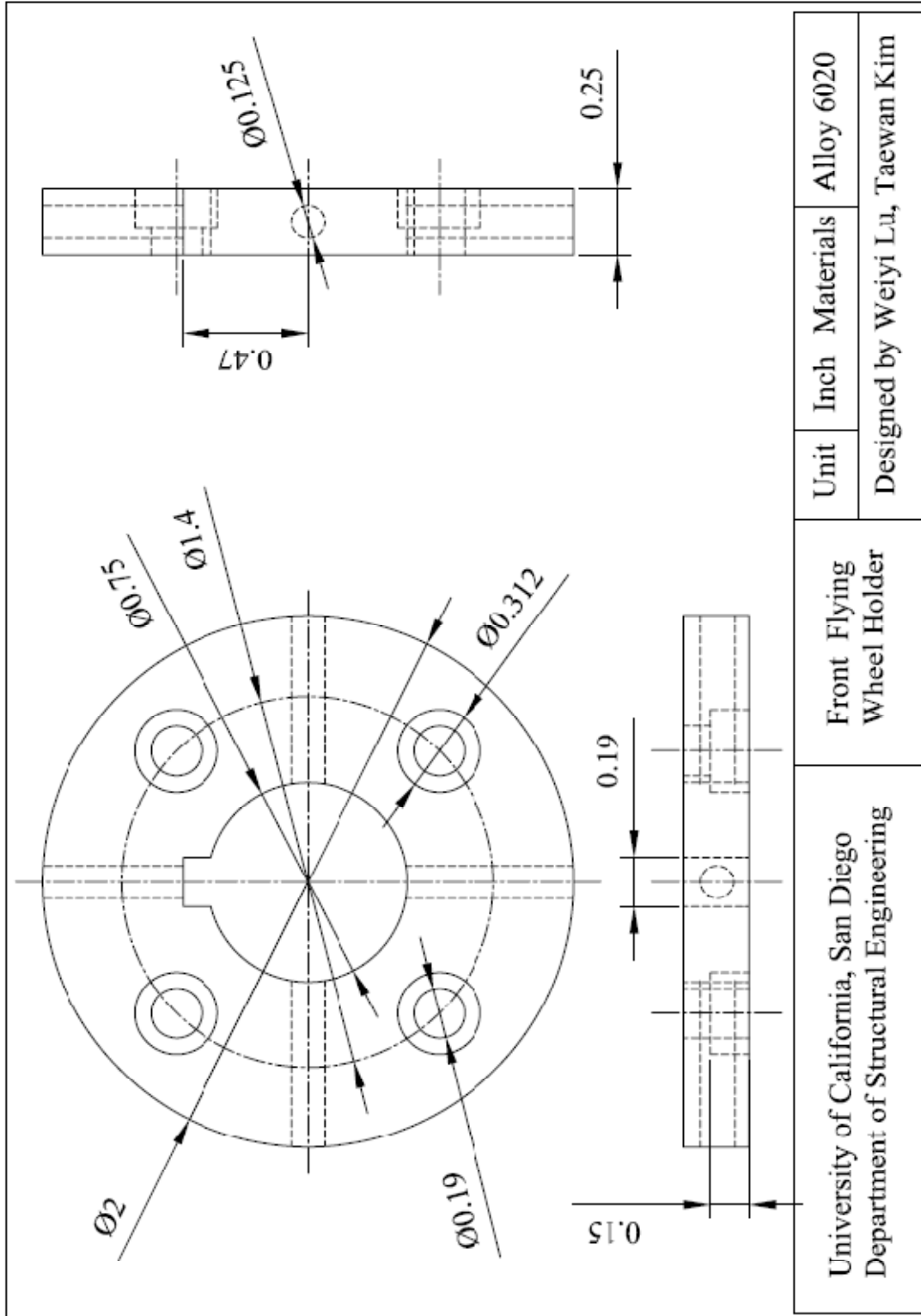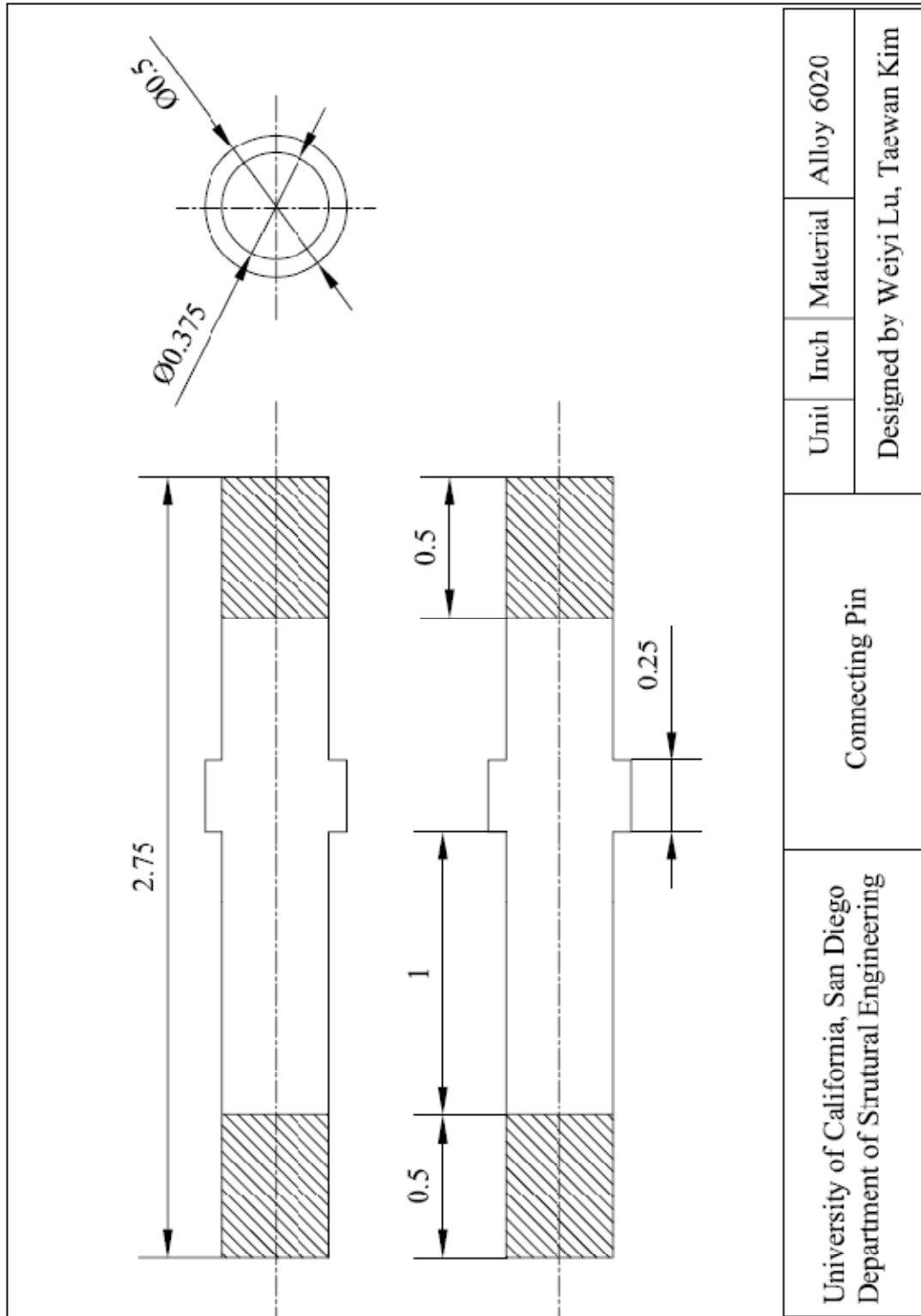
Figure C-8 Fatigue test system - Front flying wheel holder
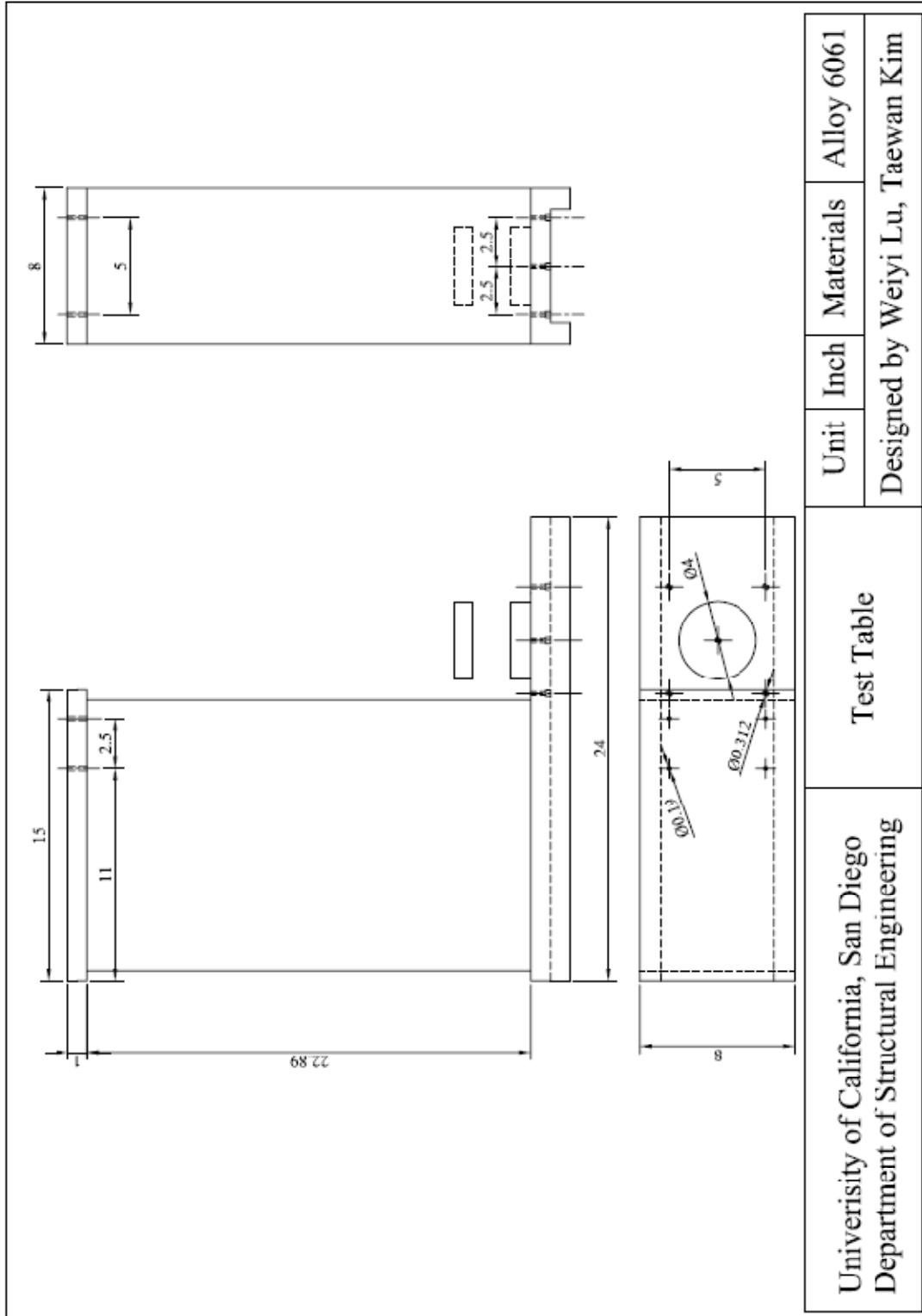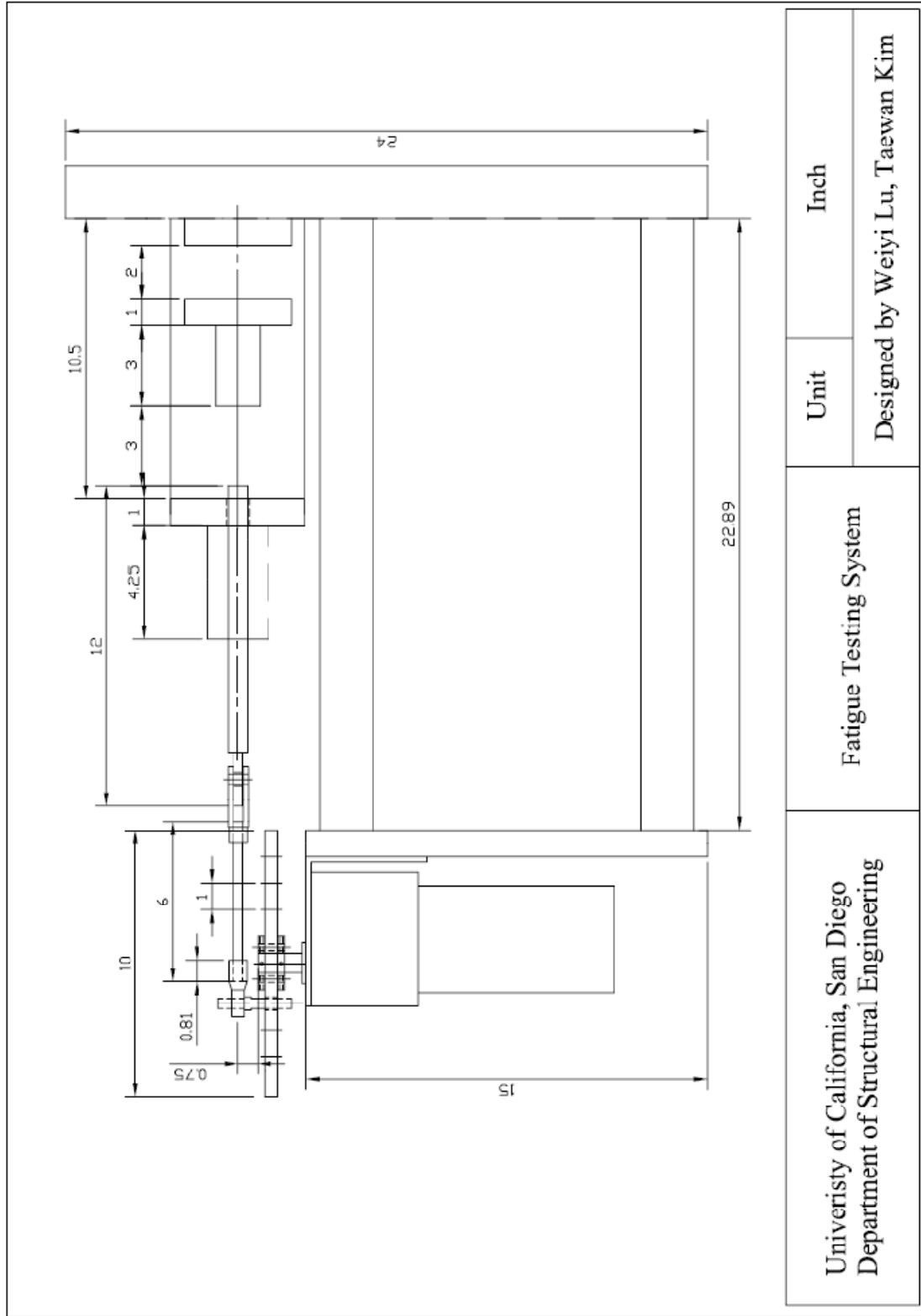
Figure C-9 Fatigue test system - Connecting pin

Figure C-10 Fatigue test system - Test table

Figure C-11 Fatigue test system